2010-01-22

Investigation of Accommodation and Presbyopia using Ultrasound Imaging during Ex Vivo Simulated Accommodation

Raksha Urs
University of Miami, rakshaurs@yahoo.com

UNIVERSITY OF MIAMI

INVESTIGATION OF ACCOMMODATION AND PRESBYOPIA USING
ULTRASOUND IMAGING DURING EX VIVO SIMULATED ACCOMMODATION

By

Raksha Urs

A DISSERTATION

Submitted to the Faculty
of the University of Miami
in partial fulfillment of the requirements for
the degree of Doctor of Philosophy

Coral Gables, Florida

May 2010

UNIVERSITY OF MIAMI

A dissertation submitted in partial fulfillment of
the requirements for the degree of
Doctor of Philosophy

INVESTIGATION OF ACCOMMODATION AND PRESBYOPIA USING
ULTRASOUND IMAGING DURING EX VIVO SIMULATED ACCOMMODATION

Raksha Urs

Approved:

_____
Fabrice Manns, Ph.D.
Associate Professor of Biomedical
Engineering and Ophthalmology

_____
Terri A. Scandura, Ph.D.
Dean of the Graduate School

_____
Jean-Marie Parel, Ph.D.
Henri and Flore Lesieur Chair in
Ophthalmology, Research Associate
Professor of Ophthalmology and
Biomedical Engineering

_____
Jorge Bohorquez, Ph.D.
Research Assistant Professor of
Biomedical Engineering

_____
Arthur Ho, M.Optom, Ph.D., F.A.A.O.
Executive Director Technology,
Institute for Eye Research and
Professorial Visiting Fellow,
School of Optometry and Vision
Science, University of New South
Wales, Sydney, Australia

_____
Giovanni Gregori, Ph.D.
Research Assistant Professor of
Ophthalmology

_____
Peter J. Milne, Ph.D.
Program Director, OPP-ANT,
NSF, Arlington, Virginia

URS, RAKSHA   (Ph.D., Biomedical Engineering)

<u>Investigation of Accommodation and Presbyopia</u>   (May 2010)
<u>using Ultrasound Imaging during Ex Vivo Simulated</u>
<u>Accommodation.</u>

Abstract of a dissertation at the University of Miami.

Dissertation supervised by Professors Fabrice Manns and Jean-Marie Parel.
No. of pages in text. (138)

The goal of this project is to obtain quantitative images of the lens and the ciliary body to validate EVAS-II (Second generation Ex Vivo Accommodation Simulator). To accomplish this goal it was necessary to develop methods, instrumentation and image processing techniques to acquire 3D images in EVAS-II, using UBM (Ultrasound Bio Microscope), and to apply these techniques to non-human primate eyes. The lens studies included measurement of speed of sound in the lens to reconstruct accurate images of the lens, development of instrumentation to measure the un-distorted lens shape and development of a mathematical model to quantify the whole lens shape. Speed measurements showed that the speed of sound exhibits a gradient profile in the equatorial plane, similar to refractive index and protein distributions in the lens. Lens shape measurements showed that the UBM can be used to accurately measure thickness, diameter, cross-sectional area, volume and surface area of the lens. The ciliary body studies included development of instrumentation and algorithms to obtain 3-D images of tissue in EVAS-II and development of methodology to quantify ciliary body movement during stretching. Studies showed that the accommodation process in young baboon eyes in EVAS-II is comparable to the in vivo process in rhesus monkeys. The UBM can be

used to obtain reliable quantitative information about the lens and the ciliary body. 3-D UBM enables monitoring of ciliary body motion of the entire accommodative apparatus.

This dissertation is dedicated to my husband and best friend, Aaron Furtado.

ACKNOWLEDGEMENTS

I would like to thank my family, especially my parents, Jayanthi Urs and T.N. Harin Nanjaraj Urs, for their support and encouragement. Most of all, I would like to thank my

TABLE OF CONTENTS

LIST OF FIGURES

LIST OF TABLES

PUBLICATION NOTE

The following are peer-reviewed articles, and conference presentations that resulted from this dissertation:

Peer-Reviewed Publications:

Urs, R., Manns, F., Ho, A., Borja, D., Amelinckx, A., Smith, J., Jain, R., Augusteyn, R., Parel, J-M. (2009). Shape of the isolated ex-vivo human crystalline lens. *Vision Research , 49*, 74-83.

Urs, R., Ho, A., Manns, F., Parel, J-M. (2009). Age-dependent Fourier model of the shape of isolated ex vivo human crystalline lens. (Submitted to *Vision Research, VR-09-429* acknowledged on 11/10/2009).

Conference Presentations:

Urs, R., Ho, A., Manns, F., Parel, JM. (2009). Model of the isolated ex-vivo human crystalline lens using cosine functions. *25th Southern Biomedical Engineering Conference Oral Presentation*; *IFMBE Proceedings* 24: 241-242.

Urs, R., Ho, A., Manns, F., Parel, JM. (2009). Fourier model of the whole profile of the isolated human crystalline lens. *Investigative Ophthalmology & Visual Science*. 50: E-Abstract 6131.

Bernal, A., **Urs, R.**, Nose, I., Lee, W., Rowan, C., Manns, F., Parel, JM., Augusteyn, B. (2009). A compact shadowphotogrammetry system for measurement of isolated lens shape . *Investigative Ophthalmology & Visual Science*. 50: E-Abstract 5790.

Urs, R., Borja, D., Amelinckx, A., Smith, J., Augusteyn, R., Manns, F., Parel, JM. (2008). Model of the isolated human crystalline lens shape using polynomial functions. *Investigative Ophthalmology & Visual Science*. 49: E-Abstract 3791.

Urs, R., Borja, D., Smith, J., Manns, F., Parel, JM. (2008). Profile of the whole ex-vivo human crystalline lens. *Ophthalmic Technologies XVIII, SPIE BIOS Conference Abstract and Oral Presentation* #6844A-23; San Jose, CA;

CHAPTER 1. **AIMS**

The ability of the eye to change its focus to view near objects is known as accommodation. As the eye ages, it loses this ability gradually. The progressive decline of near vision is referred to as presbyopia.

At present there is a large effort to develop techniques to correct presbyopia and restore accommodation. However, any such effort relies heavily on the knowledge of the accommodative mechanism and presbyopic pathophysiology. The phenomena of accommodation and presbyopia are, at present, not completely understood. In an attempt to characterize and quantify accommodation and presbyopia, a lens stretcher (the second generation Ex Vivo Accommodation Simulator – EVAS-II) that mimics natural accommodation in explanted crystalline lenses, has been developed at the Vision Cooperative Research Centre (Vision CRC) in Australia in collaboration with the Ophthalmic Biophysics Center, at Bascom Palmer Eye Institute.

EVAS-II provides measurements of force, optical power and shape of the crystalline lens during simulated accommodation. The shape is currently recorded using optical imaging techniques. Optical images of lenses need correction because of refraction of light at the anterior surface of the lens and additional distortions caused by variation in optical properties of the lens due to its inhomogeneous composition. Another disadvantage of using optical imaging is that it does not provide any information about the ciliary body. The sclera, which is not transparent, obstructs imaging of the ciliary body and the zonules, which are located beneath it. It is widely accepted by the scientific

community that accommodation occurs as a result of change in zonular tension caused by contraction and relaxation of the ciliary muscle. Consequently information about ciliary muscle movement, morphology and response time is important for studying accommodation.

High frequency Ultrasound Bio Microscopy (UBM) is used extensively in ophthalmic clinics and in research to investigate anterior segment structures. The advantage of using UBM imaging in the lens stretcher is that UBM allows imaging of the ciliary body during simulated accommodation. These images can be compared to published in vivo data.

The goal of this project is to obtain quantitative images of the lens and the ciliary body in EVAS-II using UBM. Information obtained about the shape of the lens and the orientation and position of the ciliary muscle will be used to validate EVAS-II and to improve numerical models of the accommodative mechanism. This project has three specific aims:

Aim 1: To demonstrate the feasibility of quantitative imaging of the lens and ciliary body using UBM. Cross-sectional images of the lens and the ciliary body in the cadaver eye will be obtained with a high resolution UBM. The speed of sound through the lens will be measured to reconstruct the shape of the lens from the recorded UBM data. A shadow-photogrammetric system will be developed to obtain images of lenses. Algorithms will be developed to obtain contours of the lens and describe its shape mathematically. The lens contours obtained from the two imaging modalities will be compared to validate the lens shape obtained from the UBM.

Aim 2: To obtain 3-D images of the accommodative structures in the lens stretcher. The transducer of a high resolution UBM will be interfaced to EVAS-II. The transducer will be mounted on a linear motion stage to obtain cross-sectional images of the lens and the ciliary body across multiple planes parallel to the lens equatorial axis. Images will be reconstructed in multiple meridional planes from these cross-sectional images.

Aim 3: To evaluate ciliary muscle configurational changes during stretching. Ciliary muscle configurational changes will be quantified to determine if its movement during stretching is akin to the in vivo accommodative change. Radial cross-sectional images of the ciliary body obtained at different stages of stretching will be compared to in vivo data that is published or measured.

The data obtained from this study will be used to validate and if necessary enhance EVAS-II and to improve finite element models of accommodation.

CHAPTER 2. **BACKGROUND AND SIGNIFICANCE**

2.1 **Accommodation and Presbyopia**

2.1.1 **Accommodation**

Accommodation is the ability of the eye to focus on objects at various distances. During this process the dioptric power of the eye increases. There are currently three main theories describing the mechanism of accommodation.

The most extensively accepted theory of accommodation, which is the Helmholtz theory (Helmholtz, 1855), attributes accommodation to a change in the shape of lens. In the unaccommodated state, the ciliary muscle is relaxed, causing a resting tension on zonular fibers. This zonular tension flattens the lens. As the ciliary muscle moves forward and inward during contraction, the zonules relax, allowing the lens to thicken (Figure 2.1). The posterior and anterior surfaces of the lens become more curved thereby increasing the refractive power of the lens.
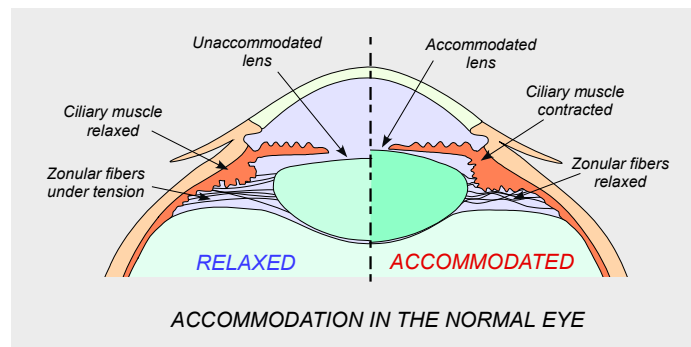
Figure 2.1: Changes that occur during accommodation in the normal eye (Manns, et al., 2004a). When the ciliary muscle contracts, the zonules relax and the lens thickens.

4

The Coleman theory (Coleman, 1970 and 1986; Coleman and Fish, 2001) attributes the change in lens shape to the force exerted by the pressure gradient between the vitreous and the aqueous chambers, rather than the radial traction of the zonules. According to this theory, the lens, zonules and anterior vitreous together form a catenary. Ciliary muscle contraction causes pressure differences between the aqueous and the vitreous body which changes the catenary. The Coleman theory does not ascribe accommodation to change in tension of the zonules.

An alternate theory proposed by Schachar (Schachar et al., 1993a, 1993b; Schachar and Bax, 2001a, 2001b) hypothesizes that the relaxation of the ciliary muscle releases zonular tension at the anterior and posterior surfaces of the lens, but increases zonular tension at the equator, causing an increase in the equatorial lens diameter, a central steepening of the lens and a peripheral flattening. There is overwhelming evidence suggesting that this theory is incorrect and founded on flawed anatomical and mechanistic assumptions (Glasser and Kaufman, 2003; Strenk et al., 2005).

2.1.2 Presbyopia

Presbyopia is a reduction in accommodative ability that occurs normally with age. There are two main theories of presbyopia (Atchison 1995): (a) Lenticular theory, which attributes presbyopia to mechanical and geometric changes of the lens (b) Extralenticular theory, which ascribes presbyopia to changes in ciliary muscle and changes in elastic components of zonule and ciliary body. Although presbyopia is a widespread, inevitable ocular affliction, its precise pathophysiology is yet to be elucidated. However, it is widely accepted that presbyopia is multifactoral and that the anatomical changes of the

accommodative structures restrict the ability of the ageing lens to change its shape. All individuals begin to require some form of optical correction for near vision around age 40. With increasing life expectancy and expansion of the ageing population, the number of presbyopes is expected to increase. The quality of life of this ageing population will significantly improve if accommodative ability can be restored.

2.1.3   Presbyopic Correction

The endeavor to restore accommodation has led scientists to investigate four major forms of intraocular presbyopic corrections: (A) IOL implantation, where the traditional intraocular lenses (IOLs) that are used for cataract surgery are being modified to create accommodative IOLs (Mastropasqua et al., 2003); (B) Scleral expansion surgery, which is based on the Schachar theory of accommodation and presbyopia, where the scleral diameter is expanded to increase the space between lens equator and ciliary body (Fukasaku and Marron, 2001; Marmer, 2001; Schachar, 2002).; (C) Lens softening where the lens nucleus is softened by photo-disruption with a high power laser (Myers and Krueger, 1998, Ripken, et al., 2008); and (D) Lens refilling where the contents of the crystalline lens are surgically removed and the capsular bag is implanted with a suitable polymerized gel. The lens-refilling technique, Phaco-Ersatz, developed by Parel et al. (1986) is based on the assumption that accommodation can be restored if the properties of the lens are restored.

2.2   Phaco-Ersatz

Phaco-Ersatz is a surgical lens-refilling technique developed to restore accommodation. Unlike scleral expansion or lens softening, which leave the natural

crystalline lens in place, this technique replaces the contents (cortex and nucleus) of the presbyopic lens with a flexible material or implant. Phaco-Ersatz relies on the assumption that a person will be able to accommodate if the injected polymer has suitable viscoelastic and optical properties to allow the lens to regain its ability to change shape in response to accommodative forces. It involves a procedure to make a small opening in the lens capsule periphery in the order of 1 mm in diameter, called mini-capsulorhexis (Tahi et al., 1999). The lens material is removed through this opening and a suitable polymer gel is injected into the intact emptied capsular bag through the same opening (Figure 2.2). The feasibility of restoring accommodation using this technique has been demonstrated in the live rhesus monkey (Haefliger and Parel, 1994; Nishi and Nishi 1998; Koopmans et al., 2006).
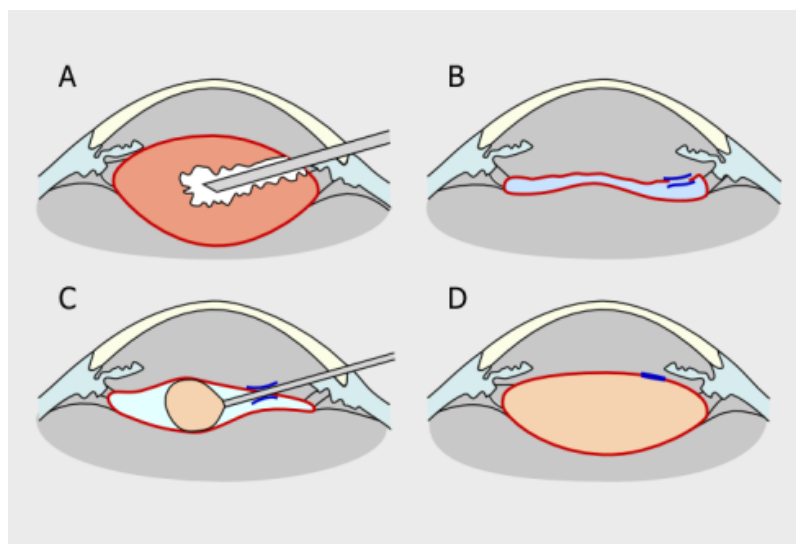
Figure 2.2: The surgical technique of Phaco-Ersatz includes extraction of the nucleus and cortex through a small opening (mini-capsulorhexis) in the capsule (A) while leaving the capsule intact (B) and then injecting a polymer gel into the empty capsule (C). With proper design of the gel, a person may be able to accommodate after the procedure because the accommodative mechanism is maintained (D) (adapted from Parel et al., 1986).

The Ophthalmic Biophysics Center of Bascom Palmer Eye Institute in collaboration with the Vision CRC in Australia and the LV Prasad Eye Institute in India is undertaking a project called the Dynamic Vision (DV) project to cure presbyopia using the Phaco-Ersatz technique. This project involves research on surgical techniques and design and development of the refilling polymer. The opto-mechanical properties of the accommodative structures are also being investigated as part of an NIH funded project. An ex vivo experimental set up was required in order to facilitate scrutiny of the accommodative response of lenses refilled by the phaco-ersatz procedure. The lens stretcher EVAS-II was developed as a part of the DV project to emulate on explanted lenses, the changes in zonular tension produced during accommodation.

2.3 EVAS-II

Over the past three-quarter century, several technically innovative ex vivo set-ups have been developed to study the relationship between force of accommodation and lens shape. Pau (1951), the pioneer of this approach, simulated accommodative force by attaching weights to the ciliary body. Fisher (1971) introduced a spinning test to imitate the pull on the zonules, and later (1977) developed another system that simulated accommodation by radial stretching. A system that simulated accommodation by applying circumferential forces was built by Sunderland and O'Neill (1976). van Alphen and Graebel (1991) used a uniaxial loading approach. Pierscioneck (1995) and Glasser and Campbell (1998) have also developed lens stretchers. The last two studies did not include force measurements.

A stretching system called EVAS (Ex Vivo Accommodation Simulator) was designed and constructed in house at the Ophthalmic Biophysics Center at the Bascom Palmer Eye Institute (Parel, et al. 2002). This system was based on designs by Fischer (1971, 1977), Sunderland and O'Neill (1976), and Glasser and Campbell (1998). EVAS is a computer controlled stretching system that applies a circumferential load to the zonular apparatus of cadaver eyes. EVAS was used to show that the force necessary to change the lens diameter and lens power increases with age in human and monkey lenses (Manns et al., 2007).

EVAS-II, the Second generation Ex Vivo Accommodation System, was designed and constructed in Australia at the Vision CRC (Ehrmann et al., 2008) to solve some of the limitations of the first generation system. This instrument is composed of eight identical linear motion stages with integrated force transducers, arranged in a symmetric star pattern and connected to a computer (Figure 2.3 (a) and (b)). Customized software allows control of the stretching motion and acquisition of signals from the force sensors. It also allows image capture for the lens diameter measurements. Several other measurement instruments such as an optical power measurement system and Optical Coherence Tomography (OCT) (Uhlhorn et al., 2008) and Scheimpflug (Borja, et al., 2009a) imaging systems have been integrated into this lens stretcher. EVAS-II emulates on explanted lenses, the changes in zonular tension produced during accommodation. It allows direct measurement of the force required to stretch the crystalline lens to its unaccommodated state and measurements of the lens equatorial diameter, thickness, curvature and changes in lens power during stretching. Figure 2.3 (c) and (d) show some typical results obtained from EVAS-II. Figure 2.3 (c) shows the variation of power with

displacement and Figure 2.3 (d) shows variation of thickness and diameter with stretch for a 2 year old Baboon lens (3 hours postmortem time).
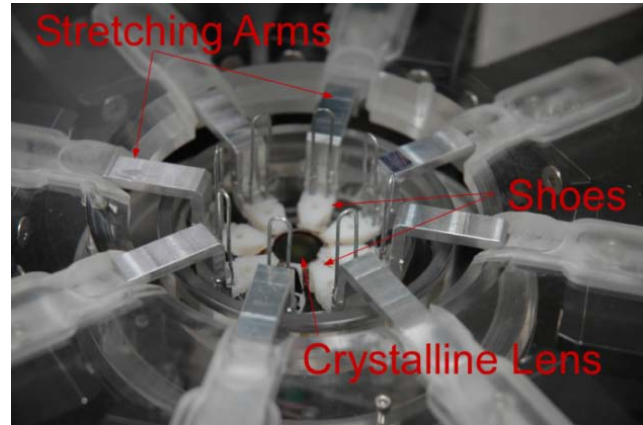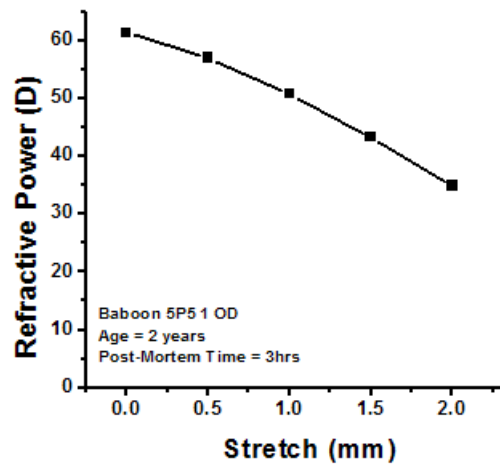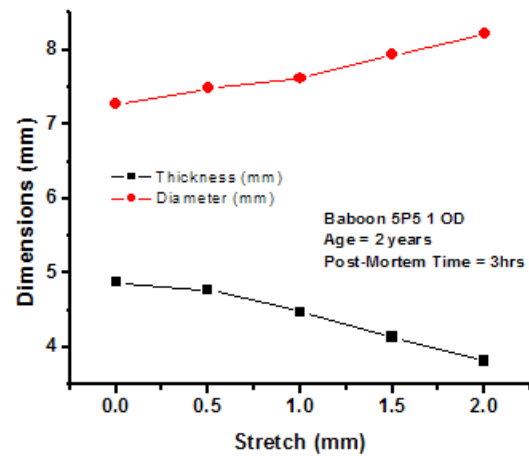
Figure 2.3: Figure (a) shows the second generation Ex Vivo Accommodation System (EVAS-II). Figure (b) shows a closer view of the system with tissue mounted. Figures (c) and (d) show some typical results obtained from EVAS-II. Figure (c) shows the variation of power with displacement and Figure (d) shows variation of thickness and diameter with stretch for a 2 year old baboon lens (3 hours postmortem time).

EVAS-II allows measurement of lens thickness, diameter and curvature using optical imaging techniques such as OCT and Scheimpflug imaging. Crystalline lens images, produced by optical imaging modalities need correction due to the refraction of light at the anterior surface of the lens. Additional corrections are required to account for inhomogeneous optical properties of the lens. EVAS-II currently does not have the capability of observing and recording the movement of the ciliary muscles and the zonules. The ciliary muscle and zonules cannot be imaged using optical imaging techniques because the sclera is opaque and obstructs these structures, which are located under the sclera. The anterior zonules are visible only when tissue is stretched. This problem will be circumvented by using the UBM. Quantitative three dimensional images of the lens along with the ciliary body will be obtained using the UBM in EVAS-II. Information obtained about the ciliary muscle configuration changes in EVAS-II will be compared to in vivo data to validate EVAS-II.

2.4   Importance of imaging the Ciliary Muscle and the Lens

The ciliary body, which is composed of the ciliary muscle and ciliary processes, is a triangular shaped region bound on its outer surface by the anterior sclera and on its inner surface by the pigmented epithelium (Glasser and Kaufman, 2003). The ciliary processes mostly consist of blood vessels. The stroma of the processes is made of loosely arranged connective tissue. The ciliary processes are covered by a two layered epithelium. The ciliary muscle is a smooth muscle with parasympathetic innervations. The anterior ciliary muscle insertion occurs partly at the scleral spur and partly within the trabecular meshwork (Figure 2.4 (a)). Posteriorly the ciliary muscle is attached to the stroma of the choroid. The ciliary muscle fiber bundles are oriented such that a

contraction of the ciliary muscle results in a forward and inward redistribution of the ciliary body.

According to the Helmholtz theory of accommodation, the change in lens shape, and thereby in its dioptric power, occurs as the result of a change in zonular tension, which is caused by contraction and relaxation of the ciliary muscle. Figure 2.4 (b) shows a Scanning Electron Microscopy (SEM) image of the accommodative structures of a non human primate lens (Rohen, 1979). It has been shown that during accommodation, in addition to radial motion, the ciliary muscle also exhibits a slight anterior motion (Stachs et al., 2002; Croft et al., 2006, 2009; Strenk et al., 2006) (Figure 2.5).

The lens stretcher EVAS-II simulates accommodation by exerting a radial force on the sclera, in the direction away from the lens. If this force introduces differences in the configurational changes of the ex vivo ciliary muscle compared to the in vivo movement, the force transmitted to the zonules may not be a replica of that transmitted in the in vivo process. As a result the simulated accommodation of the lens stretcher may not truly mimic accommodation and the forces may be different. To validate EVAS-II it is necessary to quantify any potential differences from the in vivo mechanism.

One limitation of ex vivo studies is that postmortem ischemic changes will prevent the ciliary muscle from responding normally. The ciliary muscle has been shown to contain an unusually high number of mitochondria compared with smooth muscles (Ishikawa, 1962), thereby accelerating the postmortem ischemic changes. However, ciliary muscle of the rhesus monkey has been shown to respond equally to cholinergic

agonists 1 to 32 hours post-enucleation, enabling ex vivo studies within this time frame (Poyer, et al., 1993).

The UBM will be a valuable addition to EVAS-II as it will facilitate imaging of both the ciliary muscle and the lens at the same time and in three dimensions. These images will provide valuable insight about the anatomical relationship between the lens and the ciliary body at various stages of stretching. The UBM can also be used as an exploratory tool to measure the speed of sound in the lens, which in turn can be used to investigate the mechanical properties of the lens.

(a)   (b)
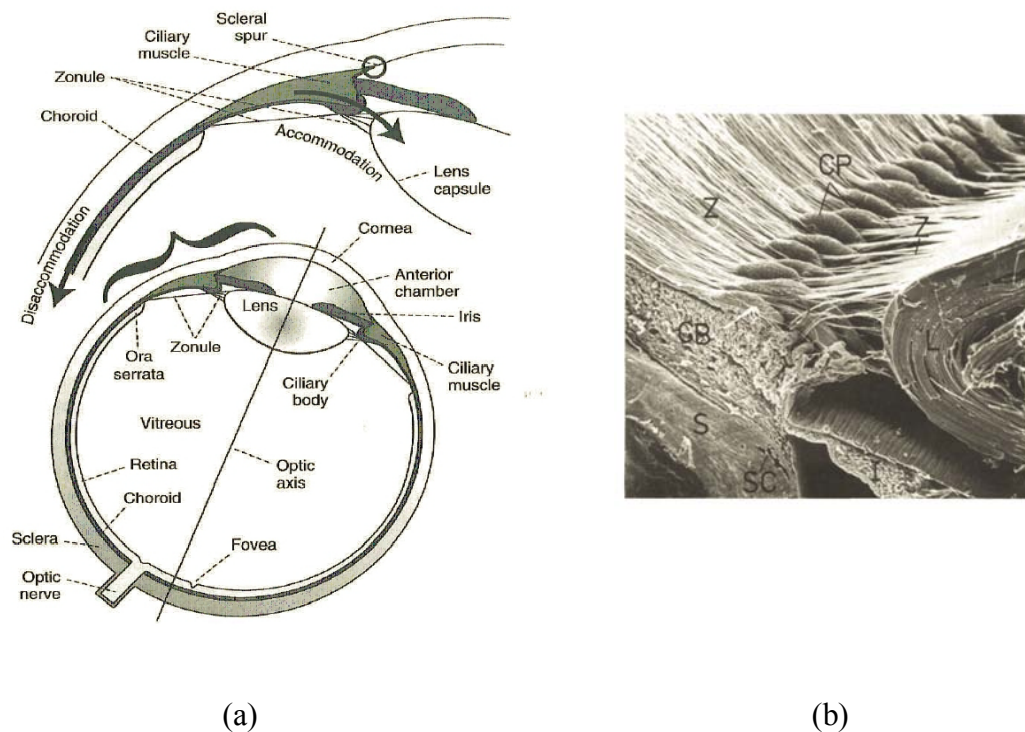
Figure 2.4: (a) Schematic representation of the cross-section of the ciliary region of the eye. (Glasser and Kaufman 2003). (b) Scanning Electron Microscopy (SEM) image of the accommodative structures of a non-human primate eye. [Z: Zonule, CB: Ciliary Body, CP Ciliary Process, L: Lens, I: Iris, S: Sclera] (Rohen, 1979).

Sclera

Vitreous
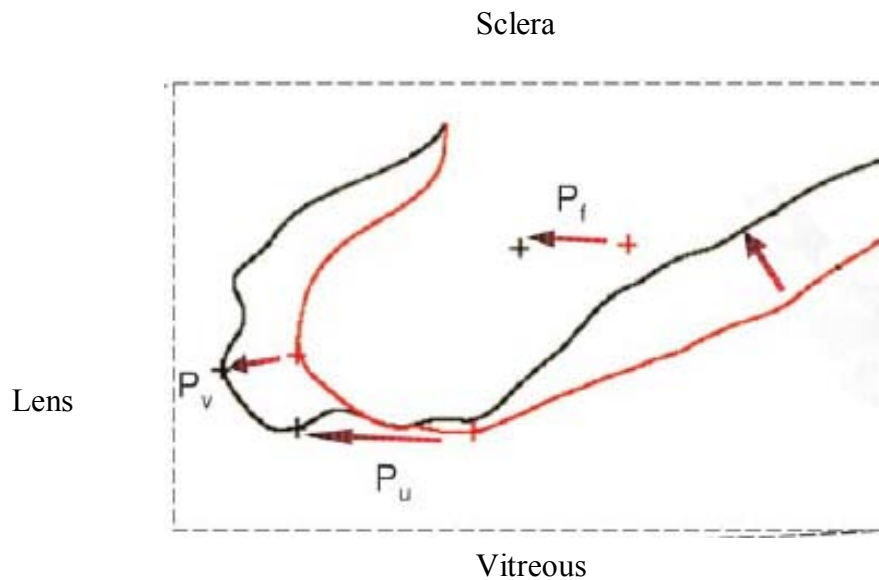
Figure 2.5: An example of quantification of the contour changes of the ciliary muscle during accommodation (Stachs et al., 2002). The outer contours in accommodation (black) and dis-accommodation (red) are shown, as is the shift of defined characteristic contour points (center of gravity Pf, anterior contour point Pv and lower contour point Pu).

2.5 Summary

Knowledge of the shape of the lens and the position and orientation of the ciliary muscle during accommodation is important to understand accommodation and to develop new treatments for presbyopia. Previous measurements of lens shape in EVAS-II were made with optical imaging techniques. The position and orientation of the ciliary muscle has not been recorded in EVAS-II.

The goal of this project is to obtain quantitative images of the lens along with the ciliary muscle. To achieve this goal, a high frequency UBM will be used to image the lens and the ciliary muscle together in EVAS-II. The speed of sound through the lens will

be measured, and these measurements will be used to reconstruct the images of the lens. Images of the ciliary muscles will be compared to in vivo images to verify if their configurational changes are similar to the in vivo accommodative changes. This data can serve to improve finite element models of accommodation and to validate and if required enhance EVAS-II.

CHAPTER 3. **ULTRASOUND BIO-MICROSCOPY**

3.1 Overview

This chapter provides a brief background of ultrasound imaging, review of anterior segment ophthalmic ultrasound and description of the ultrasound system used in this study.

3.2 Background

Sound or acoustic waves are mechanical disturbances that propagate through an elastic medium. Unlike optical waves, acoustic waves cannot propagate in vacuum. Ultrasound is an acoustic wave with frequency beyond the human maximum audible limit of 20 KHz.

Many unrelated scientific advances led to the discovery of ultrasound. Spallanzani, an Italian biologist and physiologist, discovered in 1793, that bats had the ability to maneuver in complete darkness. Through his experiments he observed that "Blinded bats are able to use their ears when they hunt insects….this discovery is incredible" (Neuweiler 2000). Galton with his ingenuous creation, the Galton Whistle, was able to demonstrate the normal upper limit of human hearing, and that several animals could hear higher frequencies (Galton, 1883). It was in the 1940s, that Griffin and Galambos solved 'Spallanzani's bat problem'. They demonstrated that bats are capable of emitting ultrasound impulses and evaluating their echoes (Griffin, 1958).

In 1880, the Curie brothers discovered the piezo-electric effect (Katzir 2003), the transformation of mechanical energy into electrical energy. In 1881, Lippman mathematically demonstrated the reciprocal behavior of achieving a mechanical stress in response to a voltage difference (Lippman, 1881). This led to the birth of a device to emit and detect ultrasound signals. Langevin developed an underwater orientation device, during World War I, on the basis of the piezo-electric effect (Stephens 1972). This device became the principle for the SONAR system. Dussik first proposed the use of ultrasound as a diagnostic system in 1941 (Dussik, 1942). He produced the first medical ultrasound images in 1945 (Dussik, 1952). The images were of human brain and ventricles.

3.3　Principle of Ultrasound Imaging

3.3.1　Overview

Ultrasound diagnostic systems utilize the interaction of sound waves with biological tissue to produce cross-sectional images. A high frequency acoustic wave is directed toward the object of interest. This wave undergoes partial reflection at the object boundaries. These 'reflections' or echoes are recorded and the positions of the boundaries are computed using sound velocities through the travelling media and time taken to receive the echoes. The following sections provide a brief review of ultrasound characteristics, ultrasound production, ultrasound beam properties, spatial resolution and different modes of ultrasound imaging.

3.3.2　Characteristics of Ultrasound

Ultrasound is mechanical energy which propagates through a continuous elastic medium by displacement of particles that compose the medium. Ultrasonic waves are

longitudinal waves, which cause displacement of particles in the medium in a direction that is parallel to the wave motion. The wave propagation velocity (c – m/s) is related to its frequency (f - Hz) in time and wavelength (λ - m) in space and is given by:

$$c = \lambda f.$$
Equation 3.1

As ultrasound energy propagates through a medium, it undergoes reflection, refraction, scattering and attenuation. The acoustic properties of the medium affect the energy of the waves during these interactions. The acoustic impedance (Z - Rayls) of the material is defined as:

$$Z = \rho c.$$
Equation 3.2

where ρ is the density of the material (kg/m^3) and c is the speed of sound (m/s) in that material. When there is a difference in the acoustic impedances of adjacent materials reflection occurs at the boundary. For perpendicular incidence, the intensity reflection coefficient is given by Equation 3.3 where Z_1 and Z_2 are the acoustic impedances of the two materials.

$$R = \left(\frac{Z_2 - Z_1}{Z_2 + Z_1} \right)^2$$
Equation 3.3

The intensity transmission coefficient is then given by:

$$T = 1 - R.$$
Equation 3.4
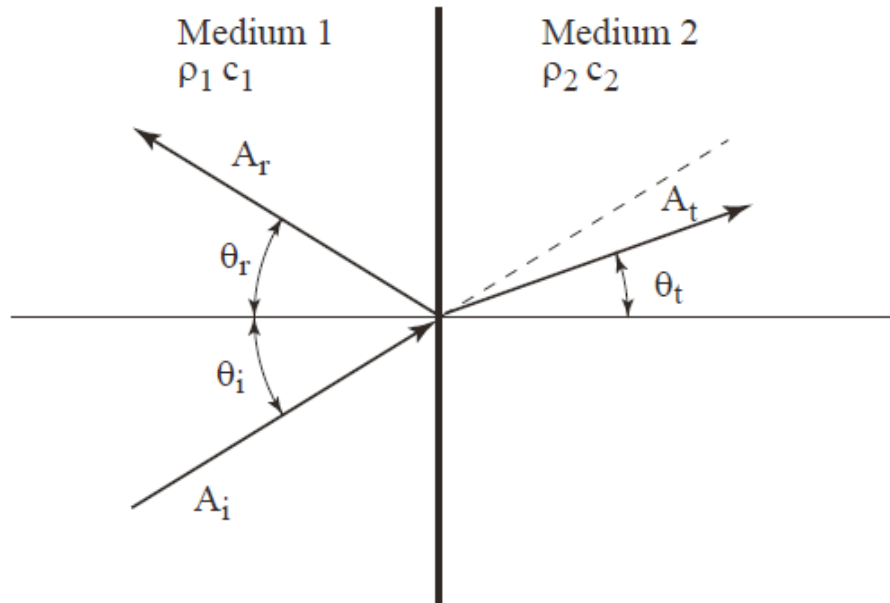
Figure 3.1: Schematic representation of an incident wave undergoing reflection and refraction at a planar boundary between two different materials (Suetens, 2002). The subscripts *i, r* and *t* stand for incidence, reflection and transmission. A_x represents the amplitude of sound wave and θ_x represents the angles.

If the incident beam is perpendicular to the boundary, the reflected beam directly returns back to the source and the transmitted beam continues in the original direction. However, if the beam has a non-perpendicular incidence, the transmitted beam undergoes a change in direction (Figure 3.1). This phenomenon is referred to as refraction. The angle of refraction is related to the angle of incidence as defined by Snell's law:

$$\left(\frac{\sin \theta_t}{\sin \theta_i} \right) = \frac{c_2}{c_1} \qquad\qquad \text{Equation 3.5}$$

where θ_t and θ_i are the angles of refraction and incidence and c_2 and c_1 are the speeds of sound in the two media. The angle of reflection (θ_r) is equal to the angle of incidence (θ_i) (Equation 3.6).

$$\theta_r = \theta_i \hspace{4cm} \text{Equation 3.6}$$

The equations above are for the case of specular reflection where the surface of the reflector is large, smooth and flat. When an ultrasound wave encounters a target that is smaller than a few wavelengths, the echo generated is scattered in multiple directions. Most biological tissues are inhomogeneous and produce diffuse reflections due to scattering. Echoes produced by diffuse scattering are weaker than those from smooth tissue boundaries. Some of the acoustic energy is also absorbed by the tissue and converted to heat. Reflection, scattering and absorption contribute to the attenuation of sound energy. Ultrasound attenuation due to absorption is approximately proportional to frequency. When examination of deeper structures is required, lower frequency ultrasound must be used.

3.3.3 Ultrasound Production

The main component of an ultrasound imaging system is a piezo-electric transducer that produces and detects ultrasonic energy. Two piezo-electric materials that are often used are PZT (lead zirconate titanate) and PVDF (polyvinylidene fluoride). Figure 3.2 shows a schematic illustration of the cross section of an ultrasonic transducer (Bushberg, et al., 2001). It consists of three important elements, namely, a piezoelectric crystal, a backing layer and a matching layer, housed in a metal shield.
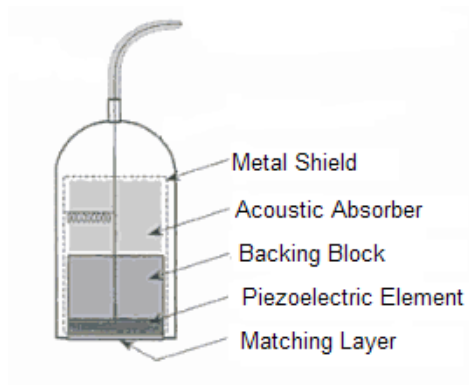
Figure 3.2: Schematic illustration of an ultrasonic transducer (Adapted from Bushberg, et al., 2001). The transducer consists of three main elements, i.e. a backing layer, a piezoelectric crystal and a matching layer, housed in a metal shield.

PRP
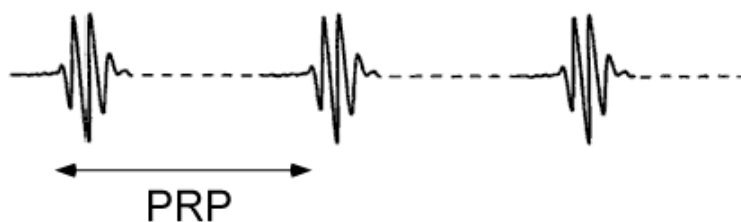
Figure 3.3: The transducer is pulsed for a brief period of time and switched to receive mode to record the echoes. This cycle is referred to as the pulse repetition period.

When a piezoelectric crystal is driven with a sinusoidal electrical signal, it vibrates, producing a sound wave at the same frequency. If the thickness of the crystal is exactly half the wavelength, the amplitude of the vibration is maximal due to the phenomenon of resonance. The backing block serves to dampen the transducer vibration. The acoustic absorber is added to absorb the remaining vibrations. Dampening produces short pulse length, but also increases the bandwidth of the ultrasound pulse. At the imaging surface, the crystal is padded with a matching layer to maximize transmission of energy from the crystal to biological tissue through destructive interference. The

matching layer is chosen so that its acoustic impedance is equal to $\sqrt{Z_c Z_t}$, where Z_c and Z_t are the acoustic impedance of the crystal and tissue respectively. The optimal matching layer thickness is equal to an odd number of quarter wavelengths. An ultrasonic transducer can only generate and receive a limited band of frequencies, which is referred to as the bandwidth of the transducer. The most common form of transducer is a simple single element transducer. Transducer arrays are also available that employ many individual piezoelectric elements.

Medical diagnostic ultrasound commonly employs frequencies between 2 and 15 MHz. The transducer is pulsed for a brief period of time and switched to receive mode to record the echoes. This cycle is referred to as the pulse repetition period (Figure 3.3). When the transducer is pulsed, acoustic waves produced by the transducer are focused into a beam and transmitted through the soft tissues of the body and target organ. The transducer is then switched to receive mode for a brief period of time to record the echoes. These echoes are converted to electric signals by the transducer and transmitted to a Central Processing Unit (CPU) where they are processed.

3.3.4 Beam Properties

The ultrasound beam emitted from a transducer surface travels in a propagation medium as a longitudinal wave. The beam properties for a single, circular transducer element are described below. The ultrasound beam propagation is characterized by two distinct regions: the near field where the beam converges and the far field where the beam diverges (Figure 3.4).
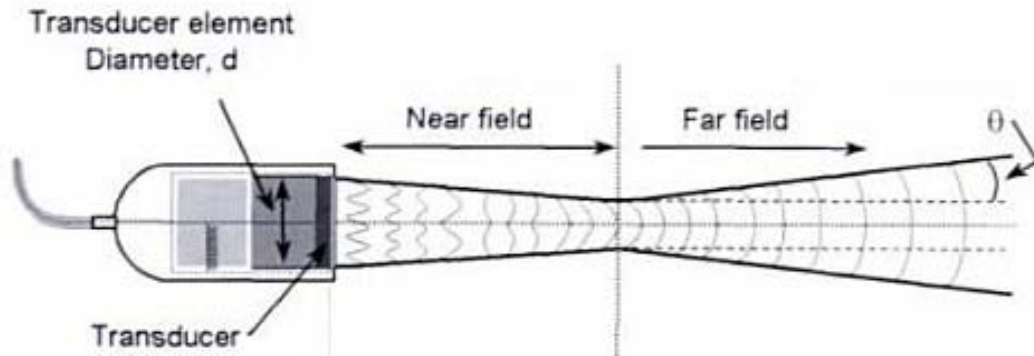
Figure 3.4: Schematic of ultrasound beam from a single, circular transducer element. (Adapted from Bushberg, et al., 2001). The beam is characterized by near field and far field regions.

The near field is also known as the Fresnel zone. The distance from the transducer face to the position of the narrowest beam width or the length of the near field is the focal length (F) of the transducer. It depends on the transducer diameter and the frequency of the transmitted wave and is given by:

$$F = \frac{d^2}{4\lambda} = \frac{d^2 f}{4c} \qquad\qquad \text{Equation 3.7}$$

where d is the diameter of the transducer element and λ is the wavelength, f is the frequency and c is the propagation speed of the sound wave (Bushberg, et al., 2001).

The far field, also known as the Fraunhofer zone, is characterized by a diverging beam. The divergence angle, θ, of the beam, is given by (Bushberg, et al., 2001):

$$\sin\theta = 1.22\frac{\lambda}{d} = 1.22\frac{c}{fd} \qquad\qquad \text{Equation 3.8}$$
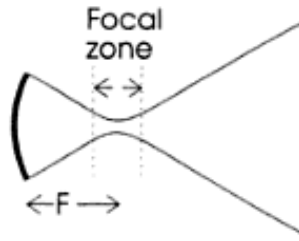
Figure 3.5: Illustration of a curved element focused transducer (adapted from Dendy and Heaton, 1999).

The depth of field (DOF) provides a measure of the range of depths over which the transducer maintains reasonable good focusing properties. A good approximation for the *DOF* at the 3dB intensity level is given by (Cobbold 2007):

$$DOF = 7.2\lambda\left(\frac{F}{d}\right)^2 = 7.2\lambda(f-number)^2 = 7.2\frac{c}{f}(f-number)^2 \qquad \text{Equation 3.9}$$

An ultrasound beam can be focused at shorter distances by using a transducer with a curved surface (Figure 3.5). Focused transducers produce an increased convergence of the beam in the near field thereby producing smaller beam diameters at the focus. However, this is accompanied by an increased beam divergence in the far field and a reduced depth range where the transducer maintains good focusing properties. This range is called the focal zone and can be adjusted independent of the focal length. For a plane transducer the DOF is dependent on the focal length.

3.3.5 Resolution

The resolution of an imaging system is its ability to distinguish two closely situated structures accurately. Lateral resolution, R_{lat}, is the resolution along the direction

that is perpendicular to the direction of wave propagation. It is dependent on the beam diameter and is best at the focal length of the transducer. The lateral resolution is given by (Cobbold, 2007):

$$R_{lat} = 1.22\lambda\left(\frac{F}{d}\right) = 1.22\lambda(f-number)$$
Equation 3.10

A focused transducer with a short focal length produces a small spot size and therefore has a high lateral resolution. However the decreased focal zone limits the imaging depth.

Axial resolution, R_{ax}, or the resolution along the direction of wave propagation, is inversely proportional to the pulse duration and is given by:

$$R_{ax} = \frac{1}{2}cT_p$$
Equation 3.11

where c is the speed of sound and T_p is the pulse duration (Cobbold, 2007).

As both axial and lateral resolutions improve with increasing frequency, higher frequency transducers are generally preferred for imaging finer structures. However, there are several drawbacks of using higher frequencies. Attenuation of sound in tissue increases with frequency and therefore penetration decreases at higher frequencies. The Depth of Field also decreases, as it is inversely proportional to the frequency. These issues must be considered carefully and the right parameters have to be chosen for the desired application.

3.3.6 Imaging Modes

There are two basic modes of ultrasound imaging: A-mode systems which provide depth information about a point and B-mode systems which provide depth information about a line. A-mode systems generate one dimensional output and are displayed as a function of time. They are commonly employed for biometry, or computation of distances. Figure 3.6 shows an A scan signal at the center of a non human primate lens. The first two peaks correspond to the two surfaces of the lens. The third peak is the reflection from a window placed under the lens. The thickness of the lens can be computed by multiplying the time of travel between the two peaks with the speed of sound in the lens.
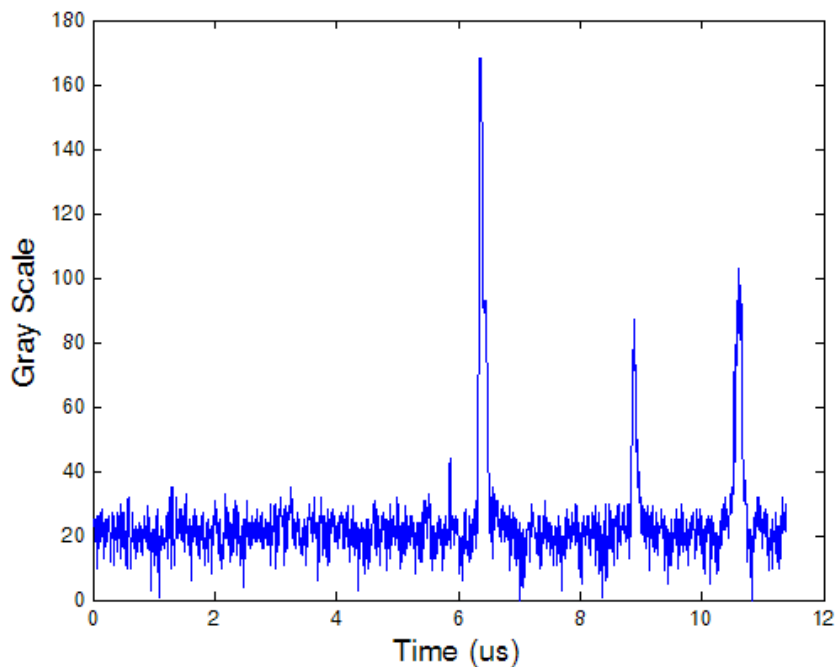
Figure 3.6: An example of an A-Mode Signal. Reflected signal is displayed as a function of time. The first two peaks correspond to the two surfaces of the lens. The third peak is the reflection from a window placed under the lens.

B-mode systems generate cross-sectional gray-scale images by scanning the transducer in the transverse direction and combining multiple A-mode acquisitions. Figure 3.7 shows a B-mode image of a non-human primate lens. The lens is oriented such that the posterior surface of the lens is facing upwards. The ciliary body and the sclera are clearly visible.
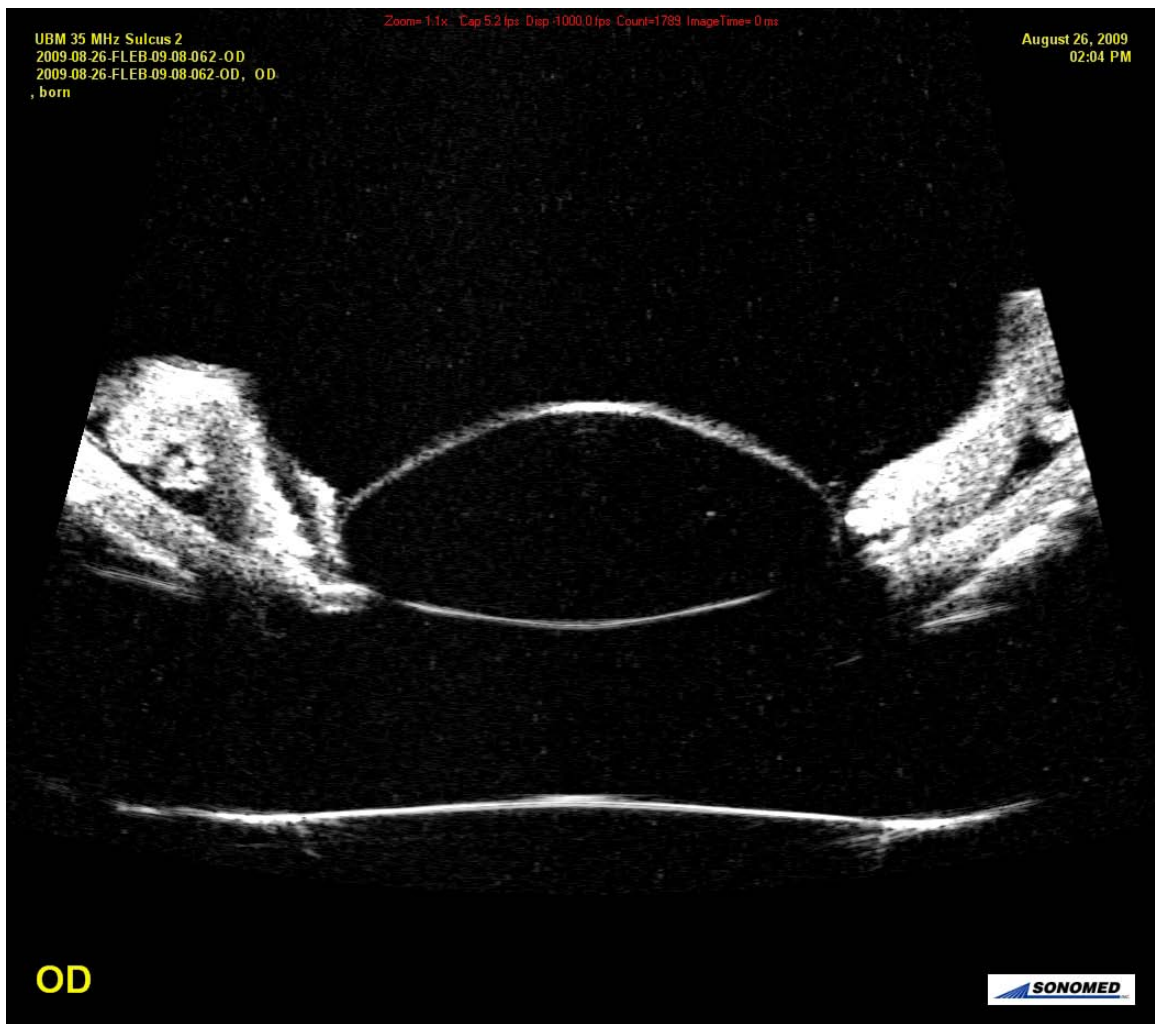
Figure 3.7: An example of a B-Mode image. Multiple A-Mode signals are combined to form an image. Figure shows a 28 year old human crystalline lens that was 3 days postmortem.

3.3.7   Ultrasound Bio-Microscopy

Visualization of tissue at microscopic resolution, using ultrasound, is referred to as Ultrasound BioMicroscopy (UBM), a term that is analogous to Optical BioMicroscopy, a well established optical method for visualizing living tissue in vivo (Foster, et al., 2000). Other terms used are "Ultrasound Backscatter Microscopy", "High Frequency Ultrasound" and "Very High Frequency Ultrasound". UBM transducers produce ultrasonic waves in the frequency range of 15 MHz to 100 MHz.

The principal components of a UBM are shown in Figure 3.8. A UBM is similar to a conventional B-mode imaging system, except that the operating frequency is approximately an order of magnitude higher. The transducer is moved linearly or angularly to emit and collect data. Motion systems can range from a stepping motor-controlled micro positioning stage to DC servo systems with custom actuators. A high voltage (20 – 200 MHz, 100-200 V peak to peak) pulse is used to excite the transducer. The resulting ultrasound pulse is transmitted through the tissue and the backscattered signal is detected by the same transducer. This signal is logarithmically amplified, its envelope is detected and it is converted from analog to digital format. The digital signal is processed by the Digital Signal Processor (DSP), where the ultrasonic image is reconstructed. A scan conversion algorithm is employed for the digital reconstruction when signal is obtained from sector scanning transducers to convert samples obtained in the Polar grid to a Cartesian grid. The images are then displayed (Figure 3.7) and stored.

Most clinical UBMs use 30-50 MHz transducers which provide a resolution of 30-70 μm and penetration of 4-10 mm (Foster, et al., 2000). This range is highly suitable for imaging the skin, cartilage and the anterior segment of the eye.
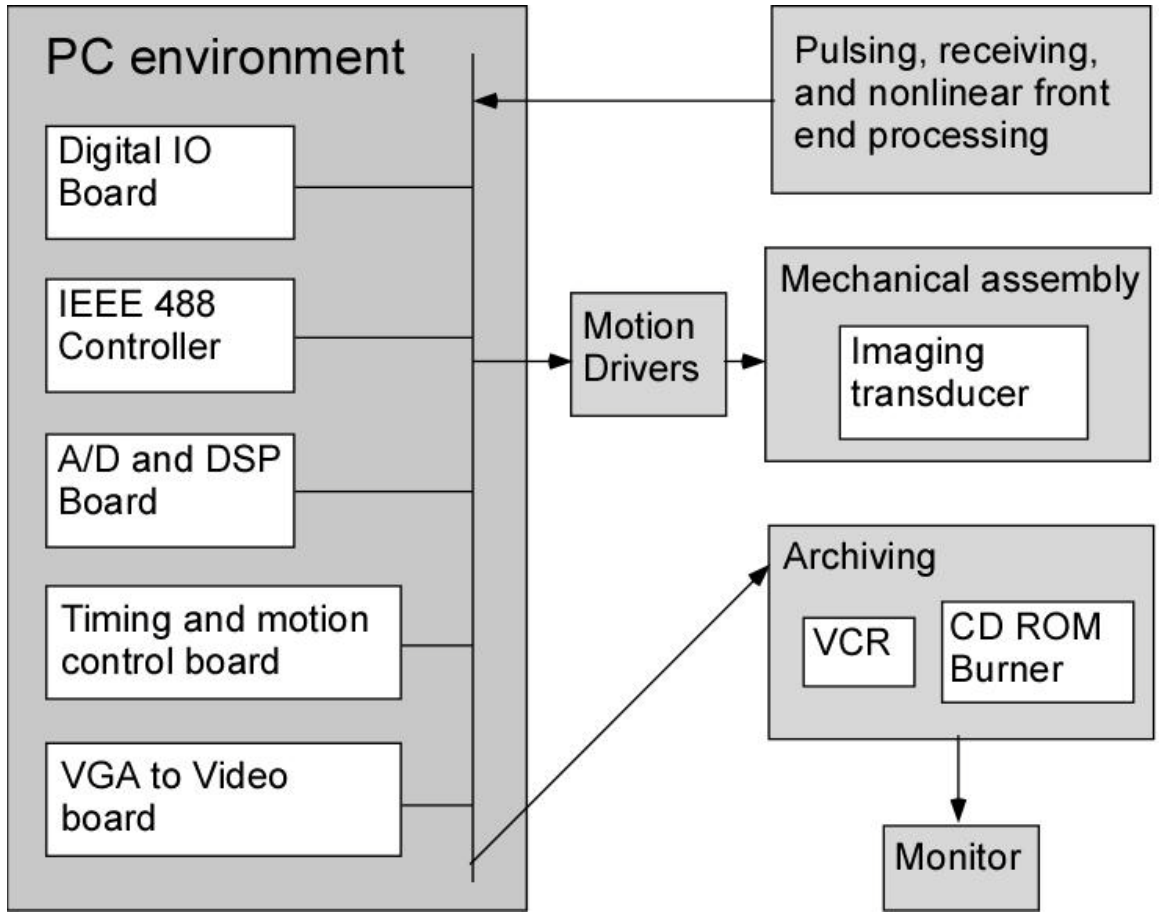
Figure 3.8: Simplified block diagram of an ultrasound biomicroscope (adapted from Foster, et al. 2000).

3.4 UBM in Anterior Segment Imaging

Vital structures of the eye fall within the range of the UBM, making the eye an ideal candidate for UBM imaging. The application of UBM in anterior segment imaging of the eye has been well documented (Pavlin and Foster 1995). The cornea, the sclera, the corneo-scleral junction and the scleral spur are some of the ocular anatomical structures and landmarks that can be well visualized by the UBM. UBM has proven to be very useful in the field of glaucoma especially in determining types of glaucoma caused by structural abnormalities of the anterior segment such as angle closure glaucoma and infantile glaucoma. It is also used to examine the iris and ciliary body for cysts and tumors (Byrne and Green 2002; Coleman et al., 2006, 2009).

Sequential 2-D images can be combined with computerized reconstruction software to produce 3-D images. Three-dimensional ultrasonography was first used by Coleman et al., (1992) to measure volume changes in ocular tumor growth.

High frequency UBM has been established as an important tool for investigating anterior segment structures. In the laboratory 2-D UBM has been used extensively in the study of accommodation and presbyopia in non human primates, in vivo (Glasser and Kaufman 1999; Croft, et al., 2006, 2009). Recently 3-D UBM has been used to characterize the ciliary body in human cadaver eyes (Silverman, et al., 2001) to monitor accommodative ciliary muscle function in the human eye in vivo (Stachs, et al., 2002), to assess accommodating intraocular lenses (Stachs, et al., 2005) and to investigate the zonules and the ciliary body in enucleated human eyes for numerical modeling of accommodation (Stachs, et al., 2006).
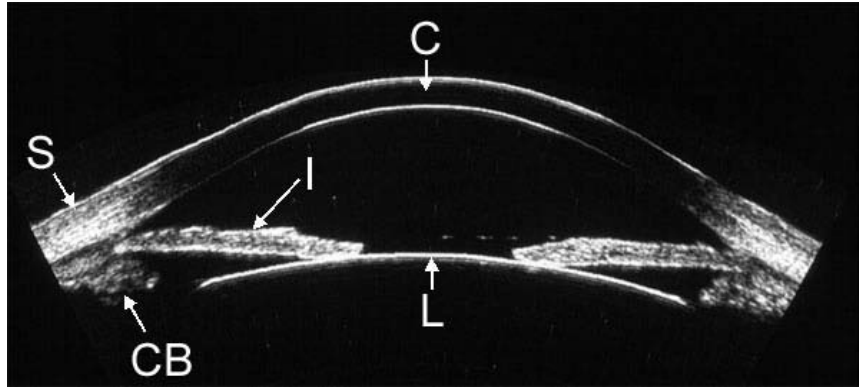
Figure 3.9: High-resolution ultrasound image of the anterior segment obtained with 50 MHz transducer and arc-scan geometry. Visualized structures include the cornea (C), sclera (S), iris (I), anterior lens surface (L) and ciliary body (CB). (Coleman et al., 2005).

Figure 3.9 shows a high resolution 2-D UBM image of the anterior segment of the human eye obtained with a 50 MHz transducer and arc-scan geometry. Visualized structures include the cornea (C), sclera (S), iris (I), anterior lens surface (L) and ciliary body (CB). (Coleman et al., 2005). The main problems associated with using 2-D images of ciliary muscle arise due to the dynamics of the accommodative mechanism. During the process of accommodation the muscle moves and imaging of the same cross-sectional plane is difficult to accomplish. The presence of ciliary processes compounds the problems of 2-D imaging. Figure 3.10 (Stachs et al., 2002) shows two radial sections S1 and S2 depicting ciliary muscle with and without processes. Differentiation of these structures is necessary to compare similar ciliary body sections. 3-D imaging provides information regarding the spatial localization of the ciliary muscle. Using this information Stachs et al., (2002) were able to show that the muscle moved towards the lens during accommodation and that muscles with processes have a greater displacement than those without.
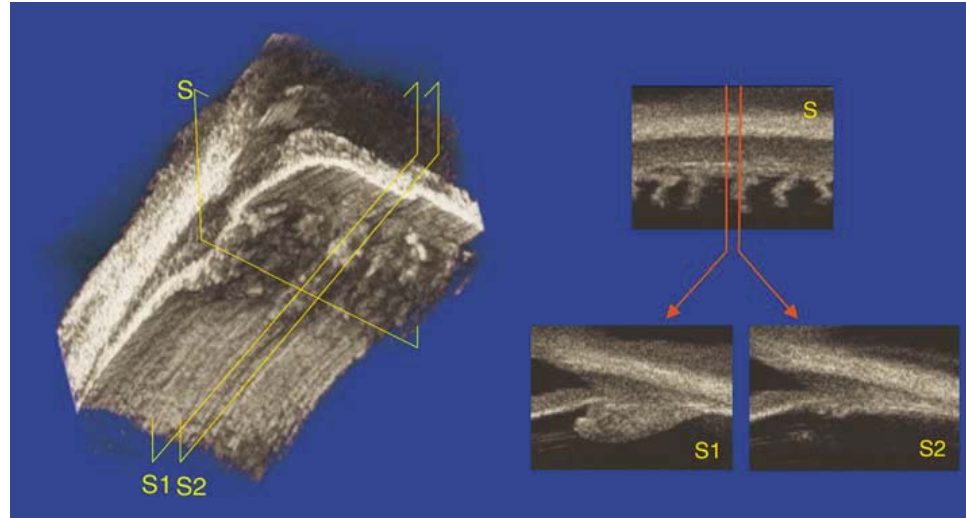
Figure 3.10: Different sections across the in vivo human ciliary body are shown. Depicted are sections in transverse direction (S) across the ciliary muscle with ciliary processes (S1) and only the ciliary muscle (S2). (Stachs et al., 2002).

Three-dimensional UBM is a powerful tool to study accommodation and presbyopia, especially for the characterization of the ciliary body. The Sonomed VuMax UBM (Lake Success, NY) will be used to image ocular structures in the lens stretcher. The ciliary muscle images obtained will be compared to published in vivo data of the ciliary muscle.

3.5 The Sonomed VuMax UBM

The Sonomed VuMax UBM will be used to measure the speed of sound through the lens and to image the lens and the ciliary muscle in three dimensions in EVAS-II. The Sonomed VuMax is a high frequency ultrasonic B-Scan imaging system for ophthalmologic diagnosis (Figure 3.11). The VuMax hardware consists of an emitter/receiver and scan converter mounted on a PCI-format circuit board, a cable harness and a water-path probe with two interchangeable transducers of center

frequencies of 35MHz and 50MHz. Optional 10MHz transducer for the orbit and 20MHz transducer for the globe are also available. The transducers are driven in an angular fashion by a DC servo motor located in the water path probe. The board is mounted in a PC (Personal computer), which provides the platform for the software and hardware. The VuMax software runs on Windows XP Operating System.

The 35 and 50 MHz transducers are made of gold-coated polyvinylidene fluoride (PVDF). They are spherically focused single element transducers with a focal length of 10 mm. The transducer is excited with a 127V pulse. The transducer is angularly rotated over a 30 degree sector to obtain multiple A-scans (lines) or a single B-scan (frame). Each frame is composed of 253 A-lines and each A-line has 1820 points. The frame acquisition rate is 5 per second. The theoretical axial resolution of the 35 MHz transducer is 0.022 mm and that of the 50 MHz transducer is 0.015 mm in tissue. The lateral resolutions for the two transducers are 0.42 mm and 0.37 mm respectively. The scan depth is 15 mm.
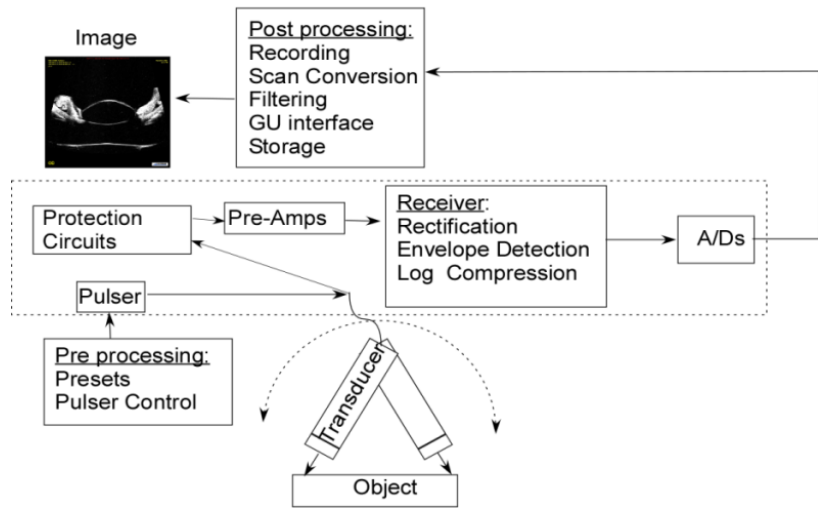
(a)   **(b)**

Figure 3.11: (a) VuMax high resolution ultrasound system from Sonomed Inc. (b) Schematic depicting the VuMax UBM. The transducer has a pulser, transmit/receive switch, pre-amplifiers and analog to digital converters. The receiver processes the data for optimal display and the scan converter produces the output image rendered on the monitor.

CHAPTER 4. MEASUREMENT OF SPEED OF SOUND IN THE LENS

4.1 Overview

Speed of sound will be measured in the human crystalline lens. These measurements will be used to help reconstruct UBM images of the lens to determine if UBM imaging can be used for lens biometry. Data obtained will be used to investigate if speed of sound is influenced by the age of the lens and if speed of sound can be predicted with a mathematical model.

4.2 Speed of Sound

4.2.1 Overview

Sound is a mechanical wave propagating through a continuous elastic medium. When ultrasound waves cause displacement of particles in the propagation direction they are called longitudinal waves. When the particle movement is at right angles to the direction of propagation they are referred to as transverse or shear waves. Ultrasound waves travel as longitudinal waves in fluids and gases and as both longitudinal and transverse waves in solids. For both longitudinal and transverse acoustic waves, the one dimensional wave equation is mathematically described as:

$$\frac{\partial^2 p}{\partial x^2} - \frac{1}{c^2}\frac{\partial^2 p}{\partial t^2} = 0 \qquad\qquad \text{Equation 4.1}$$

where p is the sound pressure along propagation direction x, t is time and c is the speed of sound (Hill, et al., 2002). The speed of sound depends on the mechanical properties of

35

the medium. In a medium, the speed of sound varies with temperature and frequency. The speed of sound was first described by Newton as (Poynting and Thomson, 1920):

$$c = \sqrt{\frac{B}{\rho}}$$ Equation 4.2

where B is the bulk modulus and ρ is the density of the material. The speed of sound in air, water, polydimethylsiloxane (PDMS) and some ocular tissue is presented in Table 4.1.

Medium	Speed of sound (m/s) at 37ºC
Air	330
Water	1524
PDMS*	1015 (Room temperature)
Cornea	1639
Lens	1641
Aqueous Humor	1532
Vitreous Humor	1532

Table 4.1: Speed of sound in air (Bushnerg, et al., 2001), water at 37ºC (Willard, 1947), biological tissues of interest at 37ºC (Coleman, et al., 2006) and PDMS at room temperature (Delides and King, 1979). (*Sound velocity of PDMS did not show any dependence on the crosslink density).

4.2.2 Speed of Sound in Liquids and Gases

Newton's equation, when applied to air yielded a value much lower than the measured value. Laplace hypothesized that sound vibrations were too rapid to allow thermal equilibrium, and the variations in density were adiabatic, not isothermal (Poynting and Thomson, 1920). He proposed the following equation for speed of sound (Newton-Laplace equation):

$$c = \sqrt{\frac{1}{\kappa \rho}}$$ Equation 4.3

where κ is the adiabatic compressibility. This equation produced results that agreed with experimental data.

When an equilibrium volume V_0 is subjected to an increase in pressure dp, under adiabatic conditions, the volume decreases by dV. The adiabatic compressibility is defined as:

$$\kappa = -\frac{1}{V_0} \left.\frac{\partial V}{\partial p}\right|_S$$ Equation 4.4

where S indicates a constant entropy corresponding to a reversible adiabatic process (Cobbold, 2007). The adiabatic Bulk Modulus K is the inverse of the adiabatic compressibility (Cobbold, 2007):

$$K = \frac{1}{\kappa}$$ Equation 4.5

The adiabatic compressibility and density of water at 20ºC are 0.4559 /GPa and 998.2 kg/m^3 (Cobbold, 2007). Substituting these values in Equation 4.3 yields a value of 1482.36 m/s for the speed of sound in water. Willard's (1947) measurements yielded a value of 1485.55 m/s.

For a fluid mixture, speed of sound is given by the additive rule:

$$\frac{1}{c} = \frac{1}{c_A}\varphi_A + \frac{1}{c_B}\varphi_B$$ Equation 4.6

where c_x and φ_x represent the speed of sound and the volume fractions of the two fluids A and B (Pfeiffer, et al., 2008).

4.2.3 Speed of Sound in Solids

When a compressive axial stress is applied to a thin rod, the decrease of the length of the rod will be accompanied by an increase in the diameter of the rod. In this case the speed of sound in the rod is given by:

$$c = \sqrt{\frac{E}{\rho}}$$

Equation 4.7

where E is the Young's modulus of the rod (Cobbold, 2007). If, however, additional constraining compressive stresses are applied, to prohibit a change in the rod diameter, the rod behaves in a more rigid manner. The speed of the longitudinal wave is then given by:

$$c_L = \sqrt{\frac{\chi}{\rho}}$$

Equation 4.8

where χ is the axial modulus (Cobbold, 2007). The axial modulus is related to Young's modulus through the equation:

$$\chi = \frac{E(1-v)}{(1-2v)(1+v)}$$

Equation 4.9

where v is the Poisson's ratio (Cobbold, 2007). The speed of the transverse wave depends on the shear modulus (G) and is given by (Cobbold, 2007):

$$c_T = \sqrt{\frac{G}{\rho}}$$

Equation 4.10

where G can be expressed in terms of E and v by:

$$G = \frac{E}{2(1+v)}$$

Equation 4.11

This model provides a good approximation of the speed of sound in hard tissue. For instance, the Young's modulus, Poisson's ratio and density of the fresh bovine bone are 22 GPa, 0.4 and 1960 kg/m^3 respectively (Cobbold, 2007). Substituting these values in Equation 4.8 and Equation 4.9 yields a value of 4904.33 m/s for the longitudinal speed of sound in bone. Goss, et al., (1978) reported a value of 4030±110 m/s.

4.2.4 Speed of Sound in Soft Biological Tissue

The speed of sound in soft biological tissue has been shown to correlate with concentration of tissue constituents, particularly, to protein concentration. Speed of sound in albumin solutions was found to increase in direct proportion to the protein concentration (Carstensen, et al., 1953). Additionally the structure of tissue has been shown to contribute to attenuation of sound (Pauly and Schwan, 1971). Goss, et al., (1980) investigated the contribution of globular and structural proteins to speed of sound in several kinds of tissue and derived an empirical model for the relationship between speed of sound and protein concentration:

$$c = M \times P + N \times K + c_0$$
<div style="text-align: right">Equation 4.12</div>

where c is the speed of sound in tissue, P and K are the wet weight percentages of the globular protein and collagen in the tissue, M and N are constants and c_0 is the speed of sound when P and K are zero. M and N were determined to be 3.2 and 6.5 respectively at 27ºC.

4.2.5 Speed of Sound in the Lens

In this section the models discussed above are applied to the lens, to determine which model is most suitable to predict speed of sound in the lens.

The commonly accepted value for speed of sound in the human crystalline lens is 1641 m/s (Jansson and Kock 1962) independent of age. The average density of the lens is 1.096 gm/cm^3 (Rosen, et al., 2006). The Poisson's ratio for the lens cortex and nucleus is generally assumed to be 0.49 (Burd, et al., 2002). Substituting these values in Equation 4.8 and Equation 4.9 yields a value of 172 MPa for the Young's modulus in the lens. Age dependent values for Young's modulus are reported in literature for the nucleus, cortex (Fisher, 1971) and capsule of the lens (Krag et al., 1996) but not the whole lens. The values reported for the nucleus, cortex and the capsule range from 0.5 KPa to 3KPa for 20 to 60 year old lenses. The solid model for the speed of sound yields a Young's modulus value that is 3 orders of magnitude higher than values reported for the lens.

Using the liquid model for the speed of sound, and substituting reported values of speed of sound in the lens (1641 m/s; Jansson and Kock 1962) and lens density (1.096 gm/cm3; Rosen, et al., 2006) into Equation 4.3 and Equation 4.5 yields a value of 2.95 GPa for the adiabatic bulk modulus in the lens. This is comparable to reported values of 2.8 GPa for the lens cortex and 3.7 GPa for the lens nucleus as measured by Brillouin light scattering (Subbaram, et al., 2002). This analysis suggests that the model for speed of sound in liquids is a better model for the speed of sound in the lens. However, Brillouin light scattering is based on acoustical properties of the tissue and therefore, this method is not an independent verification of lens adiabatic bulk modulus.

If the lens behaves as a fluid mixture, the volume fractions of water and proteins will affect the speed of sound. The lens is composed of 66% water, 33% proteins and 1% lipids. The average density of proteins is 1.37 g/cm^3 (Lodish, et al., 2007). Substituting reported values of speed of sound in water (1524 m/s at 37°C; Willard 1947) and in the

lens (1641 m/s; Jansson and Kock 1962) in Equation 4.6 and Equation 4.3 produces a value on the order of 10^{-10} m^2/N for protein adiabatic compressibility, which matches reported values (Gavish, et al., 1983). The fluid mixture model suggests that the speed of sound in the lens is dependent on protein concentration and will vary locally according to protein distribution.

Goss, et al.,'s (1980) empirical model (Equation 4.12) when applied to the lens, assuming 1524 m/s as speed of sound in water (Willard, 1947), 33% as protein concentration (globular proteins) and no collagen (structural proteins), yields 1629.6 m/s as the speed of sound in the lens. This value is within 1% of the accepted value for speed of sound in the lens.

De Korte, et al., (1994b) measured speed of sound on 1mm thick lens slices across both equatorial and optical axes of human and porcine lenses at 20ºC. They used data published by Siebinga, et al., (1991) about protein content distribution in an 8 year old human lens, to calculate the speed of sound across the human lens profile. They also used measured values of protein content in porcine lenses using Raman microspectroscopy to calculate speed of sound in porcine lenses. Figure 4.1 shows the measured (*) and calculated (+) values of speed of sound across the equatorial half-profile in human and porcine lenses. The calculated values were highly correlated to the measured values (p < 0.01).

In summary, data from literature indicate that speed of sound in the lens is dependent on local protein concentration and that the fluid mixture model and Goss, et al.,'s (1980) empirical model can be used to predict speed of sound in the lens.
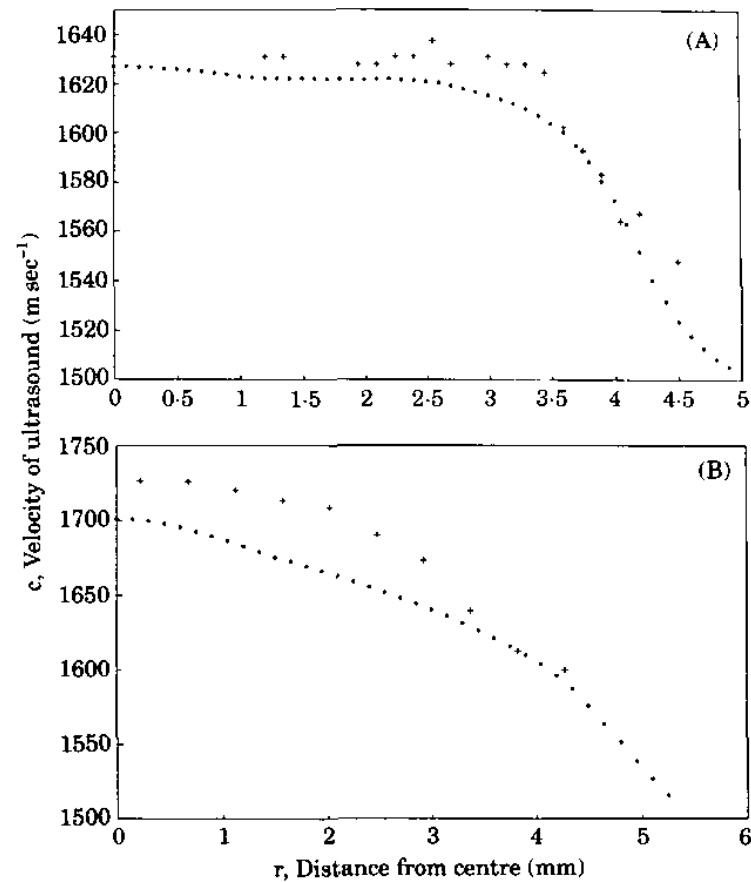
Figure 4.1: Figure is from De Korte, et al., (1994b). Speed of sound across equatorial half-profile, measured (*) and calculated (+) in (A) human lens and (B) porcine lens.

4.3   Literature Review of Speed of Sound Measurement in the Lens

The majority of the measurements of propagation velocities of sound through the lens, reported in literature, have been made using one of two common methods: Time of Flight (TOF) measurement and Interferometry.

The TOF measurement method (Figure 4.2) involves placing a reflector under the sample, immersed in a medium of known speed of sound, at a constant distance from the

transducer and measuring reflection times from the reflector with and without the sample

(Jansson and Kock, 1962). The speed of sound in the sample is then given by:

$$C_{SAMP} = C_{MED} \left[\frac{(t_R - t_s)}{(t_2 - t_1)} + 1 \right]$$
  Equation 4.13

where C_{SAMP} is the speed of sound in the sample, C_{MED} is the speed of sound in the medium, t_R is the time of flight from the transducer to the reflector without the sample, t_S is the time of flight to the reflector through the sample, t_1 and t_2 are the times of flight to the first and second surfaces of the sample.
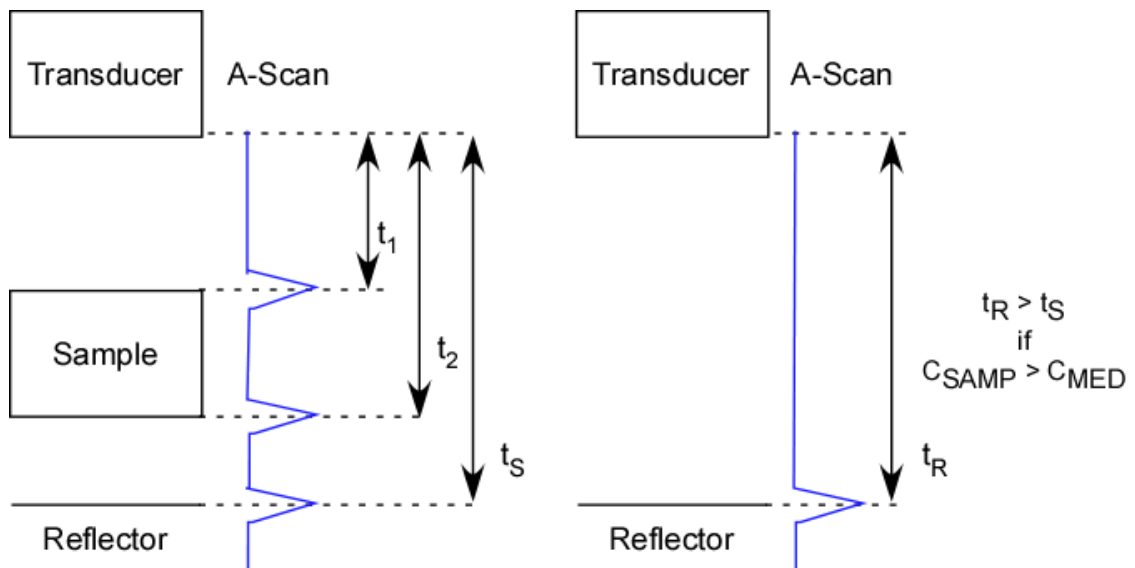
Figure 4.2: Schematic illustration of the principle of the Time of Flight technique to measure speed of sound in a sample. The sample is immersed in a medium of known speed of sound and an A-scan is recorded to measure the time of flight at the boundaries. The sample is then removed, without changing the distance of the transducer to the reflector, and time of flight is measured again. The time t_R will be greater than the time t_S if speed of sound in the sample (C_{SAMP}) is greater than speed of sound in the surrounding medium (C_{MED}).

In the interferometric method, sound waves are simultaneously directed through a sample of known length (d_s) and a water column. The active distance of the water column (d_w) from a reflector is adjusted so that the echo from the reflector will overlap the echo from the test object, producing a single echo whose amplitude is equal to the sum of the amplitudes of the two echoes. With known values of speed of sound in water (C_W), the speed of sound in the sample can be determined by (Oksala and Lehtinen, 1958):

$$C_{SAMP} = C_W \frac{d_s}{d_w} \qquad\qquad \text{Equation 4.14}$$
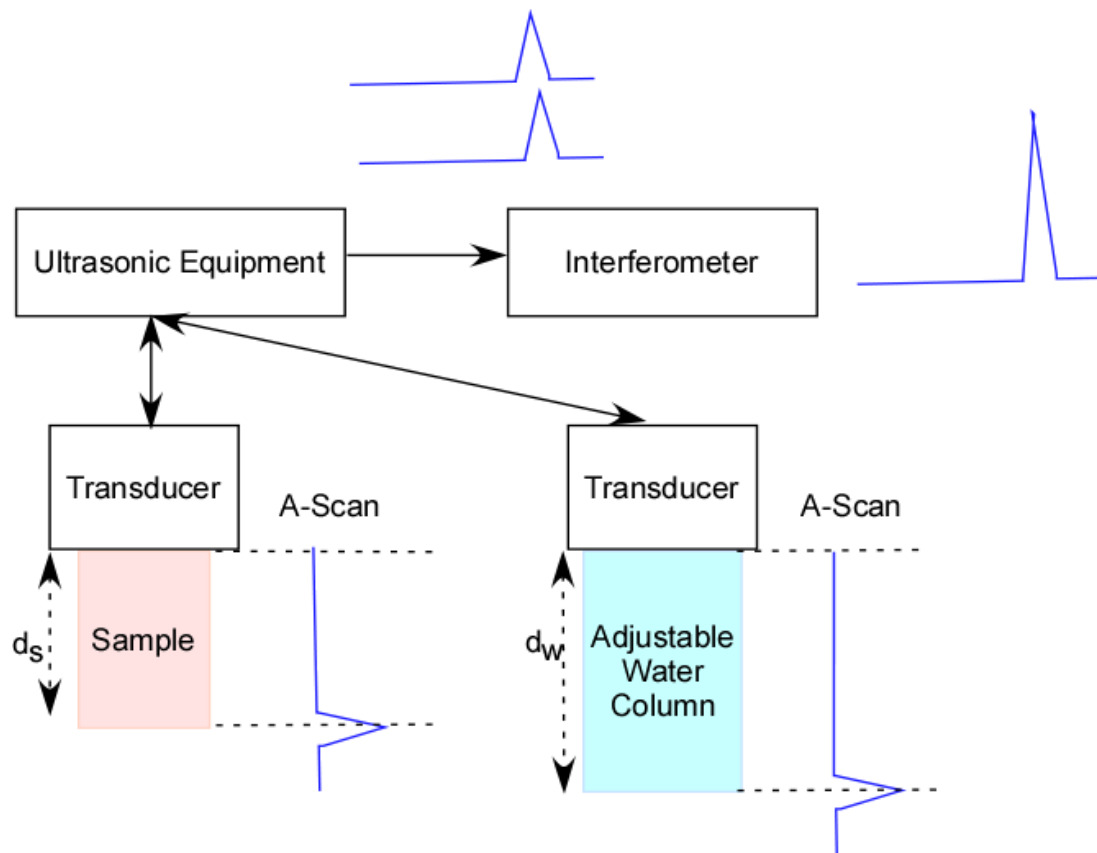
Figure 4.3: Schematic illustration of the principle of interferometry to measure speed of sound in a sample.

Authors	Year	Species	Method	Temperature (degrees C)	Speed of Sound (m/s)	N	Age Range	Media	Age Dependence	Frequency (MHz)
Begui	1954	Bovine	Resonance	Room Temperature	1616	9	8 - 12 weeks			5
Oksala & Lehtinen	1958	Bovine	I	22	1650			distilled water		4
Jansson & Sundmark	1961	Bovine		37	1680	30		Saline		
Jansson & Sundmark	1961	Human	I	37	1641	11	2 - 75 years	Saline		4
Jansson & Kock	1962	Human	TOF	37	1640	12	5 - 81 years	Saline		4
Rivara & Sanna	1962	Human		37	1647.11 ± 3.53	3		Saline		
Rivara & Sanna	1962	Porcine	TOF	37	1672.75 ± 3.12	3		Saline		4
Coleman , et al.,	1975	Human (Cataractuous)		37	1629 ± 38	50		Saline		
Coleman , et al.,	1975	Human	TOF	37	1659	4	3 - 24 months	Saline		15
Chivers, et al.,	1984	Human	Variation of TOF	22	1558	2	Unknown, 73 years			10
Thijjsen , et al.,	1985	Human		Room Temperature	1620 ± 3	4				
Thijjsen , et al.,	1985	Human		37 (Extrapolated)	1637 ± 3	4				10
Thijjsen , et al.,	1985	Porcine	TOF	Room Temperature	1651 ± 2					

46

Authors	Year	Species	Method	Temperature (degrees C)	Speed of Sound (m/s)	N	Age Range	Media	Age Dependence	Frequency (MHz)
DeKorte, et al.,	1994a	Human		20	1590.1	13	19 - 86 years	Saline	1586.7 + 7.7E-2 * Age	
		Porcine	TOF	20	1633.3	6	4 months	Saline		20
Beers & van der Heijde	1994	Human	TOF (In Vivo)		1641 ± 35.3 (15-29 years) 1656 ± 46.8 (30-45 years)	24	15 - 44 years	In vivo	1636.4 + 0.37 * Age	10
Tabandeh, et al.,	2000	Human	TOF	22	1641.2 ± 7.2	37	60-92 years			10
Lafon, et al.,	2006	Bovine	TOF		1695	10				3.5
Huang, et al.,	2007	Porcine	TOF	25	1639.8 ± 4.2	50		Saline		35

Table 4.2: Review of literature for speed of sound in the lens. (I = Interferometry, TOF = Time of Flight)

A review of literature for speed of sound in the lens has been summarized in Table 4.2. The first known record of sound speed in ocular tissue was published in 1954 by Begui. He determined the average speed of sound in bovine lenses (n=9, age = 8-12 weeks) at room temperature as 1616 m/s using a 5MHz ultrasonic interferometer. He used a resonance method to measure the speed of sound. When, the distance between the transducer and reflector, with the sample interspersed between the two, is continuously altered, the amplitude of the signal detected will be highest when the distance is a multiple of half wavelength of the source signal. The speed of sound can be calculated from the known frequency and the change in distance necessary to get from one peak to the next.

Oksala and Lehtinen (1958) measured sound speed in bovine lenses using the principle of interferometry. They measured the speed of sound in bovine lenses as 1650 m/s using a 4MHz ultrasound wave at 22ºC on lenses obtained from freshly slaughtered cattle. The lenses were immersed in distilled water and slightly compressed between the container and the ultrasonic equipment.

Jansson and Sundmark (1961) used the same method used by Oksala and Lehtinen (1958) to measure sound velocity in bovine and human lenses. They recorded these measurements at 37ºC and reported speed values of 1680 m/s for bovine (n=30) and 1641 m/s for human (n=11, age = 2-75 years) lenses. The lenses were immersed in saline solution and slightly compressed between the container and the ultrasonic equipment. Jansson and Sundmark (1961) were the first scientists to measure speed of sound in the human crystalline lens.

Jansson and Kock (1962) used the same equipment as Jansson and Sundmark (1961) but used the TOF measurement method. They placed the lens in a cuvette and measured the echoes from the bottom of the cuvette filled with saline solution, with and without the human lens, maintaining the same distance between the transducer face and the bottom of the cuvette. They reported a value of 1641 m/s for human lenses (n=12, age = 5-81 years) at 37ºC.

Rivara and Sanna (1962) used the same method on human (n=3) and porcine (n=3) lenses at 37ºC. They reported 1647.11 ± 3.53 m/s and 1672.75 ± 3.12 m/s for the two species respectively. In both these studies the lens was in contact either with the ultrasound transducer or the cuvette and immersed in saline solution.

In 1975 Coleman, et al., measured speed of sound in cataractous human lenses. They used the same method as the previous two studies. They used a 15MHz transducer made of lithium sulfate, focused at a distance of 35mm. They measured an average speed of 1629 ± 38 m/s for 50 cataractous lenses and a higher value of 1659 m/s for normal young lenses (n=4, age = 3 – 24 months). With increasing age, the lens becomes stiffer and sound is expected to travel faster than in young lenses. However, the data suggests that other factors such as increase in water content may be responsible for the counterintuitive results.

In 1984 Chivers, et al., reported a value of 1558 m/s in human lenses at 22ºC. They used a 10MHz transducer on 2 human lenses; one was of unknown age and the other, 73 years old. The measurement method they employed was a variation of the TOF method described earlier. They measured the TOF to the reflector, with the sample

interspersed between the two, moved the reflector away from the transducer by a distance, Δl, and introduced a delay in time, Δt, that was needed to return the pulse to the original distance. Speed of sound was then calculated by the formula:

$$C_{SAMP} = \frac{2\Delta l}{\Delta t}$$
<div align="right">Equation 4.15</div>

In 1985 Thijssen et al., using the TOF measurement method, made measurements on 4 human lenses, with a 10 MHz transducer, at room temperature and extrapolated the data to 37ºC as 1637 ± 3 m/s. They reported a value of 1651 ± 2 m/s for porcine lenses at room temperature.

De Korte, et al., (1994a) were the first to perform an age-dependent study using a scanning acoustic microscope with a 20 MHz transducer. They used the TOF measurement technique to determine sound speed. They did not use intact lenses, but instead used 1mm thick slices. They used tissue from 13 human lenses in the age range of 19 to 86 years at 20ºC. They reported an age-dependent value of 1586.7 + 7.7E-2 * Age (p=0.31), which was not statistically significant.

Beers and van der Heijde (1994) were the first and only group who measured sound speed in the lens in vivo. Their method was based on comparing the time for sound to travel through the lens in various accommodative states. Assuming that sound velocity of the lens and the axial length of the eye do not change during accommodation, and with knowledge of sound velocity in the anterior chamber and the vitreous, the sound velocity in the lens could be computed. They reported a value of 1636.4 + 0.37 * Age (p>0.2) which was also not statistically significant.

In recent years Tabandeh, et al., (2000), Lafon, et al., (2006) and Huang, et al., (2007) reported measurements on human, bovine and porcine lenses respectively, using the TOF measurement technique. Tabandeh, et al., (2000) reported 1641.2 ± 7.2 m/s using a 10 MHz ultrasound transducer at 22ºC in human lenses (n=37, age = 60-92 years). Lafon, et al., (2006) reported 1695 m/s in bovine lenses using a 3.5 MHz ultrasound transducer. Huang, et al., (2007) reported 1639.8 ± 4.2 m/s in porcine lenses (n=50) using a 35 MHz ultrasound transducer at 25ºC. In all these experiments the lens was immersed in saline solution.

Of the 12 ex vivo studies discussed above, 8 used the TOF method, 1 used a variation of the TOF method, 2 used the interferometric method and 1 used a resonance method to measure speed of sound. In the interferometric method the sample has to be in contact with both the transducer and the reflector. This approach causes the lens to be compressed, which could alter the speed of sound measured. In the TOF method it is possible to suspend the sample in a medium such that neither surfaces come in contact with the transducer or the reflector. However, none of the ex vivo studies have used this approach.

Only three studies that employed the TOF technique measured the speed of sound at 37ºC. Of these, Coleman, et al., (1975) used cataractous lenses and very young lenses. Rivara and Sanna (1962) used only 3 lenses, whose ages were not provided. The most reliable and relevant study was performed by Jansson and Kock (1962). They reported a value of 1641 m/s, which is the accepted value for the speed of sound in the lens. However, their samples were immersed in saline solution. Hydration control is important to preserve the shape and mechanical properties of the ex vivo lens. Water uptake by the

lens leads to swelling and capsular separation. Evidence of swelling has been shown by Augusteyn, et al., 2006, who also showed that culture media which contain nutrients are more effective than salt solutions at maintaining lens volume. A change in lens volume, indicating water uptake may alter the speed of sound in the lens.

The lens is primarily composed of water and proteins. These proteins are not distributed homogeneously in the lens. If a fluid mixture model or Goss, et al.,'s (1980) empirical model is assumed for the speed of sound of the lens, the value would vary in both the optical and the equatorial axial directions. While the speed of sound variation along the optical axis cannot be measured on intact lenses, it is possible to measure the variation along the equatorial axis. De Korte, et al., (1994b) measured speed of sound across both axes on 1 mm thick slices. This measurement has not been made on intact lenses.

The experimental set up employed in the present study was designed to address these issues. Speed of sound will be measured across the equatorial profile of the lens and Goss et al.,'s (1980) empirical model will be used to predict protein concentration of the lens across the equatorial profile.

4.4   Experimental Set up

The lens was mounted in a manual lens stretcher (MLS) (Parel, et al., 2004, Bernal, et al., 2006). The stretcher consists of 8 shoes whose diameter can be manually stretched by 4 mm. Figure 4.4 illustrates the tissue preparation protocol. The scleral shell of the whole globe was glued onto the shoes and the posterior pole, the cornea and the iris were removed. The sclera in between the shoes was carefully dissected, to allow radial

outward movement of the shoes. This left the lens, the zonules and the ciliary body intact. The MLS was then placed in a temperature controlled cell (Figure 4.5). The posterior surface of the lens was made to face upwards, because preliminary experiments revealed that better images of the lens were produced in this orientation. A glass window was placed under the MLS in the cell. The window was placed at 4 mm from the center of the MLS. The cell was filled with a preservation medium, Dulbecco's Modified Eagle Medium (DMEM) (Augusteyn, et al., 2006). The medium was heated to 37ºC in the cell with a heater (Omegalux, KHR-3/10, 10 W/in^2) affixed to the bottom of the cell. A thermocouple (Omega, 5SC-TT-T-36-72) immersed in the cell measured the temperature and a temperature controller (Omega, CN1A-TC) maintained the temperature at 37ºC ($\pm$ 0.25%). The experimental set up is shown in Figure 4.6.

(a) (b)
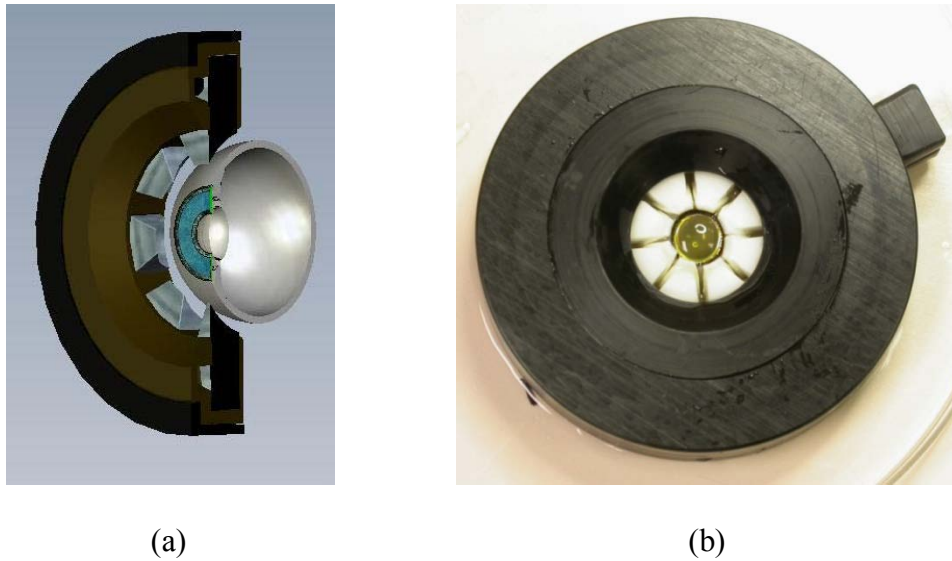
Figure 4.4: Tissue preparation: (a) The globe is glued to the shoes in the MLS. (b) The posterior pole, the cornea and the iris are removed. The sclera in between the shoes is dissected, leaving the lens, the zonules and the ciliary body intact.
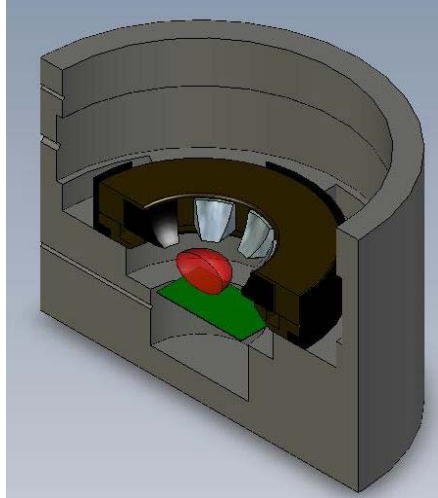
Figure 4.5: Figure shows cross-section of the temperature-controlled cell. The MLS is placed such that the posterior surface of the lens faces upwards. A glass window is placed under the MLS. The window is placed at 4 mm from the center of the MLS.
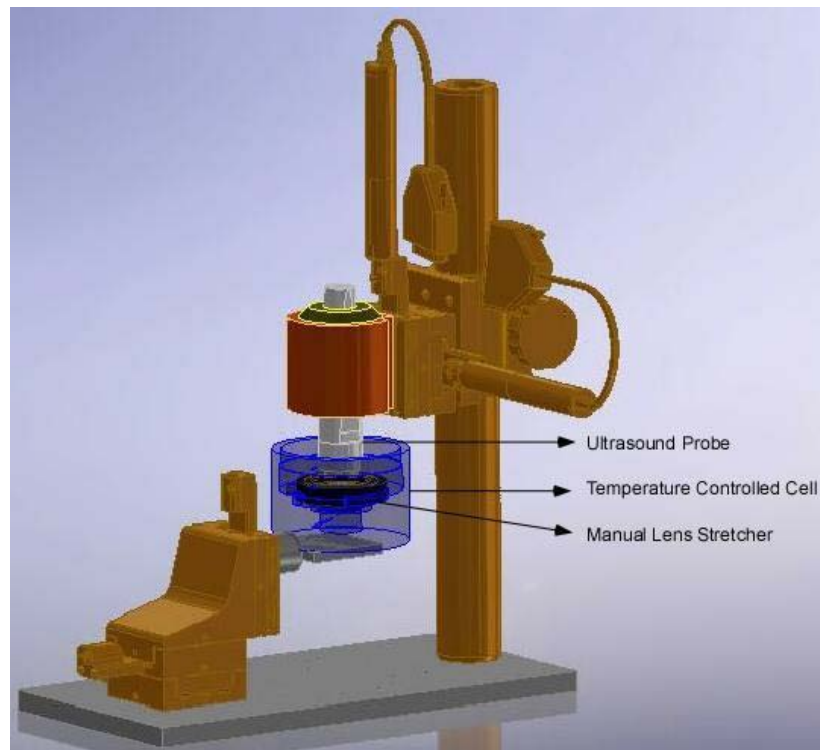
Figure 4.6: Experimental set up to measure speed of sound in the lens. The ultrasound probe is mounted on a linear translation stage. The lens, mounted in the manual lens stretcher, is placed in the temperature controlled cell.

To measure speed of sound in the lens (Figure 4.7), the transducer was immersed in DMEM in the cell and the time of flight was measured between the transducer and the posterior surface of the lens (t_1), anterior surface of the lens (t_2) and the window (t_S). The position of the transducer was noted and the transducer was raised using a motion-controlled translation stage (Newport ESP301-3N). The MLS was removed from the cell and the transducer was brought back to the noted position. The actuators (TRA25-CC) of the motion controlled translation stage have a repeatability of 2 µm. For a 20 mm distance a variability of ±2 µm would introduce a 0.009% error in speed measurement. The time of flight to the window (t_W) was measured in DMEM. Three measurements were made per sample. If the speed of sound in DMEM (C_{DMEM}) is known, the speed of sound through the lens can be calculated as:

$$C_{LENS} = C_{DMEM} \left[\frac{(t_w - t_s)}{(t_2 - t_1)} + 1 \right] \qquad \text{Equation 4.16}$$

As an A-mode probe was not available, measurements were made with a B-Mode probe, and only the center A-line was used (Figure 4.8). Time of flight was calculated by counting the number of samples (N) to the A-mode peaks corresponding to the two lens surfaces and the window and dividing it by twice the sampling frequency (80MHz).

$$t = \frac{N}{2f} \qquad \text{Equation 4.17}$$

Experiments were repeated with the 35 MHz and the 50 MHz probes, for lens in the un-stretched and stretched conditions. To measure speed of sound across the equatorial profile of the lens, the transducer was moved linearly at a speed of 0.5 m/s and the center

line of each frame was used to reconstruct the entire lens. The Sonomed UBM obtains 5 frames per second, therefore speed of sound measurement was made at increments of 100 μm.
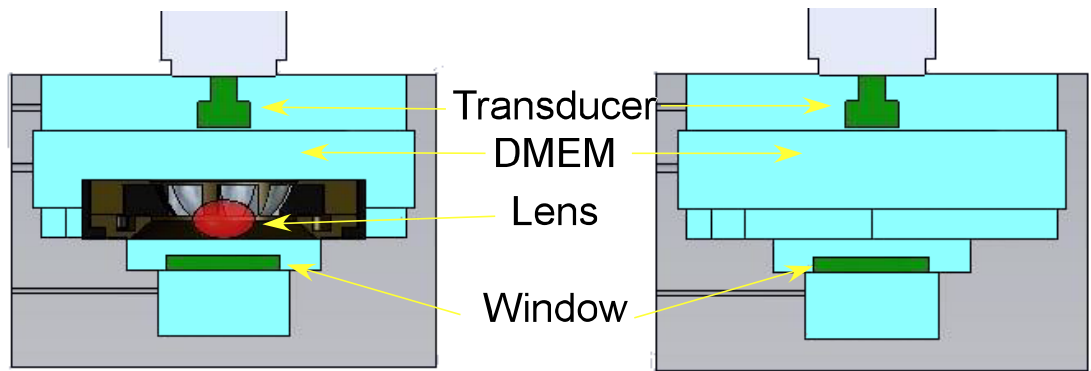
Figure 4.7: Time of flight is measured from the lens posterior surface, anterior surface and the window (left). The MLS is removed and time of flight to the window is measured without altering the distance from the transducer to the window (right).

(a)   (b)
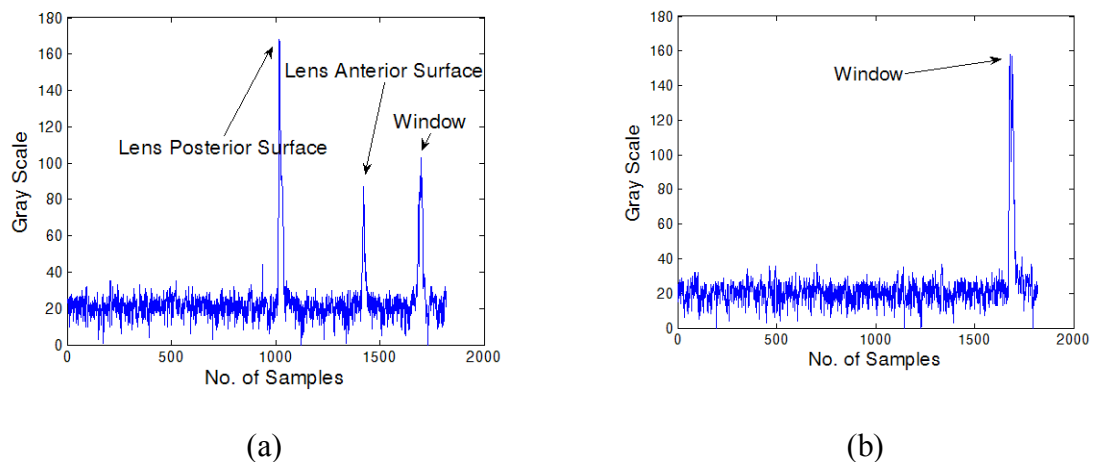
Figure 4.8: (a) A-Mode scan of the lens center. The three peaks correspond to the lens posterior and anterior surfaces and the glass window. (b) A-Mode scan of the glass window only. The time of flight was computed by dividing the number of samples corresponding to the peaks by twice the sampling frequency.

Speed of sound was measured in water and DMEM in the same cell. The transducer was immersed in the medium and the time of flight of the ultrasound signal was measured from the transducer to the glass window, at various distances between the two, with 0.5mm increments. The time versus distance information was plotted and a linear regression was performed. The inverse of the slope obtained from the linear regression is the speed of sound in the medium. Experiments were conducted with the 35 MHz and the 50 MHz probes at 37ºC.

4.5 Effect of Refraction on Speed Measurement

Speed measurement using the TOF method is valid at the center of the lens where there is no refraction and the distance travelled by the sound ray through the lens is the same as the distance travelled through water. However, away from the lens center, refraction changes the ray path and increases the distance travelled by the ray, introducing an error in speed measurement. This error depends on the distance to the window from the lens (Figure 4.7). To quantify the effect of sound refraction on the speed of sound measurement across the lens profile, speed measurement was simulated for the central 6 mm of the lens. The simulation was performed with MATLAB (Mathworks, Inc., Natick MA). The two lens surfaces were modeled with conic sections (Borja et al., 2009b). The equations for the anterior and posterior surfaces of the lens are given by:

$$z_A(x) = z_{0a} + \frac{x^2}{R_a + \sqrt{R_a^2 - p_a x^2}}$$

Equation 4.18

$$z_p(x) = z_{0p} + \frac{x^2}{R_p - \sqrt{R_p^2 + p_p x^2}}$$

Equation 4.19

where R_a and R_p are the anterior and posterior radii of curvature, p_a and p_p are the anterior and posterior shape factors and z_{0a} and z_{0p} are the anterior and posterior thicknesses of the lens. The age dependent equations for the curvature and shape factor given by Borja, et al., (2009b) and those for thickness given by Rosen, et al. (2006) were used in the simulations (Table 4.3).

Parameter	Age Dependent Equation
R_a	4.46 + 0.14 x Age (Age < 50)
	13.83 - 0.05 x Age (Age >=50)
R_p	-3.47 - 0.06 x Age (Age <57)
	-7.97 + 0.02 x Age (Age >=57)
p_a	4.84 - 0.56 x Age (Age < 26)
	14.7-0.25 x Age (Age >= 26)
p_p	-1.42 + 0.027 x Age
z_{0a}	-(1.65 + 0.0049 x Age)
z_{0p}	2.33 + 0.0074 x Age

Table 4.3: The age dependent equations for the curvature and shape factor (Borja, 2009b) and thickness (Rosen, et al., 2006) for the anterior and posterior surfaces of the human lens.
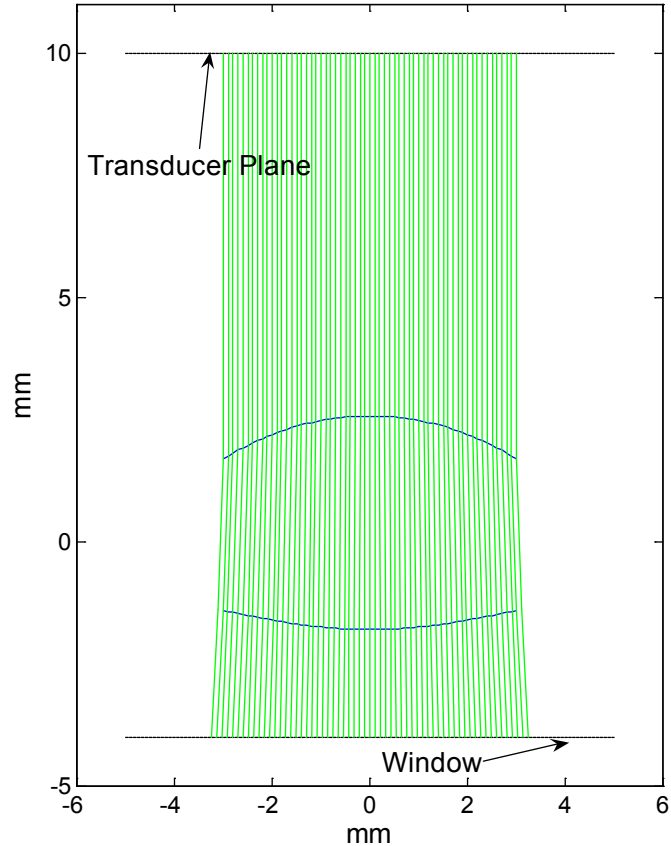
Figure 4.9: Simulation of sound wave refraction while measuring speed of sound across the central 6 mm of the lens. The speed of sound in the lens was assumed to be 1640 m/s. The window was assumed to be 4 mm away from the equatorial plane of the lens. Refraction causes sound waves to bend away from the optical axis at the two surfaces of the human lens.

The angles of refraction at the posterior and anterior surfaces of the lens were computed using Snell's law (Equation 3.5). The speeds of sound in DMEM and the lens were assumed to be 1548 and 1640 m/s respectively. The lens was assumed to have a uniform speed of sound. Figure 4.9 shows the lens model for a 32 year old lens and simulation of sound wave refraction. The distances along the refracted ray from the transducer to the posterior and anterior surfaces of the lens and the window were

computed. Times of flight to these surfaces were computed by dividing the distance by the speed of sound in the medium and the lens. Speed of sound in the lens was then calculated using Equation 4.13. Simulation was performed for various distances of the window from the lens equator starting at 2 mm up to 10 mm in increments of 2 mm (Figure 4.10). Refraction introduces an error in the measured speed that depends on the lens shape and the distance of the window from the lens center. For the Borja, et al., (2009b) model, refraction introduces an error ranging from -0.09% to -0.38%, at a point on the lens profile, 3mm away from the center of the lens along the equatorial axis, when the window is 2 mm to 10 mm away from the equatorial plane of the lens. As the anterior thickness of the lens varies from 1.74 to 2.05 mm, for the age range of 20 to 80 years, (Rosen, et al., 2006) the window was chosen to be placed at approximately 4mm away from the lens equator, for the speed of sound measurement across the profile of the lens. At this distance the error in speed of sound was -0.16% at a point 3mm away from the center of the lens along the equatorial profile.

These simulations show that refraction has a negligible effect on the measurement of speed of sound using the TOF technique.
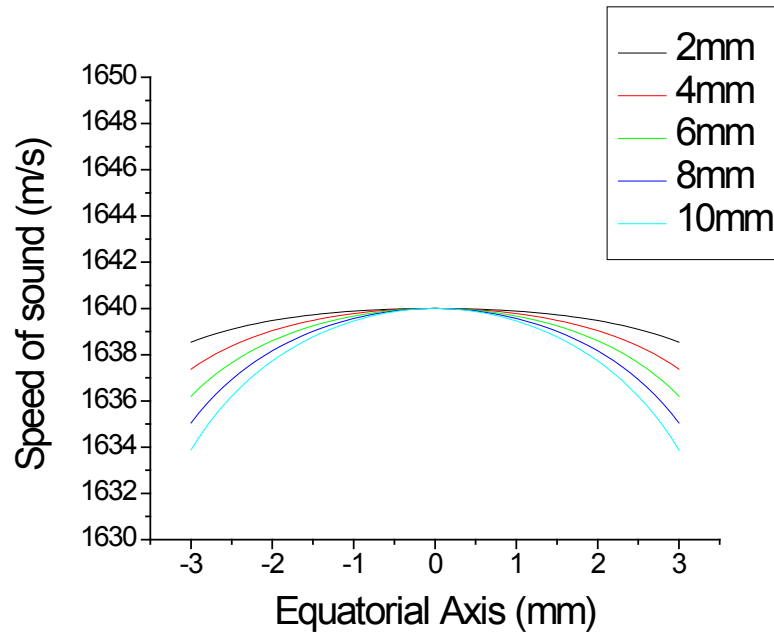
Figure 4.10: Effect of refraction on speed of sound measurement along the central 6 mm profile of the lens. If the lens is assumed to have a uniform speed of sound, refraction introduces an error that is dependent on the lens shape and the distance of the window from the lens equator. For the Borja, et al., (2009b) model, the error at the lens profile 3mm away from the center of the lens along the equatorial axis varies from -0.09% to -0.38% for window placement of 2 mm to 10 mm away from the lens equator. These values are within the experimental variability.

4.6 Results

4.6.1 Speed of Sound in Water and DMEM

Time of flight was measured in distilled water and DMEM to a window from a known distance which was chosen as the reference position. The transducer was moved 0.5 mm away from the window and time was measured again. The process was repeated for 10 measurements. Time of flight was computed using Equation 4.17. The inherent error in determining the number of samples was ± 3 samples, which corresponds to an

error of ± 18.75 ns in determining time of flight. This variability would introduce a 1.2% error in the speed of sound calculation. Time of flight versus distance was plotted for water (Figure 4.11 (a)) and DMEM (Figure 4.11(b)) as obtained from the 35MHz and 50 MHz transducers. Linear regression of time of flight versus distance was performed for the two datasets.

The slopes obtained for water were 6.57E-4 (±2.44E-6) s/m and 6.56E-4 (± 2.53E-6) s/m respectively. The inverse of the slopes yielded the speeds of sound with the two transducers, which were 1523.02 (±5.7) m/s and 1524.78 (±2.5) m/s respectively. Speed of sound measured in distilled water is comparable to accepted value of 1524 m/s at 37ºC (Willard, 1947).

The slopes obtained for DMEM were 6.46E-4 (± 2.43E-6) s/m and 6.45E-4 (± 2.23E-6) s/m respectively. The inverse of the slopes yielded the speeds of sound with the two transducers, which were 1547.6 (± 5.8) m/s and 1548.21 (± 5.3) m/s respectively. For calculation of speed of sound in the lens a value of 1548 m/s was used for the speed of sound in DMEM for both transducers. A precision of ± 6 m/s introduces a ± 0.38% error. For a 5 mm thick sample this corresponds to an error of ± 19.4 µm in thickness measurements.
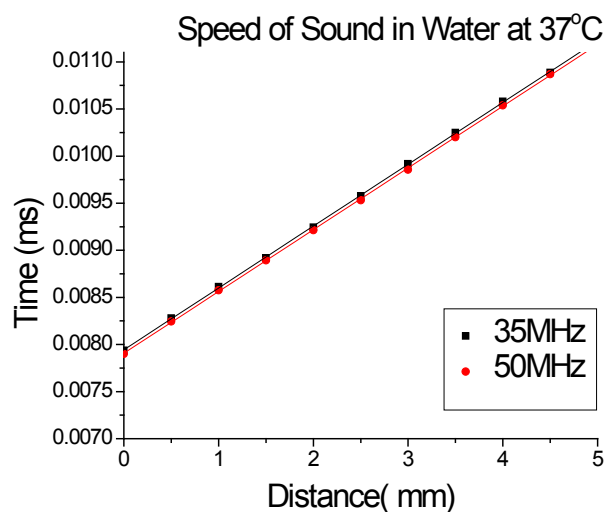
(a)
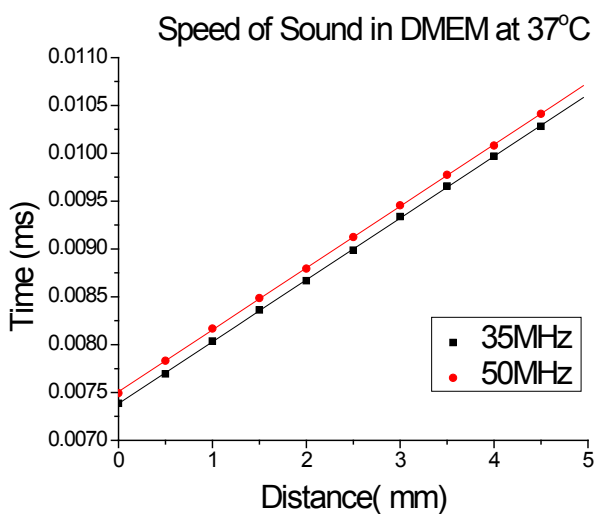
(b)

Figure 4.11: Time of flight from window to transducer at various distances, in (a) water and (b) DMEM, at 37°C with 35 MHz and 50 MHz transducers. The inverse of the slope yields the speed of sound. The speed of sound in water is 1523.02 (±5.7) m/s with the 35 MHz transducer and 1524.78 (±2.5) m/s with the 50 MHz transducer. The speed of sound in DMEM is 1547.6 (±5.8) m/s with the 35 MHz transducer and 1548.21 (±5.3) m/s with the 50 MHz transducer.

4.6.2 Speed of Sound in the Lens

Speed of sound was measured in 6 human crystalline lenses from 5 human donors with both the 35 MHz and 50 MHz transducers. Details of the lenses including, age, cause of death and postmortem time are provided in Table 4.4. Lenses were examined using a shadow-photogrammetric system and those that were swollen or exhibited capsular separation are indicated by the blue italicized font. The postmortem time ranged from 1 to 5 days, and the age ranged from 28 to 67 years.

Speed of sound was measured 3 times in the un-stretched state and in the 2 mm stretched state across the whole lens profile. The average measurement of speed of sound at the center of the lens is shown in Table 4.5. The variability of repeated measurements of the same lens (standard deviation divided by average) ranged from 0.1-0.85%. A Student's t-test revealed that speeds of sound measured by the two transducers (p=0.54) and measured at the un-stretched and stretched states (p=0.97 for the 35 MHz transducer and p=0.77 for the 50 MHz transducer) were not significantly different.

Speed of sound along the equatorial profile as obtained from the 35 MHz transducer was plotted for lenses that were not swollen. All three measurements (red, green and black) per lens for the two states and the average profile (blue) are shown in Figure 4.12. The average profile was compared across ages and stretch states.

Eye	Age	PMT (Days)	Cause of Death	Wet weight (mg)
H1 OD	28	3	Sepsis	175
H1 OS	*28*	*5*	*Sepsis*	*224*
H2 OD	*60*	*4*	*Cirrhosis*	*306*
H3 OD	67	1	--	257
H4 OD	52	4	Colon cancer	299
H5 OD	*56*	*3*	*Renal failure*	*302*

Table 4.4: Summary of age, postmortem time, cause of death and wet weight of the human crystalline lenses used in the speed of sound measurement experiments. Swollen lenses are indicated by the blue italicized font

Eye	Un-stretched		2 mm of Stretch	
	Speed of sound (m/s) 35 MHz	Speed of sound (m/s) 50 MHz	Speed of sound (m/s) 35 MHz	Speed of sound (m/s) 50 MHz
H1 OD	1687.67 ± 10.27	1706.17 ± 1.91	1692.69 ± 6.61	1715.47 ± 6.5
H1 OS	*1622.31 ± 6.48*	*1659.89 ± 3.46*	*1662.96 ± 2.32*	*1665.63 ± 2.32*
H2 OD	*1676.23 ± 3.52*	*1711.97 ± 0.51*	*1682.53 ± 2.1*	*1692 ± 6.57*
H3 OD	1686.69 ± 7.34	1691.72 ± 7.44	1675.51 ± 7.35	1671.18 ± 2.16
H4 OD	1680.38 ± 7.31	1662.67 ± 6.21	1655.89 ± 5.58	1659.43 ± 7.56
H5 OD	*1675.81 ± 7.45*	*1652.65 ± 7.24*	*1661.88 ± 2.03*	*1656.16 ± 5.85*
Mean (N=6)	**1671.52 ± 24.63**	**1680.85 ± 25.66**	**1671.91 ± 14.12**	**1676.65 ± 22.85**
Mean (N=3) *Lenses that were not swollen*	**1684.91 ± 3.96**	**1686.85 ± 22.15**	**1674.7 ± 18.42**	**1682.03 ± 29.55**

Table 4.5: Speed of sound measured at the center of the lens in human crystalline lenses. Swollen lenses are indicated by the blue italicized font.
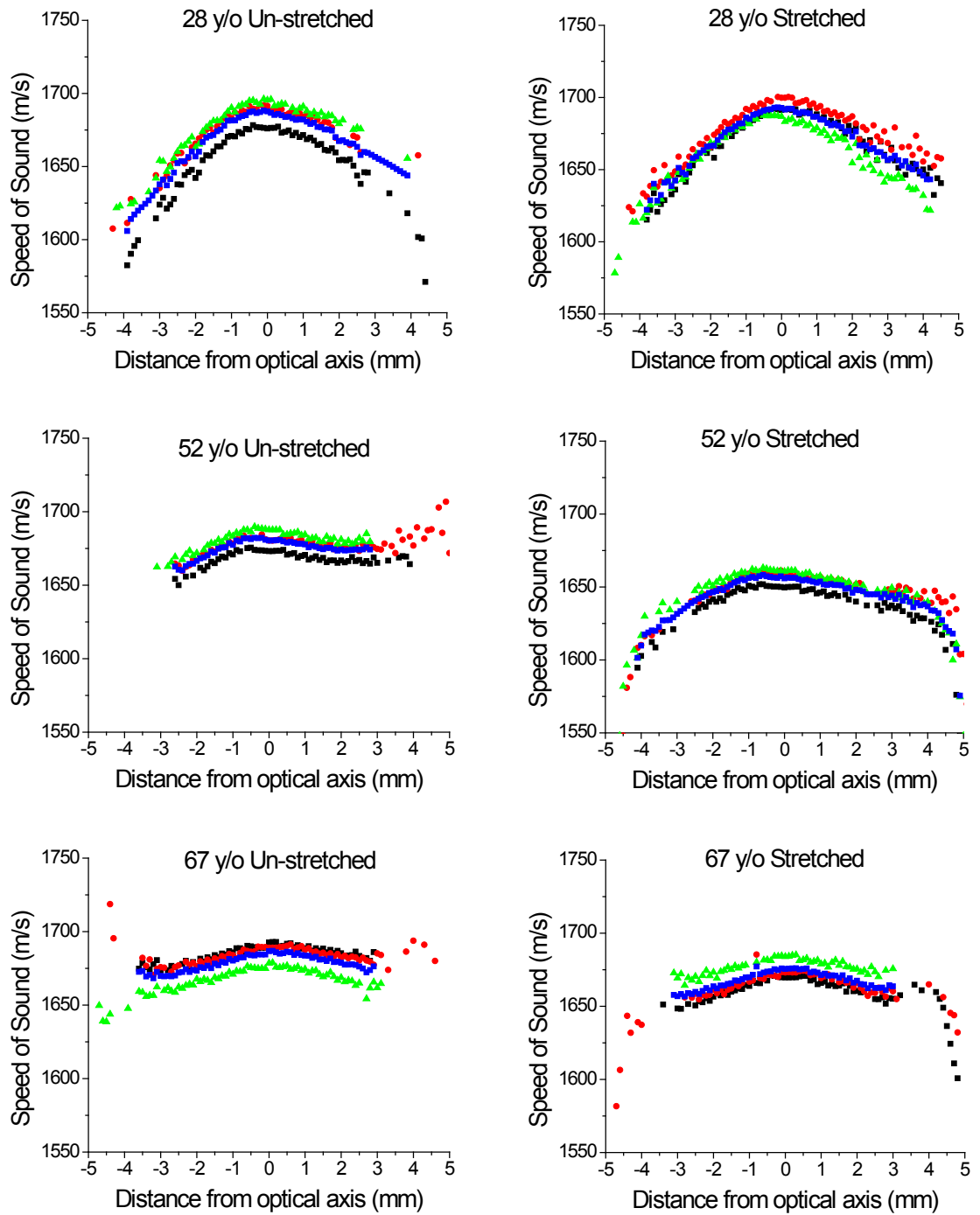
Figure 4.12: Speed of sound measured across the equatorial profile in the 2-mm stretched and un-stretched states of lenses that were not swollen. 3 measurements (red, green and black) were made per state per lens. The average measurement is shown in blue.
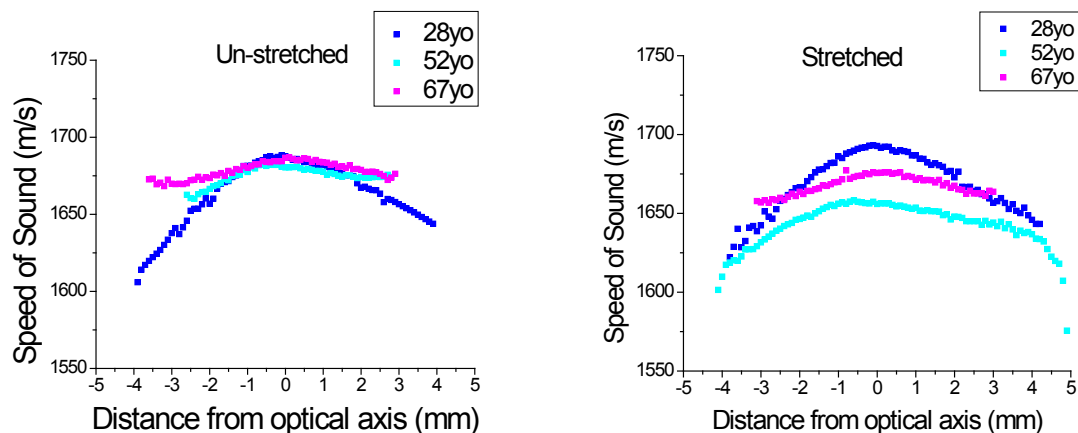
Figure 4.13: Average speed of sound along the equatorial axis of (left) un-stretched and (right) stretched lenses aged 28, 52 and 67 years as measured by the 35 MHz transducer.

Average speed of sound across the equatorial profile for lenses of different ages are shown Figure 4.13 in the un-stretched (left) and stretched (right) states. There was more variation in the young lens in the central 6 mm of the lens compared to the older lens, in both states.

Figure 4.14 shows the average equatorial profiles for the un-stretched and stretched states of these same lenses. The speed of sound in the stretched lens was slightly higher than that in the un-stretched lens for the 28 year old and the speed of sound in the un-stretched lens was higher in the older lenses. However, these values are within the measurement error for the 28 year old and the 67 year old lens.
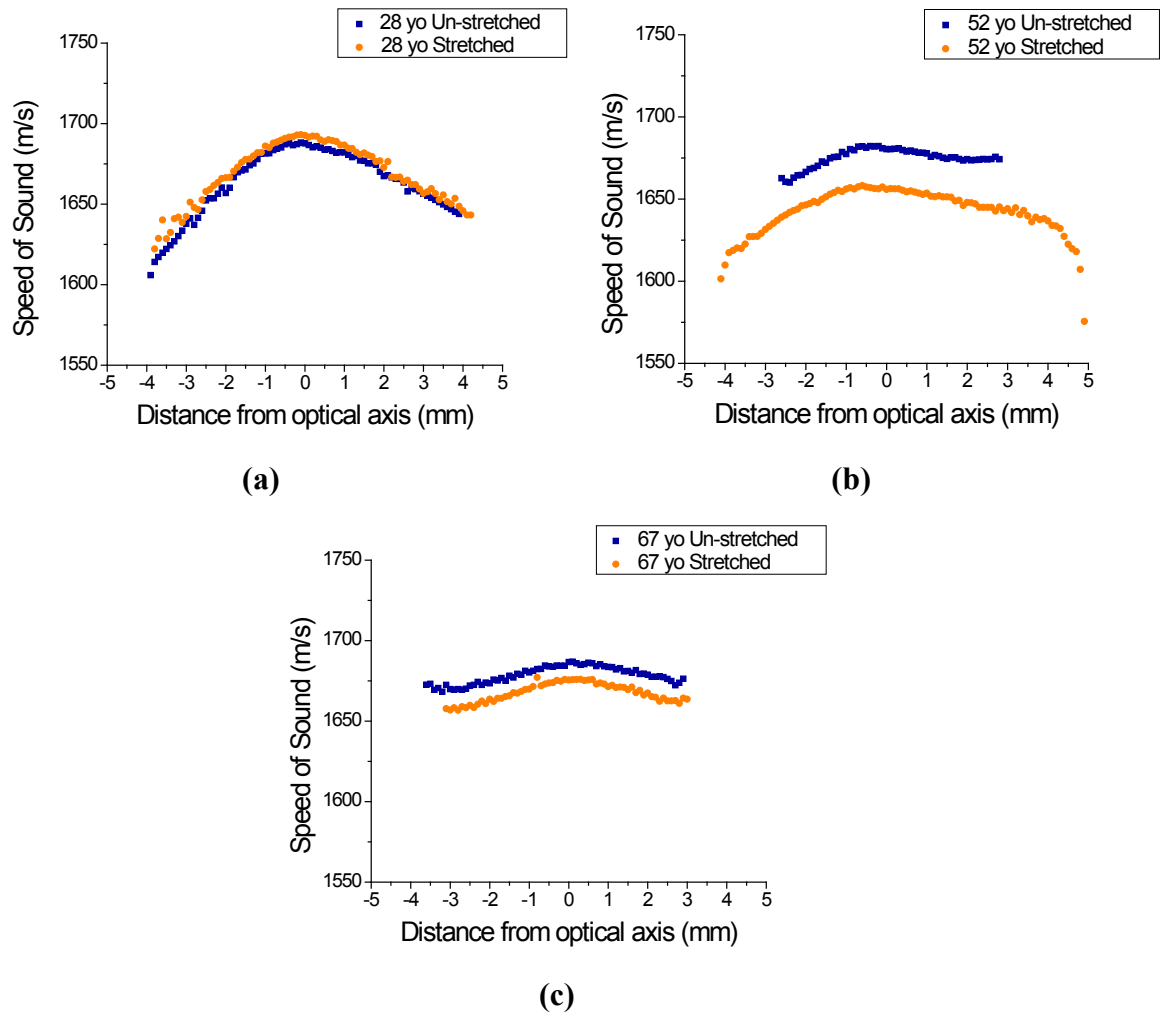
Figure 4.14: Average speed of sound profiles in the equatorial plane in the un-stretched and 2 mm stretched states of lenses aged (a) 28 (b) 52 and (c) 67 years.
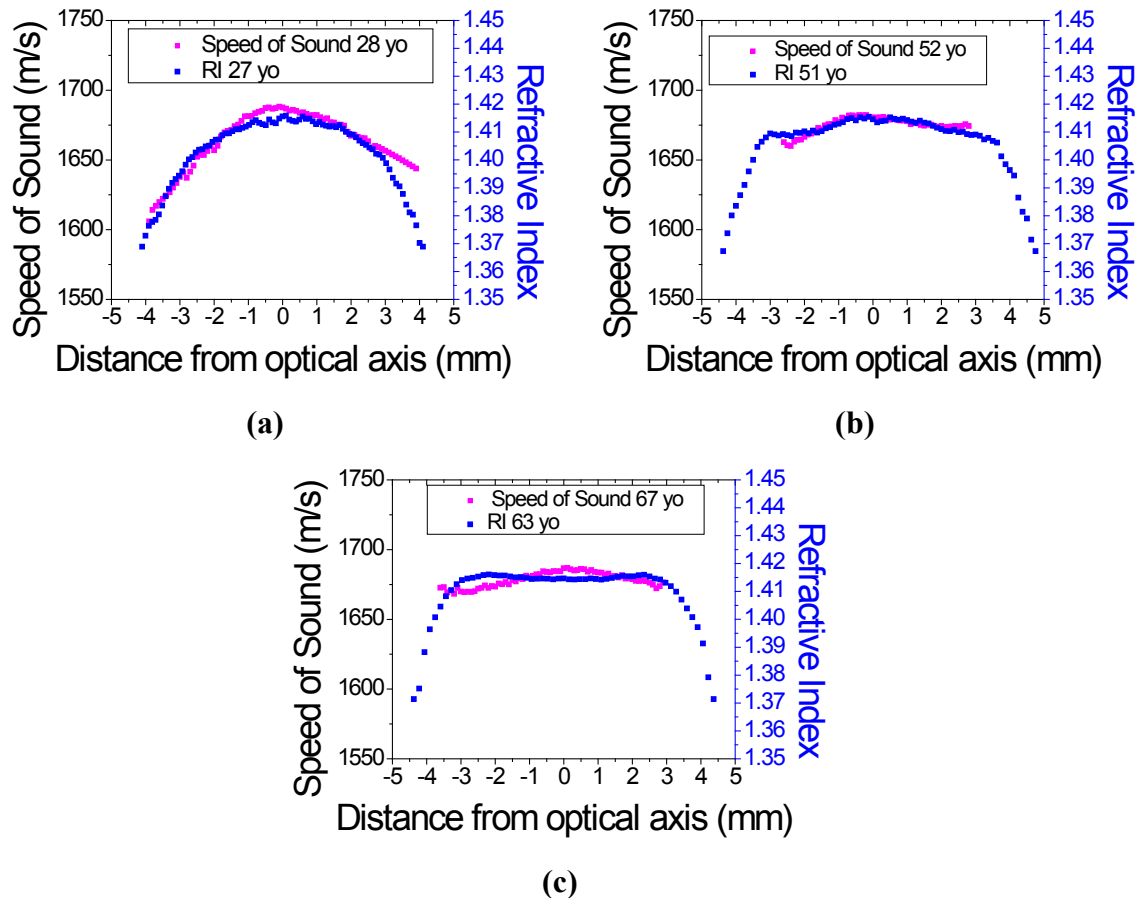
Figure 4.15: Average speed of sound across the equatorial profile is compared to refractive index at the equator (Jones et al., 2005).

Speed of sound measured across the equatorial profile was compared to Refractive index measurements at the equator (Jones, et al., 2005). Figure 4.15 shows that these parameters display similar trends.

Goss, et al.,'s (1980) empirical model was applied to the measured speed of sound to predict protein concentration percentages (Figure 4.16). The values calculated (50%) were higher than reported values (33%).
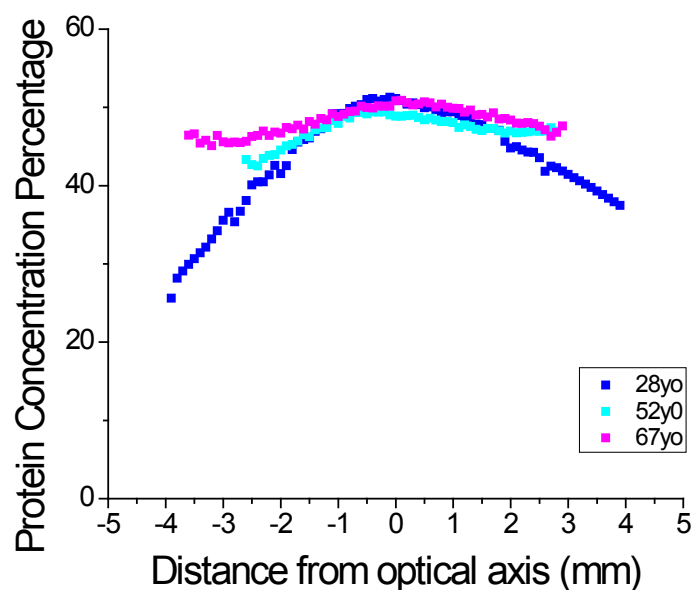
Figure 4.16: Protein concentration percentage of the lens across the equatorial profile was calculated from average speed of sound using Goss, et al.,'s (1980) empirical model.

4.7 Discussion and Conclusion

In this chapter the speed of sound was measured in human crystalline lenses. Speed was measured at the center and across the equatorial profile, when the lens was un-stretched and when stretched by 2 mm radially. Speed was measured with both the 35 MHz and 50 MHz transducers. The average value measured by the two transducers at the center of the un-stretched lens was 1685 m/s and 1687 m/s respectively for lenses that were not swollen. These values are 45-47 m/s (<3%) larger than reported values. These higher values could be due to better hydration control of the lens by using DMEM as immersion medium and not water or saline solution.

Speed of sound across the equatorial profile showed higher variation in the younger lens than in the older lenses. For the younger lens the speed profile was slightly

elevated when the lens was stretched and for the older lenses the speed profile was higher in the un-stretched state. However, these values were within the measurement error for the 28 year old and the 67 year old lens.

Average speed profile variation across the equatorial profile, with age, was similar to refractive index profile variation at the equator (Jones, et al 2005). Refractive index of protein solutions have been shown to be linearly related to the protein concentration (Barer and Joseph, 1954). Refractive index of constituent proteins of the lens were measured in the bovine lens and successfully applied to predict the refractive index gradient in the rat lens thereby demonstrating the relationship between refractive index and protein concentration of the lens (Pierscionek, et al., 1987). Based on Figure 4.15, it can be concluded that speed of sound in the lens is dependent on the protein distribution in the lens.

Protein concentration percentage across the equatorial profile was estimated with average speed measurements, using Goss, et al.,'s (1980) empirical model. The central concentration was much higher (50%) than reported values (33%). When the constant in Goss, et al.,'s empirical model was changed from 3.2 to 4.2, the values were comparable. Goss, et al.,'s empirical model was developed for speed measurements at 27°C. This constant has been shown to have a value of 3.8 for hemoglobin at 25°C (Carstensen and Schwan, 1959). To apply this empirical model to crystalline lenses, the constant has to be re-evaluated by measuring speed of sound in lens protein solutions.

The protein concentration gradient in the lens is generated through lens compaction (Augusteyn, 2008). During lens growth, fibre cells lose water gradually as

they are packed into the centre of the cell, such that, deeper the cell, the lesser the water content. Results from speed measurements are consistent with lens compaction and with the formation of a nuclear plateau.

In summary, speed of sound in the lens is dependent on protein concentration. The younger lens show greater variation of speed of sound across the equatorial profile than the older lenses. In the next chapter, the central speed measurements will be used to reconstruct lens shape from UBM images.

CHAPTER 5. MEASUREMENT OF LENS SHAPE USING ULTRASOUND

5.1 Overview

UBM images of the lens will be acquired with the lens mounted in a Manual Lens Stretcher (MLS). To obtain undistorted dimensions and shape of the whole ex vivo lens, a shadow-photogrammetric system will be developed. A mathematical model will be developed to quantify the lens shape. Lens shape extracted from UBM images will be compared to that obtained from shadow-photogrammetric images to establish if UBM can be used for whole lens biometry. The advantages of measuring lens dimensions with the UBM are that UBM images can be acquired faster than OCT images and both the lens and the ciliary body can be imaged at the same time.

5.2 Shadow-photogrammetry

5.2.1 Background

Previously, a shadow-photogrammetric system was developed in house at the Ophthalmic Biophysics Center at the Bascom Palmer Eye Institute (Denham et al., 1989). The main component of this system is a commercially available optical comparator (Model BP305, Topcon Ltd., Tokyo, Japan) which projects a 20× magnified shadow of an object onto a viewing screen. The image of the viewing screen is captured by a digital camera (Figure 5.1 (a)). This system was used to evaluate corneal buttons (Denham et al., 1989; Pflugfelder et al., 1992). This system was later modified to utilize two light sources to enable photography of the coronal and sagittal planes of isolated crystalline

lenses (Rosen et al., 2006). Figure 5.1 (b) and (c) show sagittal and coronal images, of a 37 year old human lens, obtained from this system. Sagittal images of ex vivo lenses were captured to measure dimensions and curvatures (Rosen et al., 2006) and whole lens shape (Urs et al., 2009) of the isolated lens. The main drawbacks of this system are that it acquires images of projected views and that it is very bulky. Hence a new smaller system, which is optimized for the crystalline lens was developed.

(a)   (b)

(c)
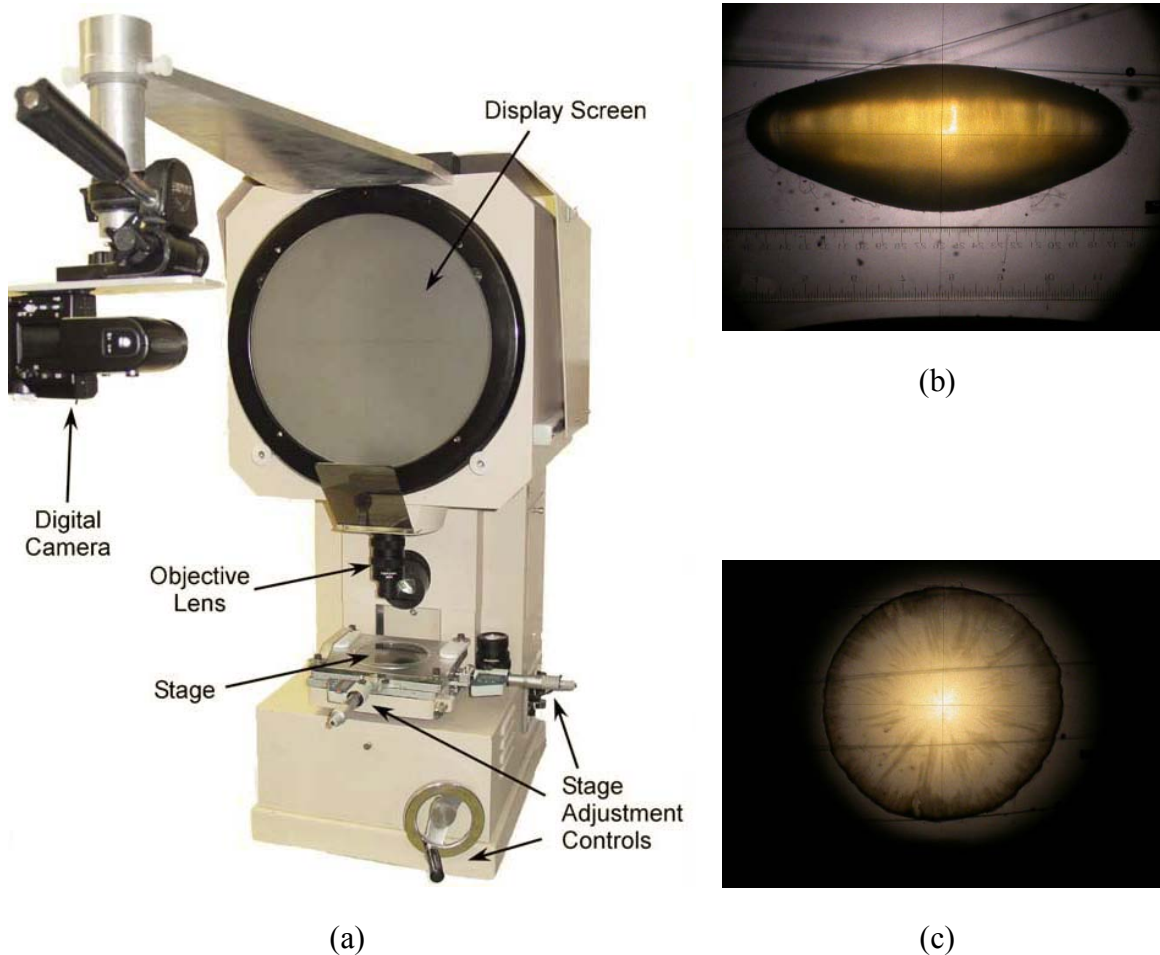
Figure 5.1: (a) The Topcon Optical comparator was modified for photographing lens profiles with a digital camera mounted on an aluminum arm. (Rosen, et al., 2006). (b) Sagittal and (c) Coronal images of a 37 year old human lens that was 2 days postmortem.

5.2.2 Design

The optical and mechanical designs of the shadow-photogrammetric system are shown in Figure 5.2 (a) and (b) respectively. The system consists of three main parts:

- An illumination system that illuminates the lens with a collimated beam from the side for a sagittal view and from below for a coronal view. The illumination system uses two white Light Emitting Diodes (LED) and collimating lenses.

- An imaging system that creates an image of the equatorial (coronal view) or axial (sagittal view) plane on the imaging sensor of a digital camera using an objective lens.

- A tissue housing component and positioning system to hold the crystalline lens and allow fine centering and rotational and tilt adjustment.

The illumination system consists of two 3 mm diameter, epoxy-encased white LEDs and collimating lenses to produce telecentric illumination. An aperture is placed in front of the LED to minimize the divergence of the beam. The aperture of the adjustable diaphragm acts as the effective source of light. The LEDs were collimated using a 25 mm diameter achromat of 150 mm focal length. The full divergence angle, θ, of the beam after collimation is given by the following formula:

$$\theta = \frac{D_s}{f_c}$$

<div align="right">Equation 5.1</div>

where D_s is the diameter of the aperture and f_c is the focal length of the collimating objective. The full divergence angle of the beam was calculated to be 0.16 radians for an

aperture size of 25 mm. The system employs three mirrors to fold the light path to illuminate the crystalline lens from below and from the side for coronal and sagittal profile imaging respectively.
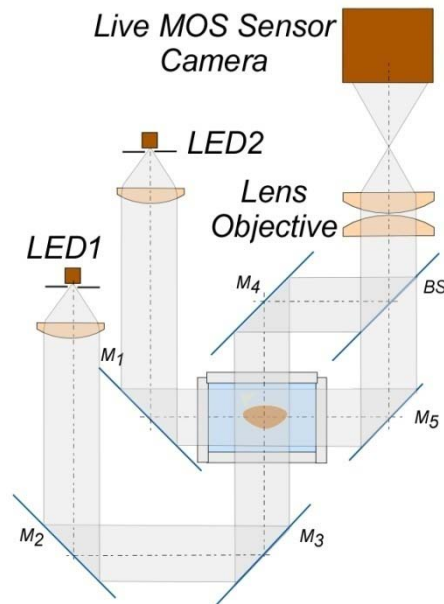
(a)
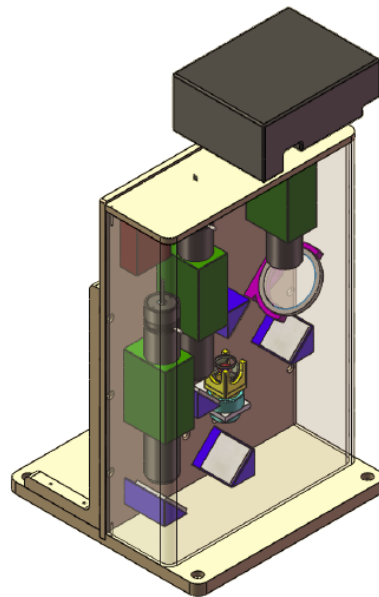
(b)

Figure 5.2: (a) General design principle of the shadow-photogrammetric system. (b) Mechanical design of the shadow-photogrammetric system.

The imaging system consists of an imaging lens pair, a pair of mirrors and a beam splitter to create an image of the coronal or sagittal view on the imaging sensor of a digital camera. An Olympus E-410 10 megapixel camera was chosen to capture the images. This camera was chosen because it has a Live MOS (Metal Oxide Semiconductor) sensor. The sensor size is 17.3 mm X 13 mm and the pixel size is 4.75 μm. The Live MOS sensor consumes lower energy than a CMOS (Complementary MOS) sensor, making it possible to add the 'live view' function. The camera also provides a zoom-in facility. The real time view can be redirected to a computer monitor and the zoom-in facility can be used to bring the object into focus.

The objective lens is composed of two achromats (Figure 5.3). The focal length of the first achromat of the objective lens is also the distance from the crystalline lens plane to the objective. This distance must be large enough to allow mounting of the tissue housing component and folding optics therefore a value of 150 mm was selected. The achromats were selected to provide a field of view of 12.5 x 12.5 mm in the image space, because the minimum dimension of the Live MOS sensor was 13mm. The magnification *M*, is determined by the following equation derived using basic geometrical optics principles:

$$M = \frac{f_2}{f_1} = \frac{I}{FOV}$$
<div align="right">Equation 5.2</div>

where f_1 and f_2 are the focal lengths of the first and second achromat, respectively, *FOV* is the field of view in the object space, and *I* is the size of the image. The largest diameter of a human crystalline lens is less than 11 mm. As the desired field of view in the image space is 12.5 X 12.5 mm, the magnification becomes 1.2.Since focal length f_1 was chosen

to be 150 mm, to achieve a magnification of 1.2, f_2 was calculated to be 180 mm. The lens with the closest focal length available was 175 mm, making the magnification of the system 1.16.

The tissue housing component (Figure 5.4) consists of a transparent spherical cell mounted in a cell holder. The cell is made of clear PMMA and consists of sutures on which the crystalline lens can be placed. Placement of the lens on the sutures allows imaging of both anterior and posterior sections of the crystalline lens in the sagittal view. The cell has openings on the top, bottom and sides to allow light to pass through. The spherical shape of the cell facilitates rotational alignment of the crystalline lens and minimizes effects of tilting in the sagittal and coronal planes. The cell holder has clear plastic windows on the sides and a round glass window on the bottom which permits the lens to be illuminated from both directions. The cell holder is placed on a three dimensional positioning system for precise center alignment.

Object Plane
(Crystalline Lens)

Image Plane
(Live-MOS Sensor)

f_1 f_2
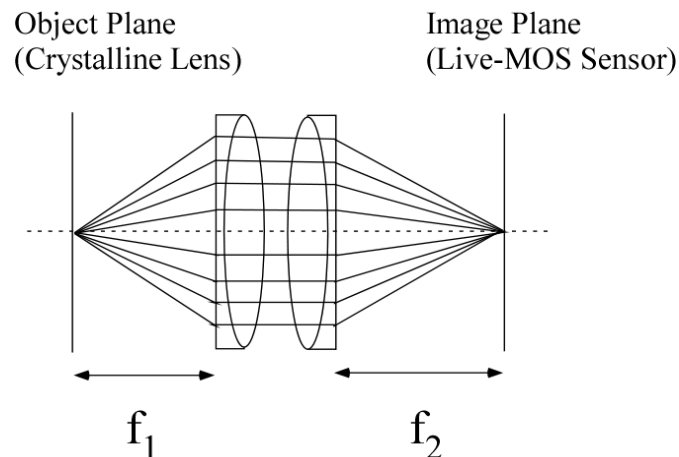
Figure 5.3: The objective lens of the imaging system is composed of two achromats, with focal lengths f_1 = 150 mm and f_2 = 175 mm. The magnification of the system is 1.16.

(a) (b) (c)
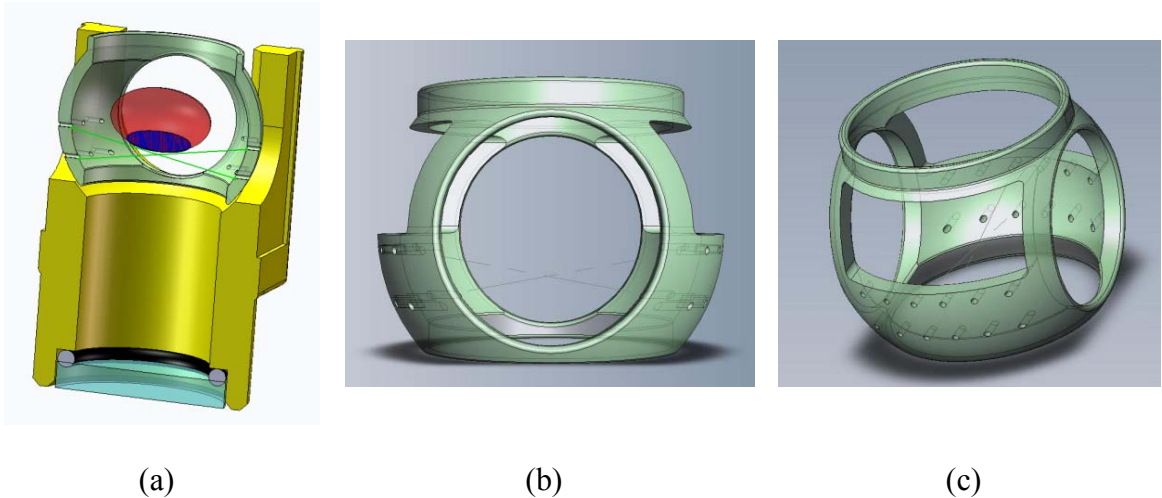
Figure 5.4: (a) Mechanical drawing of the tissue housing component. It consists of a rotatable cell with sutures on which the crystalline lens can be positioned. (b) and (c) Mechanical drawings of the transparent spherical cell.

5.2.3 Calibration

The resolution of the system was determined by capturing images of a resolution target (USAF Resolution Target 2" Square Positive – part # NT38-257 – Edmund Optics USA). The group with the highest frequency that was visible was Group 5 - Element 6 (Figure 5.5) which corresponds to 57 line-pairs/mm or 8.77 µm/line. Since the magnification of the system is 1.16, the resolution of the system is 7.5 µm in the plane of the crystalline lens.

(a)   (b)
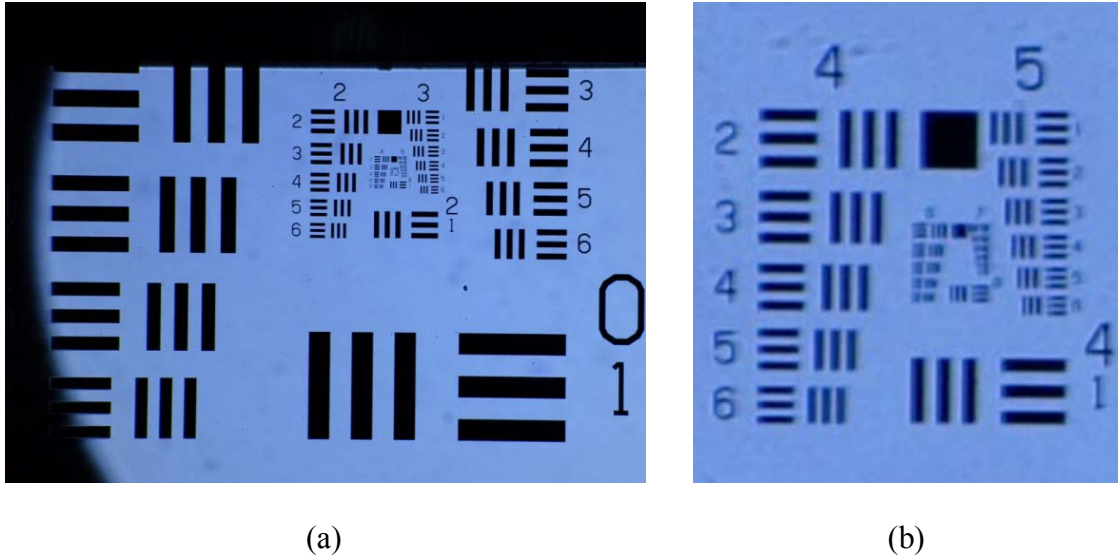
Figure 5.5: (a) Shadow-photogrammetric image of the resolution target (USAF Resolution Target 2" Square Positive – part # NT38-257 – Edmund Optics USA). (b) Enlarged view of the central section. The group with the highest frequency that was visible was Group 5 - Element 6 which corresponds to 57 line-pairs/mm or 8.77 µm/line. The magnification of the system is 1.16. Therefore the resolution of the system is 7.5 µm in the plane of the crystalline lens.

The actual pixel size of the sensor is 4.75 µm. As the magnification of the system is 1.16 each pixel represents 4.07 µm in the plane of the crystalline lens. To measure the actual pixel size, a fixed frequency grid distortion target (25X25 DOT GRID GLASS 0.25MM CENTERS – part # NT58-257 – Edmund Optics USA) was imaged using the system. The target is composed of 0.125 mm diameter dots. The average diameter of the dots was measured as 31 pixels using the image processing software ImageJ (Rasband, 1997-2008; Abramoff, et al., 2004). Each pixel therefore corresponds to 4.03 µm. This difference of 0.04 µm between the measured pixel size and the expected size is negligible.

5.2.4 Lens Imaging and Contour Detection

During lens imaging, the spherical cell was placed in the cell holder and the cell holder was filled with the preservation medium DMEM (Dulbecco's Modified Eagle Medium). The isolated crystalline lens was delicately placed on the sutures of the cell using a lens spoon (K3-4255, Katena Products Inc, Denville, New Jersey). The cell was rotated for alignment of the lens. The camera was set to the 'live-view' mode and the image was zoomed-in 10 times and displayed on a monitor. The crystalline lens was brought into focus by adjusting the three dimensional positioning system. The light source was switched to obtain images of both the sagittal and coronal profiles of the crystalline lens. Figure 5.6 shows sagittal and coronal images of a 28 year old human lens that was 3 days postmortem.

Contour detection was performed with MATLAB. Lens images were converted to 8-bit grayscale images. An algorithm composed of two separate processes was used to detect the lens-contour. The first process detected a thick approximate contour of the lens, using the Prewitt edge detector and morphological functions. This eliminated false edges generated by the sutures, zonules, adherent vitreous and other material extraneous to the lens. The second separate process used the Canny edge detector, to detect a fine contour of the lens. An intersection of the outputs of the two processes produces the lens contour with minimal false contours. A few false contours that were detected were removed manually. Figure 5.7 shows the manually cleaned lens contour superimposed on the shadow-photogrammetric image of the lens shown in Figure 5.6 (a).
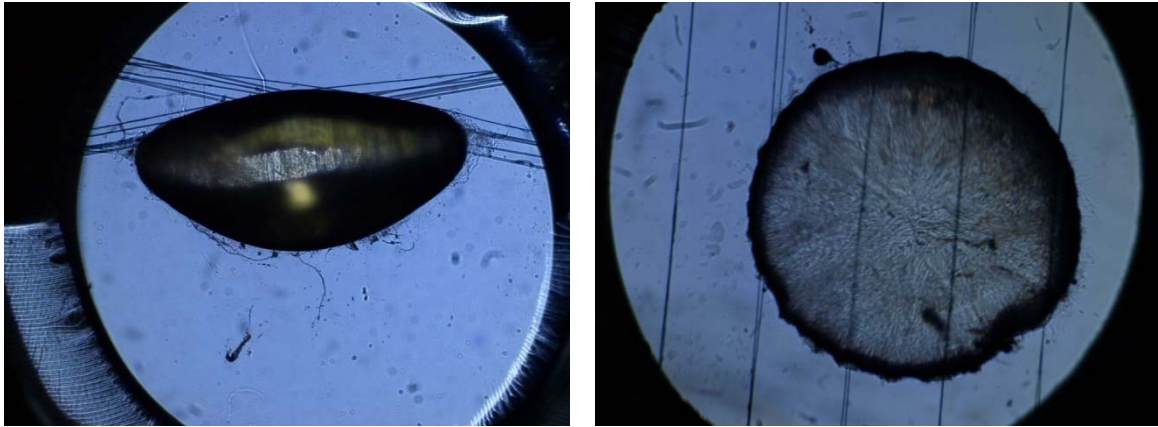
(a)   (b)

Figure 5.6: (a) Sagittal and (b) Coronal shadow-photogrammetric images of a 28 year old human crystalline lens that was 3 days postmortem.
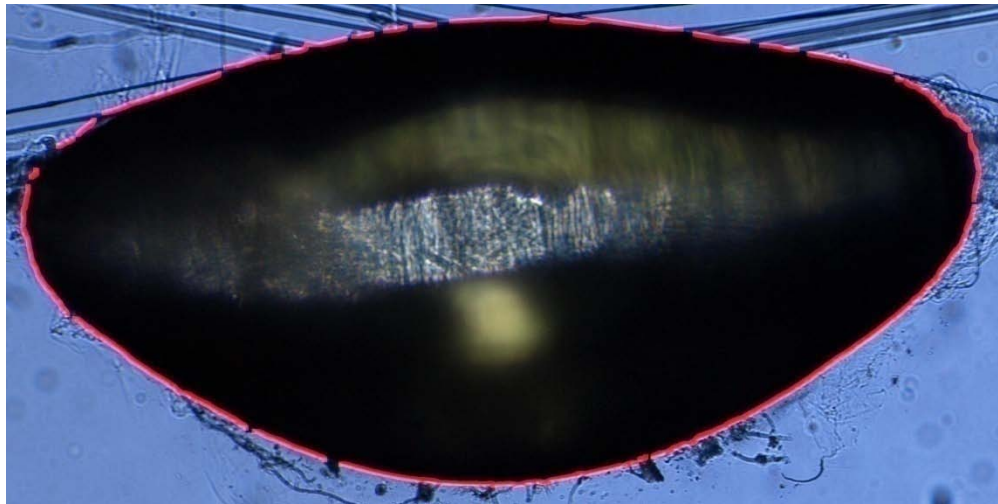
Figure 5.7: The detected contour was superimposed on the image. Gaps in the contour are regions where the algorithm could not detect the lens boundary.

5.3 Ultrasound Imaging of the Lens

5.3.1 Image Acquisition and Construction

The experimental set up described in section 4.4 was used to record the shape of the crystalline lens. The shape was recorded in the un-stretched position, with a B-scan probe. The B-scan probe employed a sector scan pattern to obtain 253 A-lines over a 30º scan sector. Each A-line was composed of 1820 points. Sector reconstruction was performed in MATLAB on the 8 bit raw data to convert it into a rectangular grid. Figure 5.8 shows raw and sector reconstructed images of a 28 year old human lens. The speed of sound measured at the center of the lens and recorded in Table 4.5 was used to perform the reconstruction. The image of the lens was obtained with the posterior surface facing upwards.

(a)   (b)
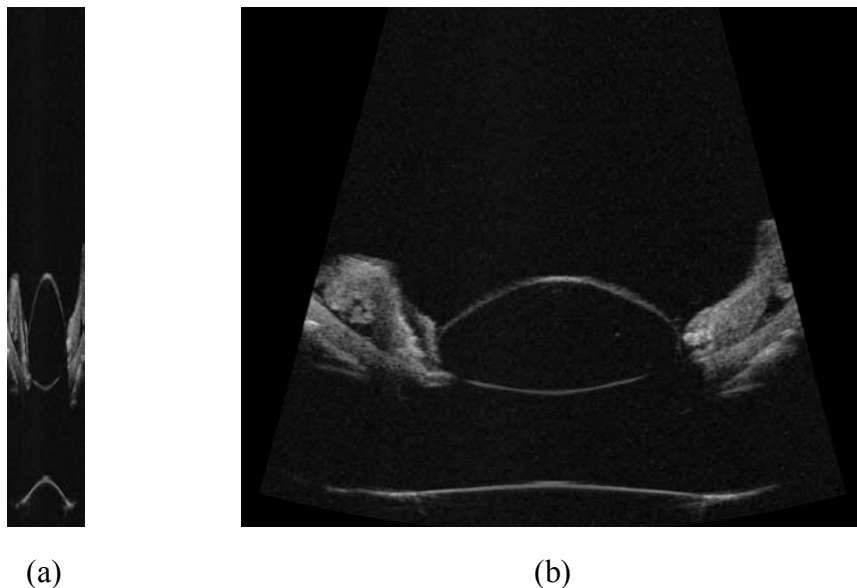
Figure 5.8: (a) 8 bit raw data obtained from Sonomed B-Scan system with the 35 MHz transducer. (b) Sector reconstruction of the raw data. Figure shows images of a 28 year old human crystalline lens that was 3 days postmortem. A glass window was imaged under the lens. This window appears curved due to the difference in speed of sound in the lens and in DMEM

5.3.2 Lens Contour Detection

(a)   (b)

(c)   (d)

(e)
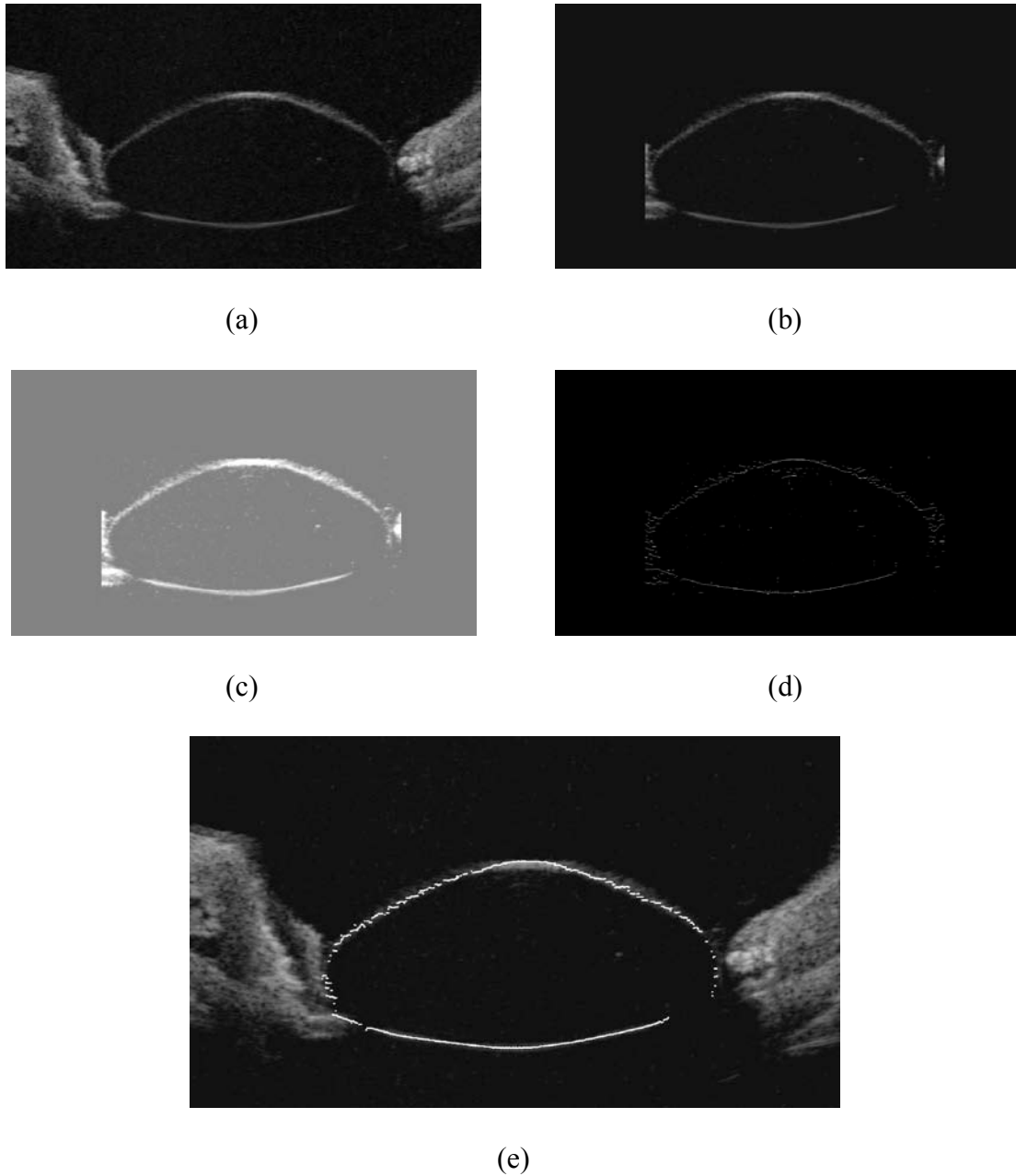
Figure 5.9: Lens contour detection from UBM images of a 28 year old human crystalline lens that was 3 days postmortem (a) Original UBM image after sector reconstruction (b) User input is used to mask regions that are not of interest. (c) Image intensity and contrast are adjusted. (d) Edges are determined using peak detection. (e) Pixels that do not correspond to the lens contour are manually eliminated. Figure shows edge superimposed on original image.

Lens contour detection from UBM images was performed by a semi automated interactive algorithm, using MATLAB. Figure 5.9 illustrates the different stages of the lens contour detection algorithm. Images are of a 28 year old human lens. Figure 5.9 (a) shows a UBM image of a lens after sector reconstruction. User input was used to determine regions around the lens, which were masked by the algorithm (Figure 5.9 (b)). The intensity level and contrast of the image were adjusted (Figure 5.9 (c)) and the lens contour was detected using a peak detection algorithm (Figure 5.9 (d)). Some pixels that do not correspond to the lens contour were also detected. These pixels were manually removed using imaging software. Figure 5.9 (e) shows the manually cleaned lens contour superimposed on the original UBM image.

5.3.3 Effect of Refraction on Lens Shape

The effect of refraction on the shape of the anterior surface was simulated for the central 6 mm of the lens. The simulation was performed with MATLAB. The following geometry was assumed for the sector-scan beam: The distance from the pivot to the transducer face was 20.7792 mm. The face of the transducer was assumed to be 10 mm away from the center of the lens. At this distance an 11 degree scan sector covers the central 6 mm of the lens. The two lens surfaces were modeled with conic sections (Borja, et al., 2009b) as described in section 4.5.

The angles of refraction at the posterior surface were computed using Snell's law (Equation 3.5). The speed of sound in DMEM and the lens were assumed to be 1548 and 1640 m/s respectively. The lens was assumed to have a uniform speed of sound.
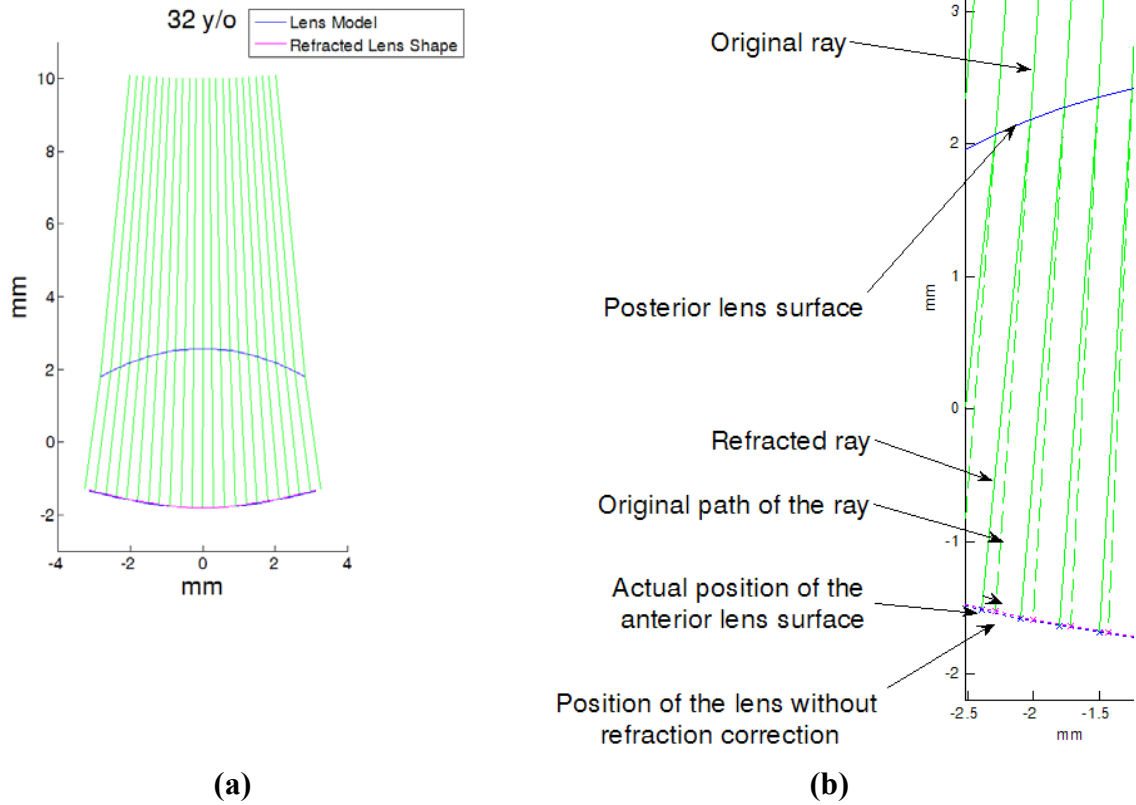
Figure 5.10: (a) Simulation of effect of sound wave refraction on the shape of the anterior surface of a 32 year old lens. (b) The echo from the anterior lens surface (x) is assumed to be arising from a point along the path of the original ray which causes a change in shape of the anterior lens surface (x).

Figure 5.10 shows the simulation of sound wave refraction at the posterior lens surface and the effect of refraction on the anterior lens surface of a 32 y/o lens modeled with the Borja, et al., (2009b) conic lens model. The point of intersection of the refracted ray with the anterior surface was moved to be positioned along the path of the original ray to simulate the output of the UBM (Figure 5.10 (b)).
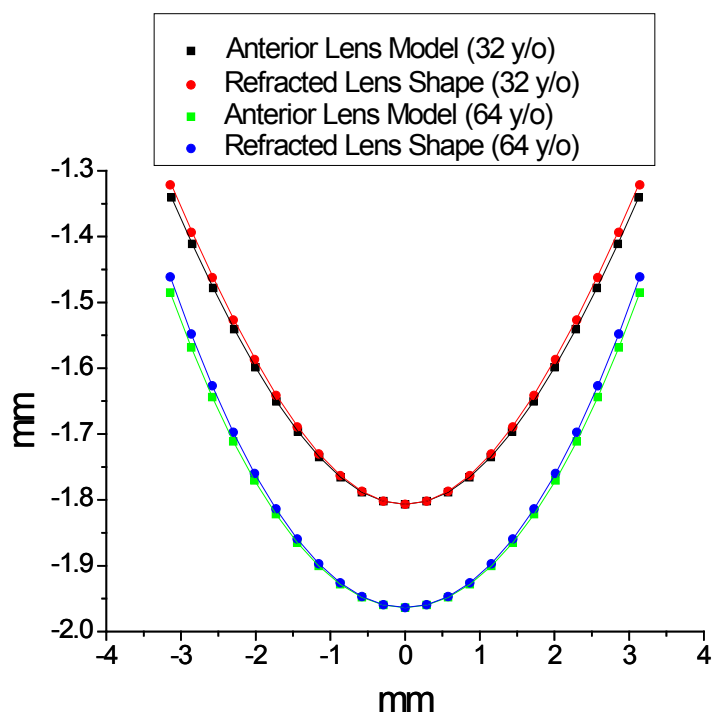
Figure 5.11: Graph shows the Borja et al., age-dependent conic lens model for the anterior surfaces of 32 (black) and 64 (green) y/o lenses and changes due to refraction (32 y/o – red; 62 y/o - blue). Refraction introduced a 6.8% change in curvature for the 32 y/o lens and a 5.5% change for the 64 y/o lens.

The anterior lens model and the anterior lens shape after refraction were plotted for lenses aged 32 and 64 years (Figure 5.11). The anterior radii of curvature with the Borja, et al., (2009b) model were 8.94 mm and 10.63 mm for the two ages. The values decreased to 8.32 mm and 10.04 mm due to the simulated refraction, thereby introducing a 6.9% (0.62 mm) and 5.5% (0.59 mm) error respectively. The percentage error was computed for lenses aged 30 to 85. Error in anterior curvature ranged from 5.25% to 7% in the age range of 30 to 85. The error changes due to change in shape of lens with age. This error is within the variability of measurement as the lateral resolution of the Sonomed UBM is 0.5mm. The simulation demonstrates that the effect of ultrasound

refraction is negligible. In the following work, the anterior surface of the lens obtained from the UBM images will not be corrected for refraction.

5.4   Quantification of Lens Shape

5.4.1   Background

The human lens is most commonly thought of as being composed of two aspherical surfaces, even though the earliest eye models represent the lens as two spherical surfaces. The lens has been modeled with a number of mathematical functions. The shape has been progressively described as hyperbolic (Howcroft and Parker, 1977), parabolic (Koretz, et al., 1984), 4th-order polynomial (Strenk, et al., 2004) and conic (Dubbelman and Van der Heijde, 2001; Manns, et al., 2004b; Rosen, et al., 2006; Borja, et al., 2008). While these models present a good approximation of the human lens, they were developed for optical modeling and therefore mostly focus on the central 4 to 5 mm of the lens, and do not provide information about the far peripheral and equatorial regions. Kasprzak (2000) approximated the whole profile of the human lens using a hyperbolic cosine function. This model is based on published values of radius of curvature and asphericity and focuses on the central optical zone of the lens. This model has been evaluated against hyperbolic, parabolic and elliptic approximations, but has not been compared to the shape of an actual lens and therefore, the validity of the equatorial regions of this model is not known. More recently two polynomials were developed (Urs, et al., 2009). These models did not describe the whole lens shape with one mathematical function. To overcome this shortcoming, a model using cosine functions was developed.

5.4.2 Cosine Model

Lens contour obtained from shadow-photogrammetric images and UBM images were initially centered as follows. The midpoint of the outermost pixels at the equator along the Y axis was estimated to be the position of the optical axis. The position of the equatorial axis was estimated to be the midpoint of the outermost pixels at the equator, along the X axis. The center of the lens was estimated to be the point of intersection of the optical axis and the equatorial axis. This initially centered lens contour was positioned such that the anterior surface of the lens was in the 2nd and 3rd quadrants of the Cartesian co-ordinate system and the posterior surface in the 1st and 4th quadrants (Figure 5.12). This coordinate system was converted to polar domain and fit to a 10th order even Fourier series containing terms for tilt (θ_c) and decentration (x_c, y_c) (Equation 5.3) using MATLAB's least square curve fit method, to correct for decentration and tilts.

$$\rho_c(\theta) = \sum_{n=0}^{10} a_n \cos\left(n \times \left(\tan^{-1}\left(\frac{y - y_c}{x - x_c}\right) - \theta_c\right)\right)$$

Equation 5.3

The center and angle displacements of the lens contour were corrected with the values x_c, y_c and θ_c obtained from the curve fit. Decentration was further corrected in the Cartesian coordinate system by translating the corrected profile to place the equator on *x = 0*, where the equator was defined as the maximum diameter of the lens. The translated, corrected profile was then fit again to a Fourier series model (Equation 5.4) using MATLAB's least square curve fit method to obtain the first 11 Fourier coefficients.

$$\rho(\theta) = \sum_{n=0}^{10} a_n \cos(n\theta)$$

Equation 5.4

This curve fitting is illustrated in Figure 5.13.
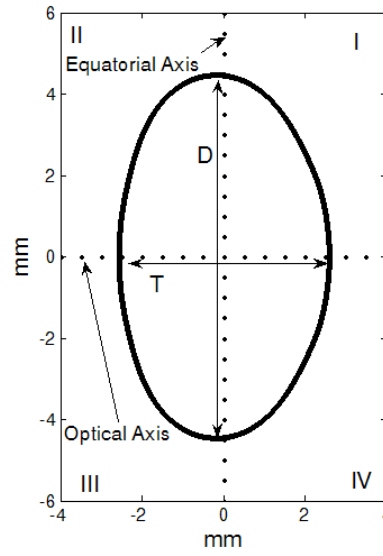
Figure 5.12: The co-ordinate system for the Fourier model. The lens anterior surface was placed in quadrants II and III and the posterior surface was placed in the quadrants I and IV. T and D represent the thickness and Diameter of the lens

The equatorial diameter (D) was estimated as twice the radial distance at $\theta=\pi/2$. The anterior sagittal thickness (bA) and the posterior sagittal thickness (bP) were estimated as the radial distances at $\theta=\pi$ and $\theta=0$ respectively. Total sagittal thickness was estimated as the sum of two thicknesses. The cross-sectional area (CSA) of the lens was computed by integrating the fits in the polar domain (Equation 5.5).

$$CSA = \frac{1}{2} \int_{0}^{2\pi} [\rho_r(\theta)]^2 \, d\theta$$

Equation 5.5

Assuming rotational symmetry, the surface area (SA) of the lens was estimated by computing the surface of revolution of the fitted curve around the optical axis (Equation 5.6).
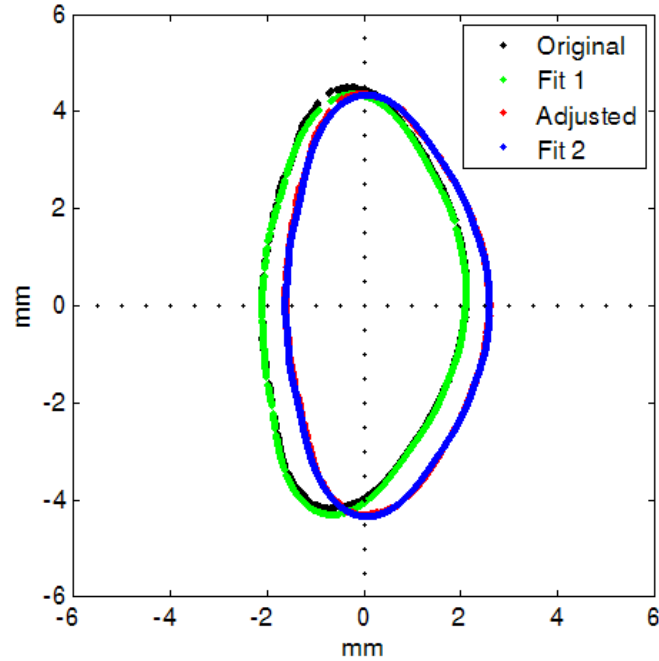
(a)
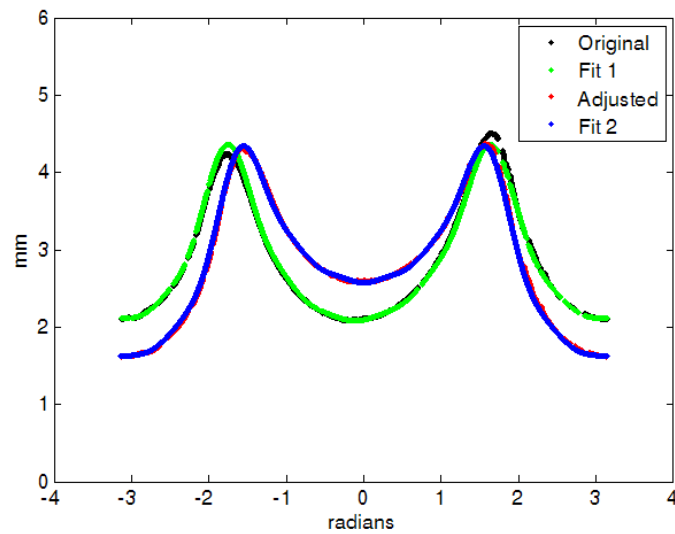
(b)

Figure 5.13: The original lens contour (black), lens contour fit to Equation 5.3 (green), the adjusted lens contour (red) and the lens contour fit to Equation 5.4 (blue). (a) Shows lens contour in Cartesian coordinates and (b) in Polar coordinates for contour extracted from shadow-photogrammetric images of a 28 year old human crystalline lens that was 3 days post mortem.

$$SA = 2\pi \int_0^\pi \rho_r(\theta)\sqrt{[\rho_r(\theta)]^2 + [\rho_r{}'(\theta)]^2} \, \sin\theta \, d\theta \qquad \text{Equation 5.6}$$

The volume (V) of the lens was estimated by computing the solid of revolution of the cross-sectional plane around the optical axis (Equation 5.7).

$$V = \frac{2\pi}{3} \int_0^\pi [\rho_r(\theta)]^3 \sin\theta \, d\theta \qquad \text{Equation 5.7}$$

The cosine model is excellent for lens biometry especially because it provides a method for correction of tilt and decentration. However, it cannot be used to compute radius of curvature, because the higher order terms introduce large variances in curvature values along the surface of the lens. Conic function (described in section 4.5) fits of the untilted and centered lens contour will be used to estimate radius of curvature.

5.5   Application to Human Crystalline Lenses

Lens shape of 6 human crystalline lenses from 5 human donors was measured with the 35 MHz and 50 MHz transducers and with the shadow-photogrammetric system, using the cosine lens model. Details of the lenses used in this study including, age, postmortem time, cause of death and wet weights are provided in Table 5.1. The following parameters were measured and tabulated: Thickness and Diameter (Table 5.2), Cross-Sectional Area and Surface Area (Table 5.3), Volume (Table 5.4), and Anterior and Posterior Radius of Curvature (Table 5.5).

Bland-Altman analysis was performed to assess the degree of similarity between the measurements obtained from the three methods. All measurements were within 2 standard deviations of the mean measurement error. The thickness measurements (Figure

5.14) from all three methods were the same. Although, diameter measurements (Figure 5.15) from UBM 50 images were closer to those from shadow-photogrammetric images than those from UBM 35 images, measurements from all three methods were comparable.

For cross-sectional area (Figure 5.16), measurements from UBM 50 images were slightly lesser than those from shadow images whereas CSA measurements from UBM 35 images were the same as those from shadow images. SA measurements (Figure 5.17) from UBM 35 images were slightly larger compared to those from shadow images, whereas SA measurements from UBM 50 images were the same as those from shadow images. For volume (Figure 5.18), measurements from UBM 35 images were slightly lower than those from shadow images whereas volume measurements from UBM 50 images were slightly higher than those from shadow images.

Radius of curvature measured from UBM images were not similar to the values measured from shadow images. The mean measurement error was 2.72±1.32 mm for the anterior radius of curvature measurements (Figure 5.19) from shadow and UBM 35 images and 2.55±0.66 mm for those from shadow and UBM 50 images. Anterior radius of curvature measurements from UBM images were lower than those from shadow images. For posterior radius of curvature (Figure 5.20), the mean measurement error was -3.07±1.77 mm for measurements from shadow and UBM 35 images and -1.675±1.52 mm for those from shadow and UBM 50 images. These results indicate that posterior radius of curvature measurements from UBM images were higher than those from shadow images.

Eye	Age	PMT (Days)	Cause of Death	Wet weight (mg)
H1 OD	28	3	Sepsis	175
H1 OS	28	5	Sepsis	224
H2 OD	67	4	Cirrhosis	306
H3 OD	60	1	--	257
H4 OD	52	4	Colon cancer	299
H5 OD	56	3	Renal failure	302

Table 5.1: Summary of age, postmortem time, cause of death and wet weight of the human crystalline lenses used in the lens shape measurement experiments.

Eye	Thickness (mm)			Diameter (mm)		
	Shadow images	UBM 35 MHz	UBM 50 MHz	Shadow images	UBM 35 MHz	UBM 50 MHz
H1 OD	4.21	4.23	4.28	8.68	8.98	8.75
H1 OS	4.4	4.24	4.32	8.63	8.76	8.8
H2 OD	5.94	5.83	5.95	9.24	9.54	9.36
H3 OD	4.6	4.62	4.63	9.46	9.68	9.5
H4 OD	4.4	4.57	4.51	9.64	10.2	9.98
H5 OD	4.85	4.96	4.81	9.52	9.68	9.58

Table 5.2: Thickness and Diameter of lenses measured from Shadow-photogrammetric images, and images from UBM 35 MHz and 50 MHz transducers

Eye	Cross Sectional Area (mm^2)			Surface Area (mm^2)		
	Shadow images	UBM 35 MHz	UBM 50 MHz	Shadow images	UBM 35 MHz	UBM 50 MHz
H1 OD	27.14	27.84	27.58	156.5	165.3	159.6
H1 OS	28.86	27.51	27.91	159.4	159.4	160.6
H2 OD	42.17	41.07	39.69	203.3	205.3	195.8
H3 OD	34.02	33.89	33.31	192.7	196	190
H4 OD	32.78	34.31	33.65	193.6	209.2	202.3
H5 OD	35.35	36.02	34.38	195.7	202.2	193.8

Table 5.3: Cross-Sectional Area and Surface Area of lenses measured from Shadow-photogrammetric images, and images from UBM 35 MHz and 50 MHz transducers
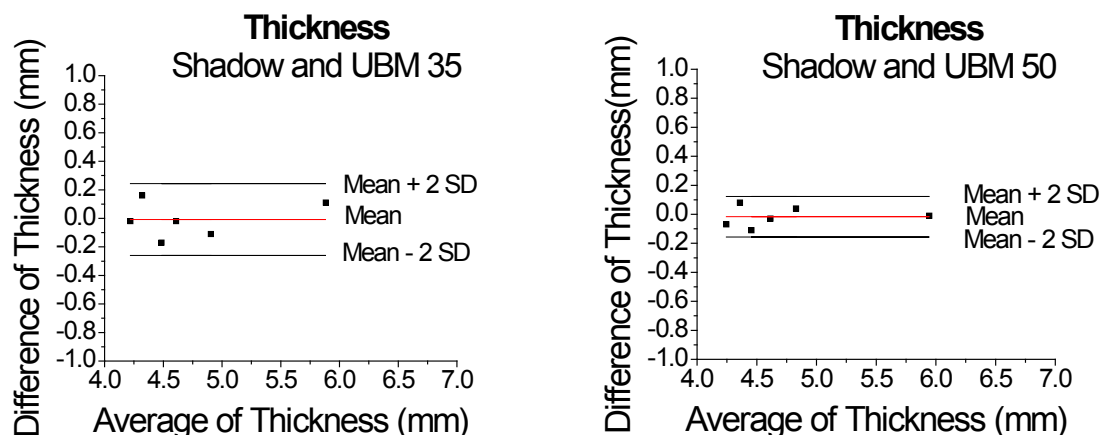
Figure 5.14: Bland-Altman plots for thickness of the lens comparing measurements from (left) shadow-photogrammetric images and UBM 35 images and (right) shadow-photogrammetric images and UBM 50 images of the lens. All measurements were within 2 standard deviations of the mean measurement error. The mean measurement error was -0.008±0.13 mm for the thickness measurements from shadow and UBM 35 images and -0.017±0.07 mm for those from shadow and UBM 50 images. These results indicate that thickness measurements from all three methods are the same.
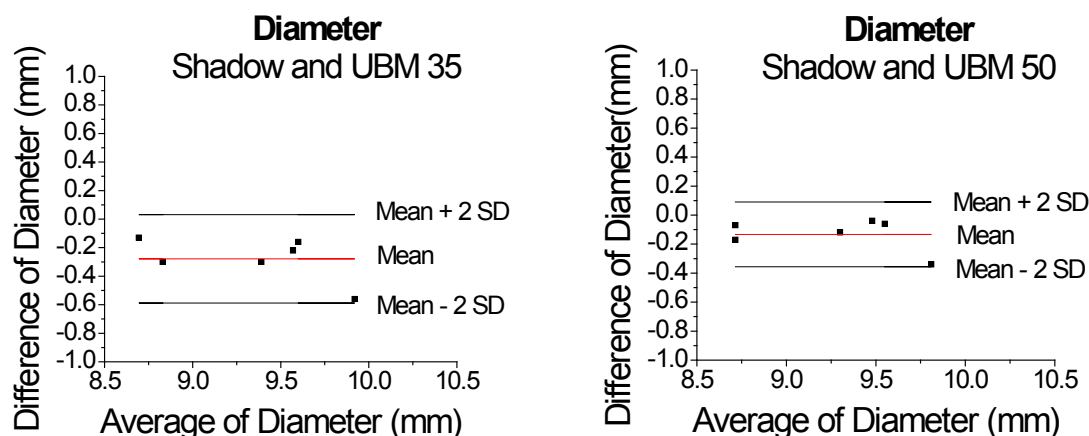
Figure 5.15: Bland-Altman plots for diameter of the lens comparing measurements from (left) shadow-photogrammetric images and UBM 35 images and (right) shadow-photogrammetric images and UBM 50 images of the lens. All measurements were within 2 standard deviations of the mean measurement error. The mean measurement error was -0.28±0.15 mm for diameter measurements from shadow and UBM 35 images and -0.13±0.11 mm for those from shadow and UBM 50 images. These results indicate that diameter measurements from all three methods are the comparable. Measurements from UBM 50 images are closer to those from shadow-photogrammetric images than those from UBM 35 images.
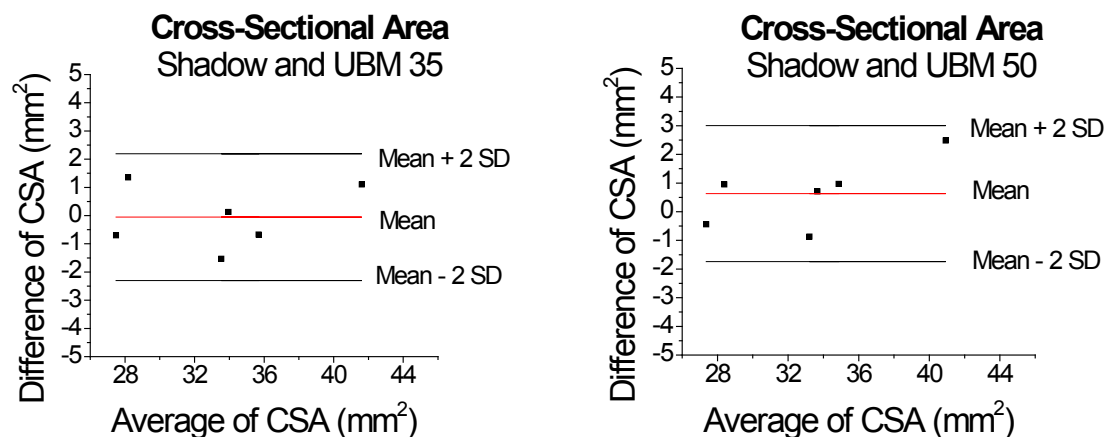
Figure 5.16: Bland-Altman plots for CSA of the lens comparing measurements from (left) shadow-photogrammetric images and UBM 35 images and (right) shadow-photogrammetric images and UBM 50 images of the lens. All measurements were within 2 standard deviations of the mean measurement error. The mean measurement error was -0.05 ± 1.15 mm^2 for measurements from shadow and UBM 35 images and 0.633 ± 1.18 mm^2 for those from shadow and UBM 50 images. These results indicate that CSA measurements from UBM 50 images are slightly lower than those from shadow images. CSA measurements from UBM 35 images are the same as those from shadow images.
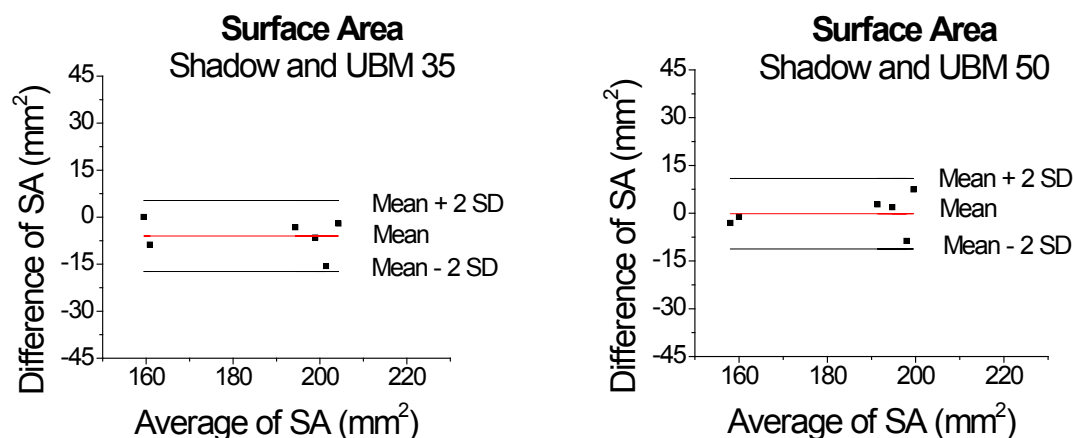
Figure 5.17: Bland-Altman plots for surface area of the lens comparing measurements from (left) shadow-photogrammetric images and UBM 35 images and (right) shadow-photogrammetric images and UBM 50 images of the lens. All measurements were within 2 standard deviations of the mean measurement error. The mean measurement error was -6.02 ± 5.66 mm^2 for measurements from shadow and UBM 35 images and -0.14 ± 5.53 mm^2 for those from shadow and UBM 50 images. These results indicate that SA measurements from UBM 35 images are slightly higher than those from shadow images. SA measurements from UBM 50 images are the same as those from shadow images.

Eye	Volume (mm^3)		
	Shadow images	**UBM 35 MHz**	**UBM 50 MHz**
H1 OD	152.8	162.8	157.6
H1 OS	163.1	157.2	159.1
H2 OD	256.3	251	233.3
H3 OD	214.9	215.4	207.8
H4 OD	209.4	226.7	218.8
H5 OD	222.2	231.5	215.6

Table 5.4: Volume of lenses measured from Shadow-photogrammetric images, and images from UBM 35 MHz and 50 MHz transducers.
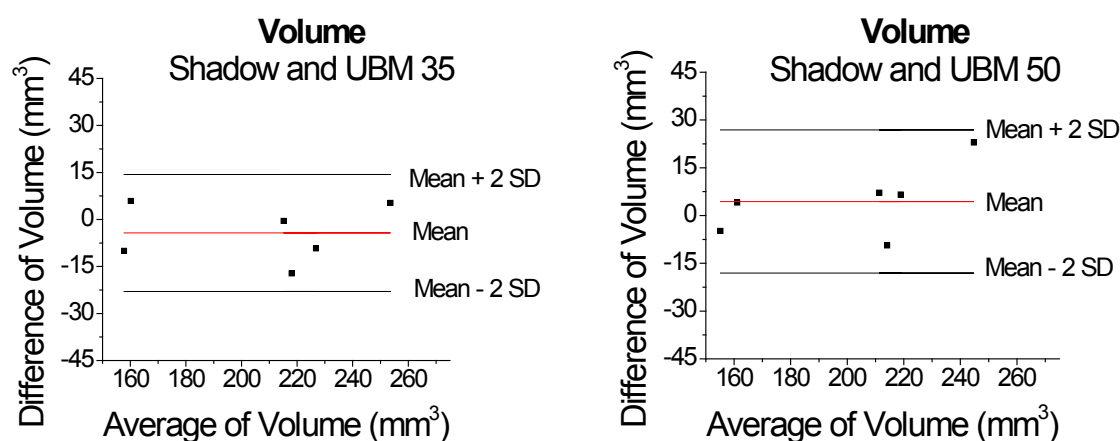
Figure 5.18: Bland-Altman plots for volume of the lens comparing measurements from (left) shadow-photogrammetric images and UBM 35 images and (right) shadow-photogrammetric images and UBM 50 images of the lens. All measurements were within 2 standard deviations of the mean measurement error. The mean measurement error was -4.3±9.33 mm^3 for the volume measurements from shadow and UBM 35 images and 4.4±11.25 mm^3 for those from shadow and UBM 50 images. These results indicate that volume measurements from UBM 35 images are slightly lower than those from shadow images whereas volume measurements from UBM 50 images are slightly higher than those from shadow images.

Eye	Anterior Radius of Curvature (mm)			Posterior Radius of Curvature (mm)		
	Shadow images	UBM 35 MHz	UBM 50 MHz	Shadow images	UBM 35 MHz	UBM 50 MHz
H1 OD	7.71	5.08	5.37	-4.53	-3.26	-3.18
H1 OS	8.03	6.76	6.36	-4.69	-3	-3.64
H2 OD	7.81	5.82	4.11	-4.84	1.14	-5.09
H3 OD	15	10.16	12.35	-6.06	-3.13	-3.55
H4 OD	13.22	11.33	10.55	-6.09	-3.79	-4.9
H5 OD	8.65	4.95	6.34	-6.17	-1.87	-1.97

Table 5.5: Anterior and Posterior Radius of Curvature of lenses measured from Shadow-photogrammetric images, and images from UBM 35 MHz and 50 MHz transducers
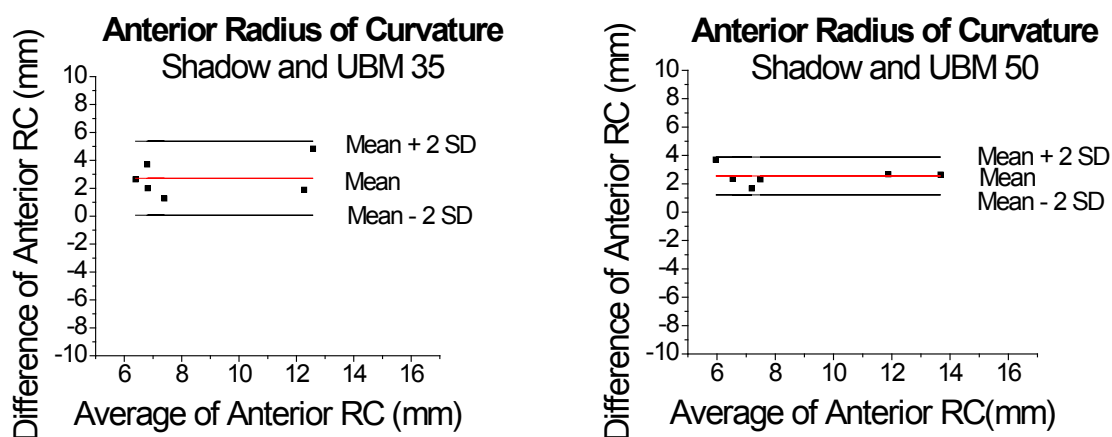
Figure 5.19: Bland-Altman plots for anterior radius of curvature of the lens comparing measurements from (left) shadow-photogrammetric images and UBM 35 images and (right) shadow-photogrammetric images and UBM 50 images of the lens. All measurements were within 2 standard deviations of the mean measurement error. The mean measurement error was 2.72±1.32 mm for the anterior radius of curvature measurements from shadow and UBM 35 images and 2.55±0.66 mm for those from shadow and UBM 50 images. These results indicate that anterior radius of curvature measurements from UBM 35 images and UBM 50 images are lower than those from shadow images.
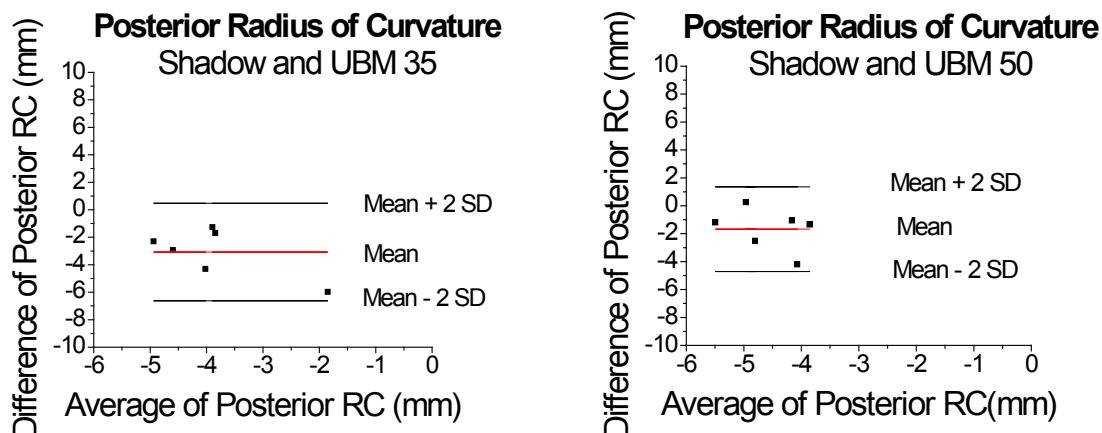
Figure 5.20: Bland-Altman plots for posterior radius of curvature of the lens comparing measurements from (left) shadow-photogrammetric images and UBM 35 images and (right) shadow-photogrammetric images and UBM 50 images of the lens. All measurements were within 2 standard deviations of the mean measurement error. The mean measurement error was -3.07±1.77 mm for the posterior radius of curvature measurements from shadow and UBM 35 images and -1.675±1.52 mm for those from shadow and UBM 50 images. These results indicate that posterior radius of curvature measurements from UBM 35 images and UBM 50 images are higher than those from shadow images.

5.6   Discussion and Conclusion

The goal of this study was to validate the lens shape obtained from UBM images. Towards this end, a shadow-photogrammetric system was developed to record un-distorted lens shape and a mathematical model using cosine functions was developed to quantify whole lens shape. The following parameters were measured using the cosine lens model: thickness, diameter, cross-sectional area, surface area and volume. Conic function fits were used to measure the central curvatures of the anterior and posterior surfaces of the lens.

Results indicate that UBM images of the lens can be used to obtain reliable dimensions, namely thickness, diameter, CSA, surface area and volume of the lens.

However, they cannot be used to measure radius of curvature. There is some degree of error in measuring anterior radius curvature due to refraction of sound waves at the posterior surface. There should be no error in measuring posterior radius of curvature. The poor correlation of the curvature data could be due two reasons: (a) Low resolution and poor contrast of UBM images introduce error in lens contour detection. (b) Adherent vitreous on the posterior surface of the lens compound this problem. The gradient speed of sound will also contribute to error in curvature measurement especially for the young lenses.

In conclusion, the UBM is a reliable tool to measure whole lens dimensions, but it cannot be used to measure radii of curvature. The UBM can be used in EVAS-II to image both the lens and the ciliary body together and to obtain quantitative information about the lens. In the next chapter, UBM images will be analyzed to obtain quantitative information about the ciliary body.

CHAPTER 6. EVALUATION OF CILIARY MUSCLE CONFIGURATIONAL CHANGES IN THE LENS STRETCHER

6.1 Overview

A three dimensional ultrasound linear scanning system will be developed to obtain sequential images of tissue in EVAS-II. 3D datasets of the accommodative apparatus of hamadryas baboons will be obtained during several stretched states. These data sets will be used to reconstruct images in meridional planes to obtain information about ciliary muscle configurational changes. These changes will be compared to in vivo published data to validate EVAS-II.

6.2 Design

A post and plate assembly was used to interface the UBM probe to EVAS-II (Figure 6.1). The probe was mounted on the same motion controlled translation stage that was described in section 4.4. The actuators (TRA25-CC) of the translation stage were controlled by a motion controller/driver (Newport ESP301-3N).
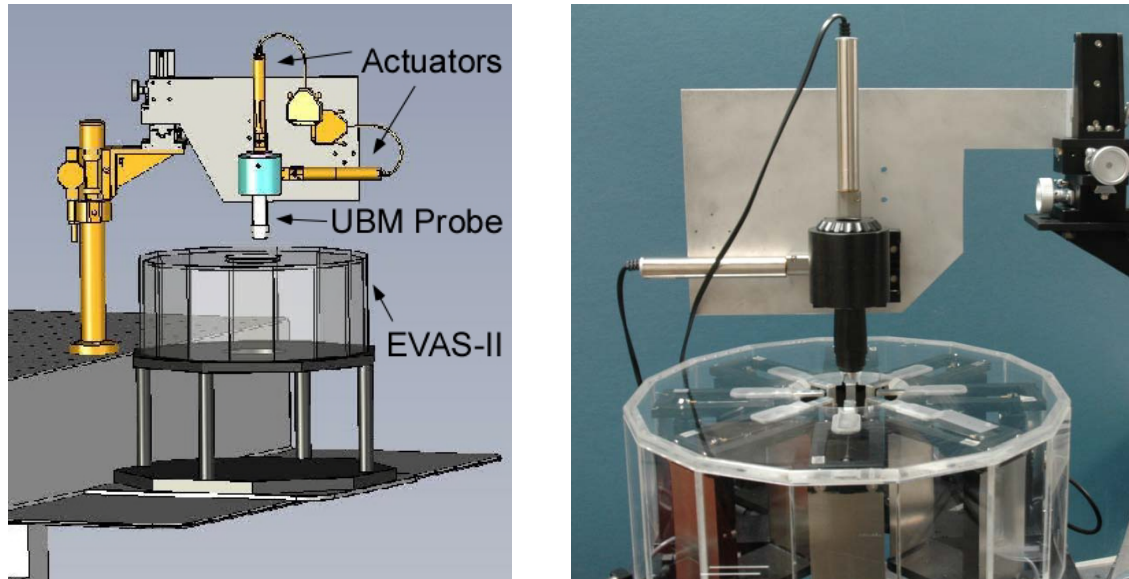
Figure 6.1: Schematics show the assembly used to interface the UBM probe to EVAS-II. The probe was mounted on a motion controlled translation stage and lowered into EVAS-II using a post and plate assembly.

6.3   Experiments

Experiments were performed on 5 hamadryas baboon eyes from 3 donors, with the 35 MHz transducer. Details of the eyes including, age, cause of death and postmortem time are provided in Table 6.1. The postmortem time ranged from 2 to 28 hours, and the age ranged from 6 to 8 years. All animals were healthy at time of euthanasia.

Tissue dissection was performed by an ophthalmic surgeon (Ehrmann, et al., 2008) and was similar to the procedure used during speed of sound measurement. The eight independent scleral shoes of EVAS-II were bonded with cyanoacrylate adhesive (Duro SuperGlue, Henkel Locktite Corp, Cleveland, OH) onto the anterior scleral surface (Figure 6.2 (a)). The posterior pole, the cornea and iris were then removed (Figure 6.2 (b)). Scleral incisions were made between adjacent shoes to produce 8 segments for

stretching (Figure 6.2 (c)). The dissected tissue was then transferred to the testing chamber, which was filled with the DMEM preservation medium (Figure 6.2 (d)).

In EVAS-II the tissue was mounted with the posterior surface of the lens facing upwards to enable UBM imaging of the ciliary body. The tissue was taken through a stretch cycle, stretching radially from 0 to 2.5 mm in intervals of 0.5 mm. At each interval UBM images of the tissue were recorded. The probe was translated in the direction perpendicular to the B-Scan motion of the transducer, at a rate of 0.5 m/s to obtain approximately 150 sequential images covering the entire accommodative apparatus at each stretch interval.

Eye	Age	PMT (Hours)
B1 OD	7 years, 10 months	2
B1 OS	7 years, 10 months	26
B2 OD	8 years, 4 months	2
B2 OS	8 years, 4 months	26
B3 OS	6 years, 11 months	28

Table 6.1: Summary of age and postmortem time of the hamadryas baboon eyes used in EVAS-II for the 3D study. All animals were healthy at time of euthanasia.

(a) (b)

(c) (d)
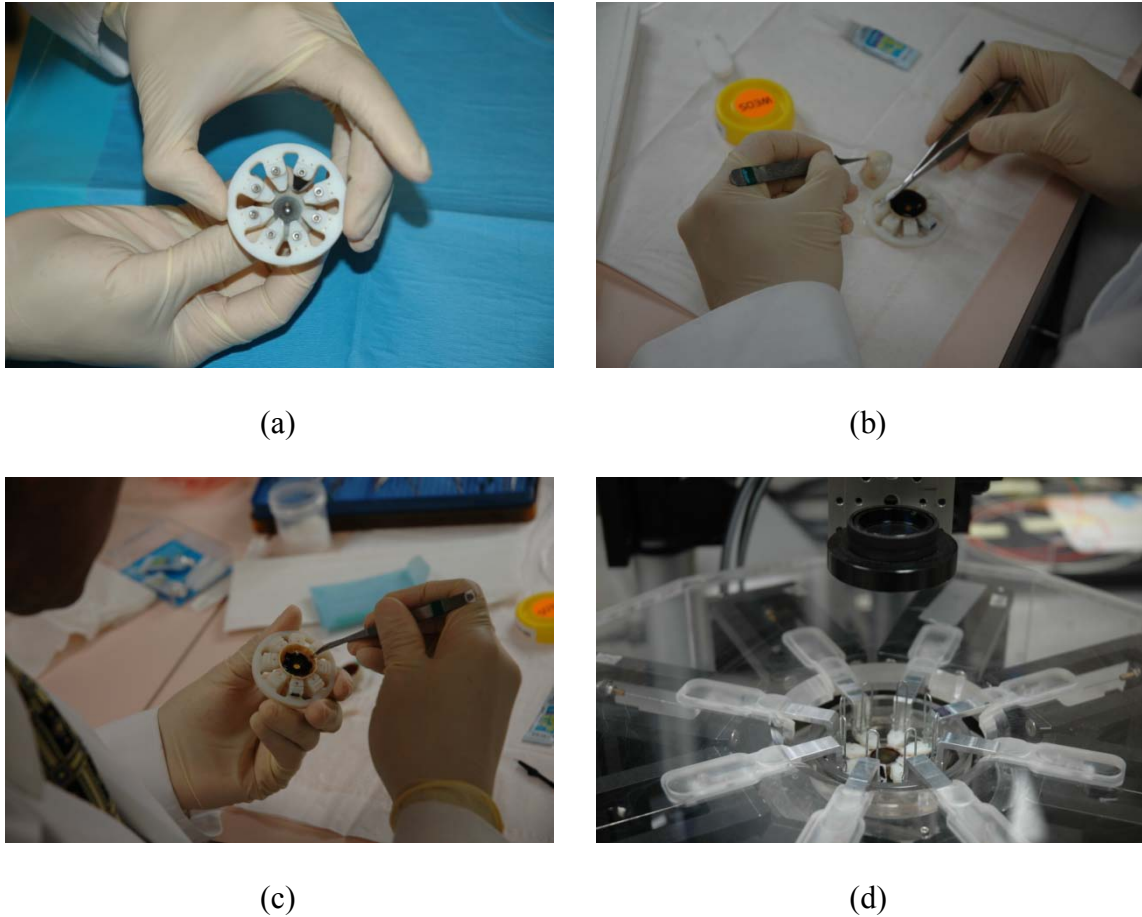
Figure 6.2: Tissue dissection procedure for EVAS-II. (a) The sclera is glued to the 8 independent shoes. (b) The posterior hemisphere, cornea and iris are removed. (c). Sclera is segmented between the 8 shoes. (d) Tissue is transferred to testing chamber in EVAS-II

6.4 Ultrasound Image Reconstruction in Meridional Planes

Raw data obtained from the 3-D scanner was converted into sequential jpeg images. Image construction was previously described in section 5.3.1. The images were then pre-processed to remove noise. Noise reduction was achieved by detecting the mode value of the image and setting all pixels whose values were less than the mode to that value.
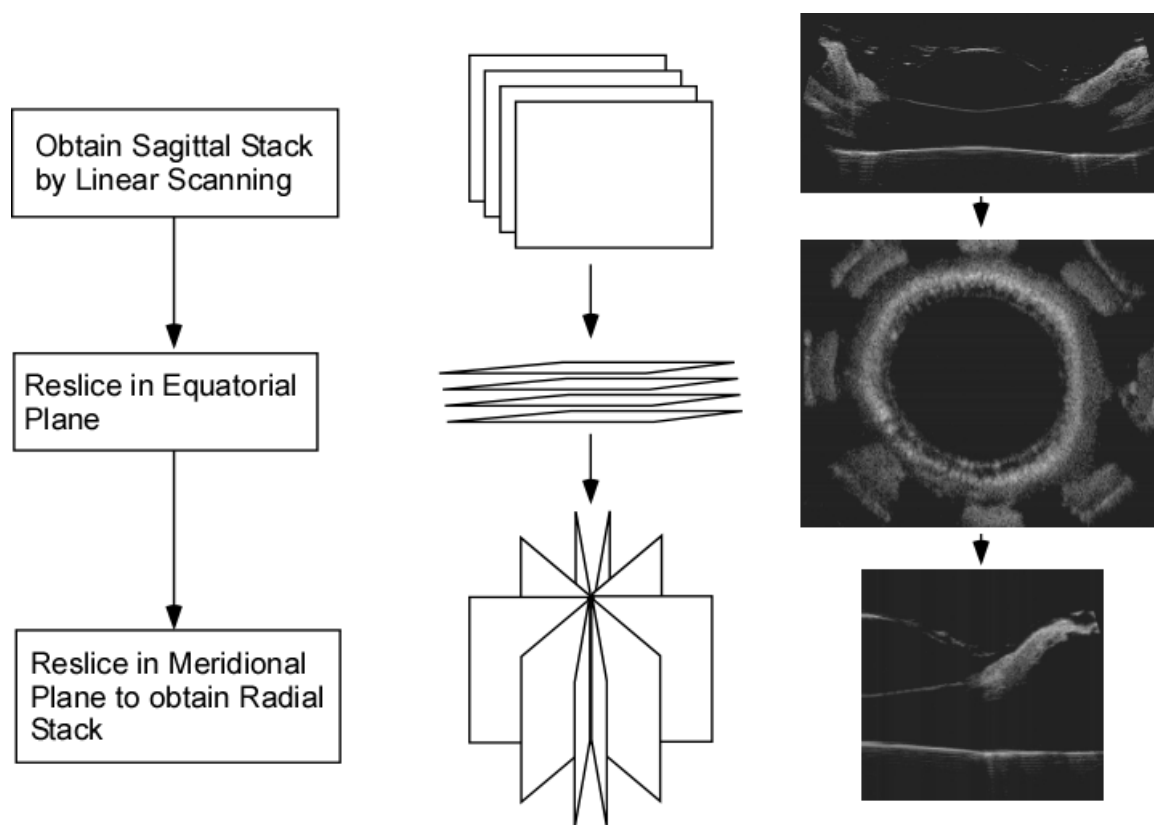
Figure 6.3: Flowchart describing ultrasound image reconstruction in meridional planes. The stack of cross-sectional images obtained from linear scanning in the sagittal plane is re-sliced in the equatorial plane to obtain cross-sectional images of the lens at various depths. The equatorial stack is then radially re-sliced to obtain radial cross-sectional images.

The image reconstruction process is illustrated in the flowchart in Figure 6.3. The sequential images obtained in the sagittal plane were loaded into the image processing software ImageJ, as a stack of images. The sagittal stack was then re-sliced in the equatorial plane using the 'Stack/Reslice' option, which reconstructs orthogonal slices through the image volume represented by the sagittal stack. The images were sliced at every 5 pixels.

In the equatorial plane a straight line was drawn through the center of the lens. The ImageJ plugin 'Radial Reslice' was used to re-slice the equatorial stack over 360 degrees at every 45 degrees. Re-slicing was performed by rotating the straight line drawn through the center of the lens. Eight images were produced over eight equally spaced hemi-meridional planes (Cut 0 to Cut 315).

Meridional images reconstructed in one hemi-meridional plane for each stretching interval are shown for baboon B1OD in Figure 6.4. Images clearly reveal the ciliary body and the lens.

(a) (b) (c)

(d) (e) (f)
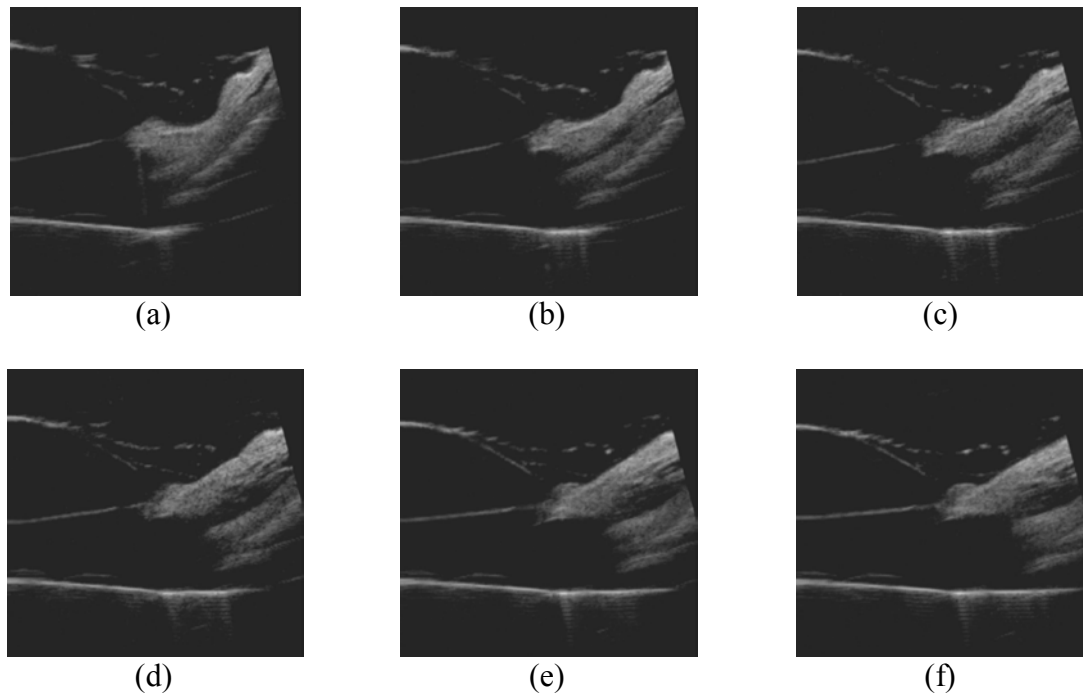
Figure 6.4: Radial reconstruction of tissue in EVAS-II for animal B1OD. Figures (a) through (f) represent tissue stretched from 0 to 2.5 mm, with 0.5 mm increments. The curved surface under the lens is a glass window in EVAS-II that appears curved in UBM images due to the difference in speed of sound in the lens and in DMEM.

6.5 Image Analysis

Reconstructed images are analyzed as follows to obtain a landmark on the ciliary body and to trace this landmark across stretching intervals. The original image (Figure 6.5 (a)) is used to create a mask (Figure 6.5 (b)) by user selection. The original image is then masked ((Figure 6.5 (c)) and converted to binary (Figure 6.5 (d)). The MATLAB function 'bwtraceboundary' is used to automatically trace the boundary of the ciliary body contour (Figure 6.5 (e)). The innermost point of this contour is detected (yellow point in (Figure 6.5 (f)) and the contour is restricted to 100 pixels (approximately 1 mm) from this point in both horizontal and vertical directions (blue contour in (Figure 6.5 (f)). The centroid of this new contour is detected (red point in (Figure 6.5 (f)) using the MATLAB function 'regionprops' which calculates the center of mass of the image delimited by the contour. The centroid is determined for every hemi-meridional plane per stretching interval. Figure 6.6 shows the centroid for every hemi-meridional plane at 1 mm of stretch for Baboon B1-OD. Figure 6.7 shows the centroid at every stretched state at one hemi-meridional plane for Baboon B1-OD. The coordinates of the centroid at each hemi-meridional plane is averaged to yield one point per each stretching interval.

Figure 6.8 (a) shows the coordinates of centroids of all images for Baboon B1 OD and the average points (dark blue) at each stretching interval . Step 0 was used as reference position and distances were measured from centroid positions at each stretch state to this position. Figure 6.8 (b) shows linear fits of centroid positions at each hemi-meridional plane for Baboon B1-OD. Linear fits were used to calculate total centroid displacement distances from step 0 to step 6 and the direction of displacement.

Centroid displacement distances from step 0 were examined in relation to load applied per stretching interval and to change in lens power, lens diameter and lens thickness. Lens thickness was measured from the UBM images, by examining the A-line at the center of the lens. Lens diameter, power and load were obtained from EVAS-II.

(a)   **(b)**   **(c)**

(d)   **(e)**   **(f)**
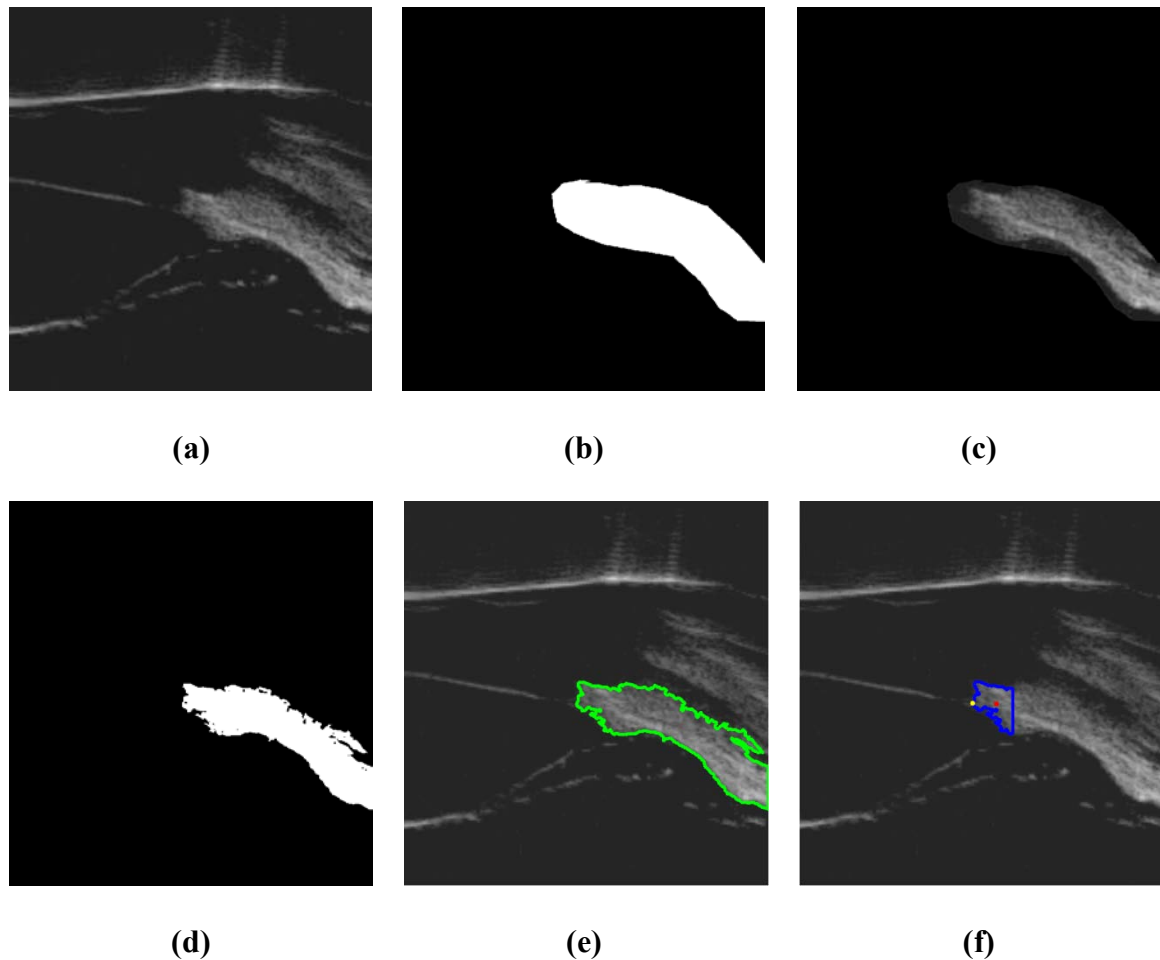
Figure 6.5: Figure illustrates ciliary body contour and centroid detection. The images obtained in EVAS-II were flipped to face the anterior surface of the lens upwards. (a) Original image. (b) A mask image is created by user selection. (c) Original image is masked. (d) Masked image is converted to binary (e) Ciliary body contour is detected (green). (f) The innermost point on the contour (yellow) is identified and the contour is limited to a distance of 100 pixels from the innermost point in both horizontal and vertical direction. The centroid (red) of the new contour (blue) is detected.

Step 2 – Cut 0　　　　**Step 2 – Cut 45**　　　　**Step 2 – Cut 90**

Step 2 – Cut 135　　　　**Step 2 – Cut 180**　　　　**Step 2 – Cut 225**

Step 2 – Cut 270　　　　**Step 2 – Cut 315**
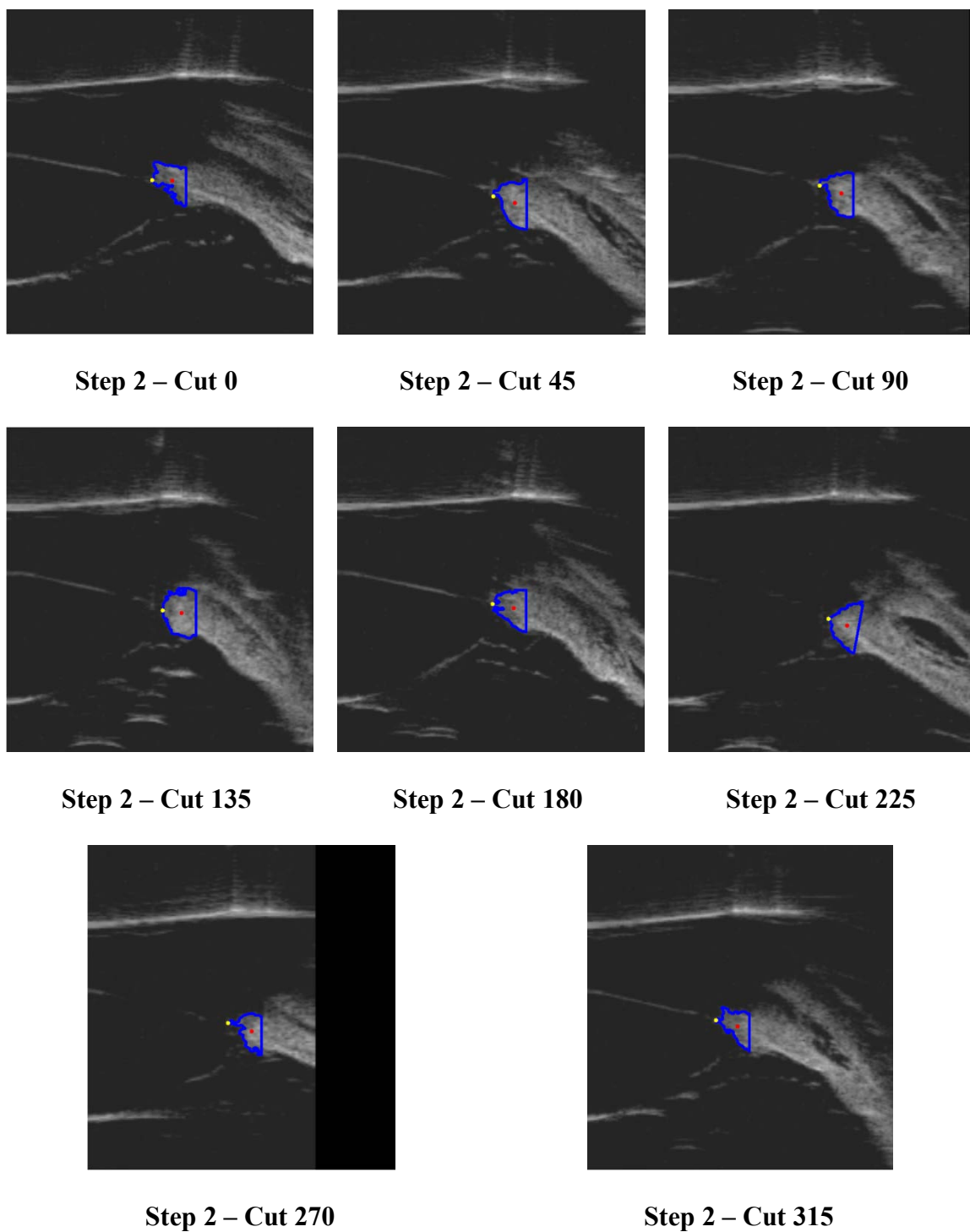
Figure 6.6: Ciliary body centroid (red) detection is performed on all eight hemi-meridional planes (Cut 0 to Cut 315) per stretching interval. Figure shows centroid for Baboon B1-OD at 1 mm of Stretch (Step 2).

| Step 0 - Cut 0 | Step 1 - Cut 0 | Step 2 – Cut 0 |
| Step 3 – Cut 0 | Step 4 – Cut 0 | Step 5 – Cut 0 |
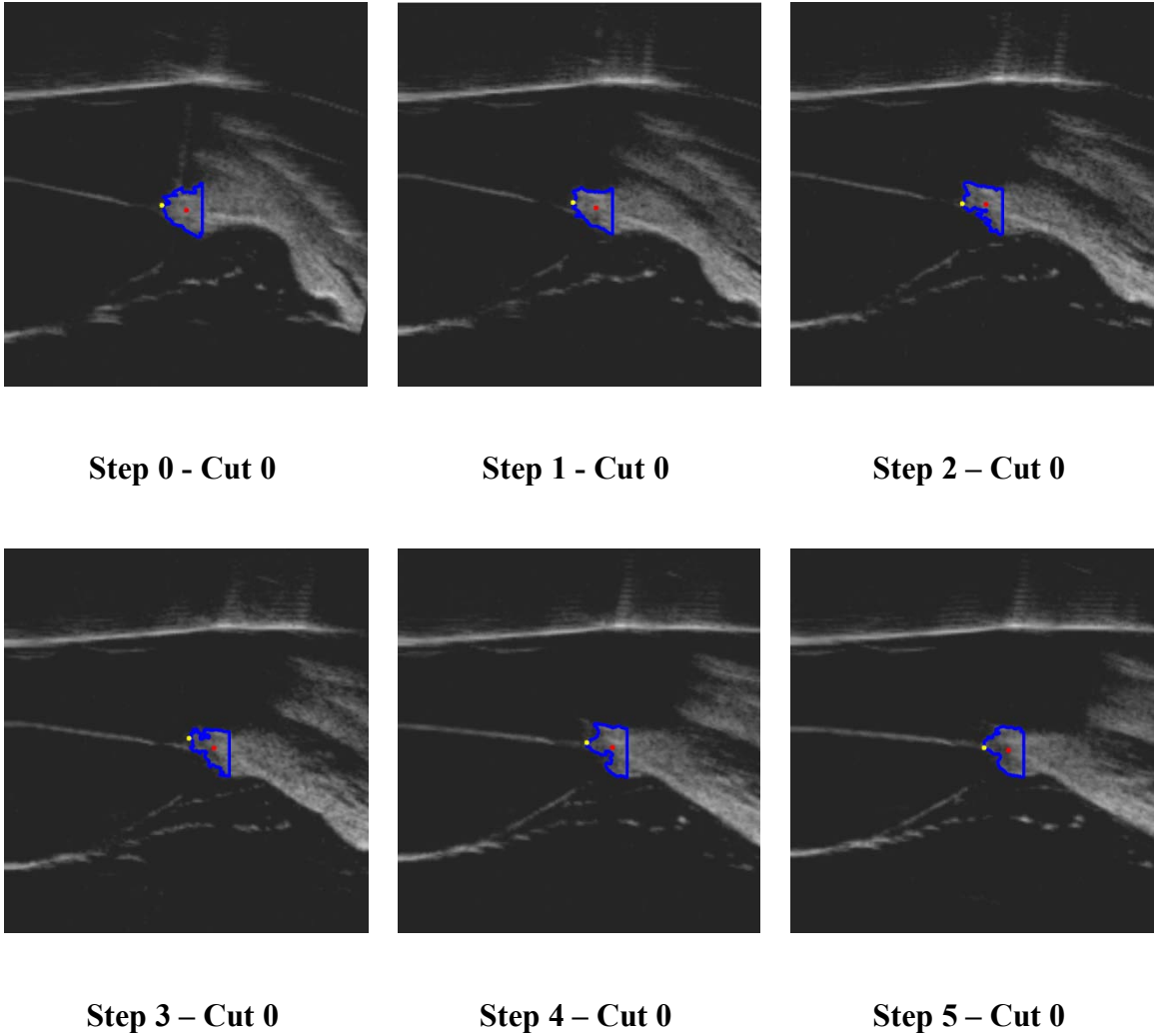
Figure 6.7: Ciliary body centroid (red) detection is performed at all stretching intervals (Step 0 to Step 5). Figure shows centroid for Baboon B1-OD at all stretching intervals in one hemi-meridional plane (Cut 0).

(a)

(b)
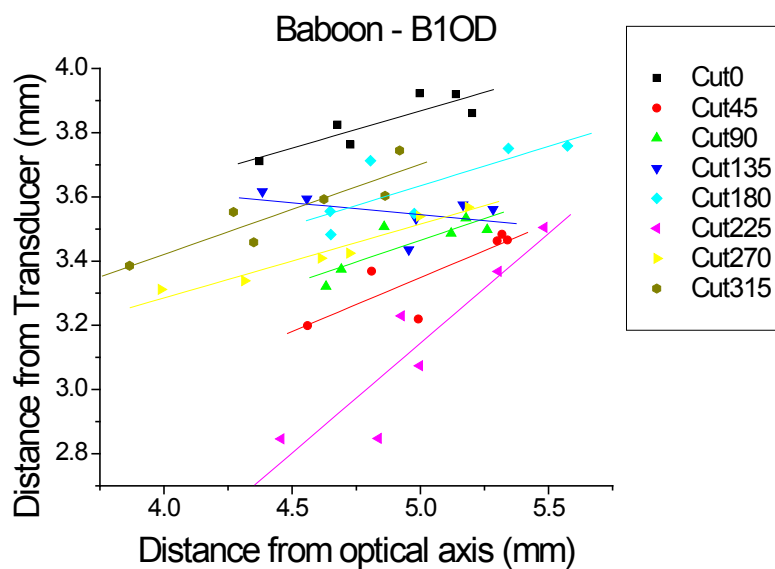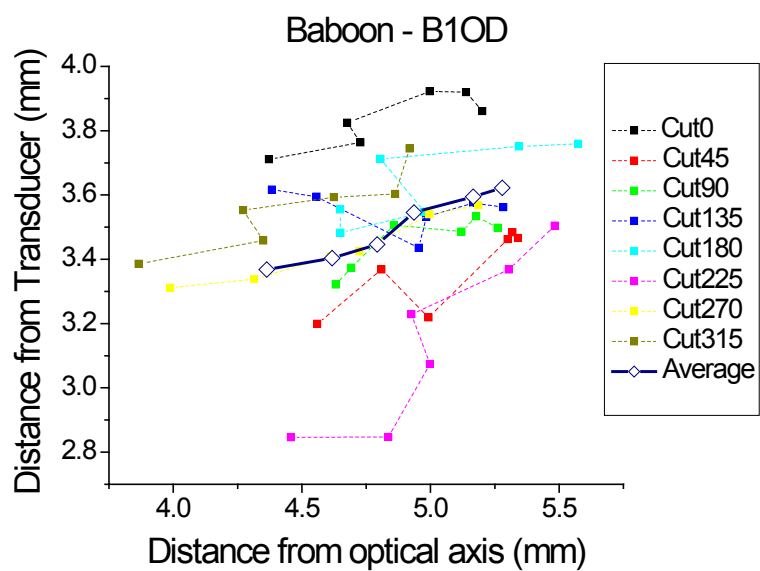
Figure 6.8: (a) The coordinates of the centroid at each hemi-meridional plane is averaged to yield one point per each stretching interval. Figure shows the average point in dark blue (◊) for Baboon B1-OD. (b) The linear fits of coordinates of the centroid at each hemi-meridional plane are assessed to calculate the average length of the line and the slope.

6.6 Results

6.6.1 CB Centroid Displacement

Figure 6.9 shows the average centroid positions (obtained from averaging positions per step at each hemi-meridional plane) for all five animals across all stretching intervals. CB centroid moved away from the optical axis and anteriorly during stretching. The absolute distances from step 0 to each stretch state were computed and tabulated in Table 6.2.

Linear fits of centroid positions at every hemi-meridional plane were used to calculate total displacement and direction of displacement. These values are tabulated in Table 6.3. Total centroid displacements varied from 0.93 to 1.09 mm at angles of 15.4 to 32°. Linear fits of average centroid positions yielded comparable values for total displacement (0.94 to 1.09 mm) and direction of displacement (16.8 to 32.1°).
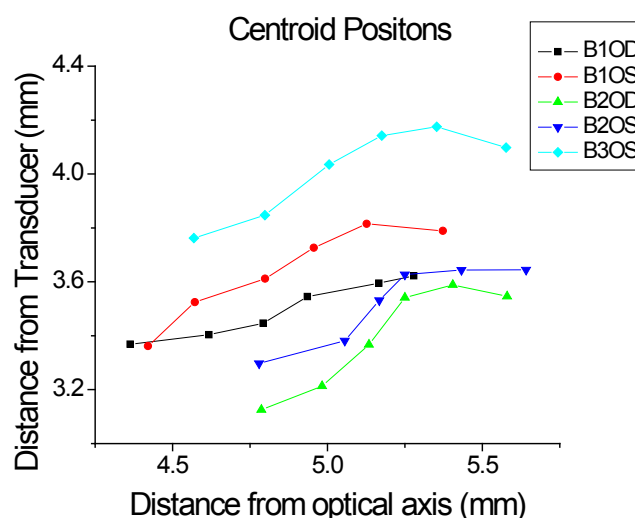
Figure 6.9: Figure shows the average centroid positions for the five animals across all stretching intervals.

	B1-OD (mm)	B1-OS (mm)	B2-OD (mm)	B2-OS (mm)	B3-OS (mm)	Average (mm)
Step 0	0	0	0	0	0	0
Step 1	0.26	0.22	0.21	0.29	0.24	0.25±0.03
Step 2	0.44	0.45	0.42	0.45	0.51	0.46±0.04
Step 3	0.6	0.65	0.62	0.57	0.72	0.63±0.05
Step 4	0.83	0.84	0.77	0.74	0.89	0.81±0.06
Step 5	0.95	1.04	0.9	0.93	1.06	0.98±0.07

Table 6.2: Displacement of CB centroid from Step 0 across all stretching intervals for the five animals used in this study and their average values.

	Average length of displacement (mm)	Average angle of displacement (°)
B1-OD	0.97 ± 0.21	15.4 ± 11.65
B1-OS	1.04 ± 0.17	22.8 ± 12.6
B2-OD	0.93 ± 0.32	32 ± 18.2
B2-OS	0.93 ± 0.43	22.6 ± 10.4
B3-OS	1.09 ± 0.3	20.9 ± 8.4

Table 6.3: Average length of displacement and direction of displacement were calculated from linear fits of centroid positions at each hemi-meridional plane.

6.6.2 CB Centroid Displacement Versus EVAS-II Stretch Distances

Figure 6.10 shows the CB centroid displacement as a function of stretch distance in EVAS-II. The average CB centroid displacement increased linearly with EVAS-II stretch distances at a rate of 0.41 ± 0.01 (p<0.0001).
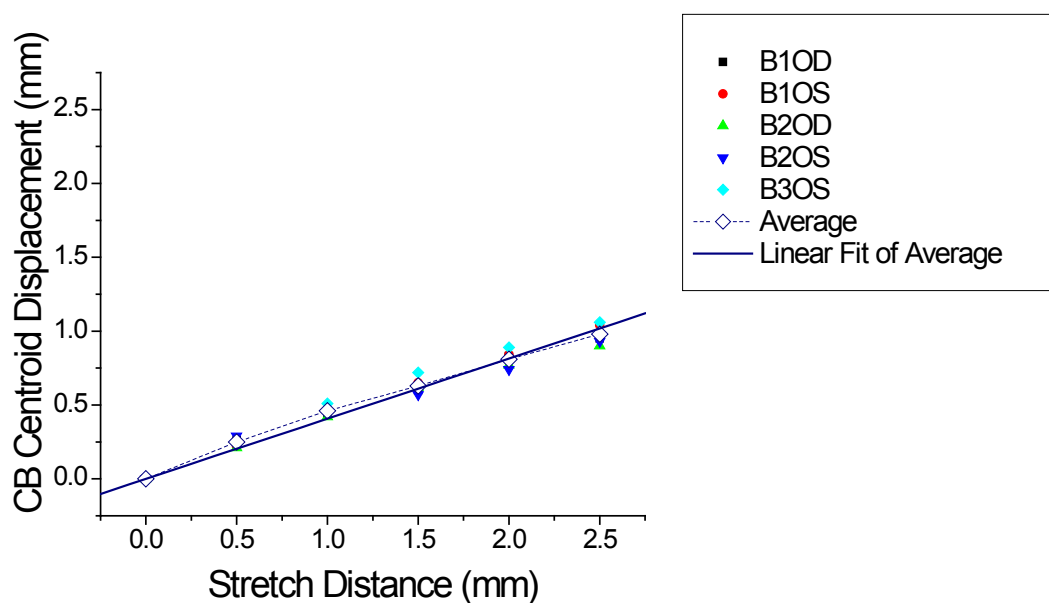
Figure 6.10: Graph shows CB centroid displacement from step 0 for each animal and the average values (◊) as a function of EVAS -II stretch distance. Linear fit of the average values yielded a slope of 0.41 ± 0.01 (p<0.0001), which indicates that for every mm of stretch the ciliary body centroid was displaced by 0.41mm.

6.6.3 EVAS-II Force Versus CB Centroid Displacement

Force applied in EVAS-II to stretch the ciliary body radially was examined as a function of change in displacement of CB centroid (Figure 6.11). An average value of 43.6 mN was required to move the centroid by 0.98 mm. After 1.5 mm of stretch (step 3) the force applied increased non-linearly when compared to ciliary body centroid displacement.
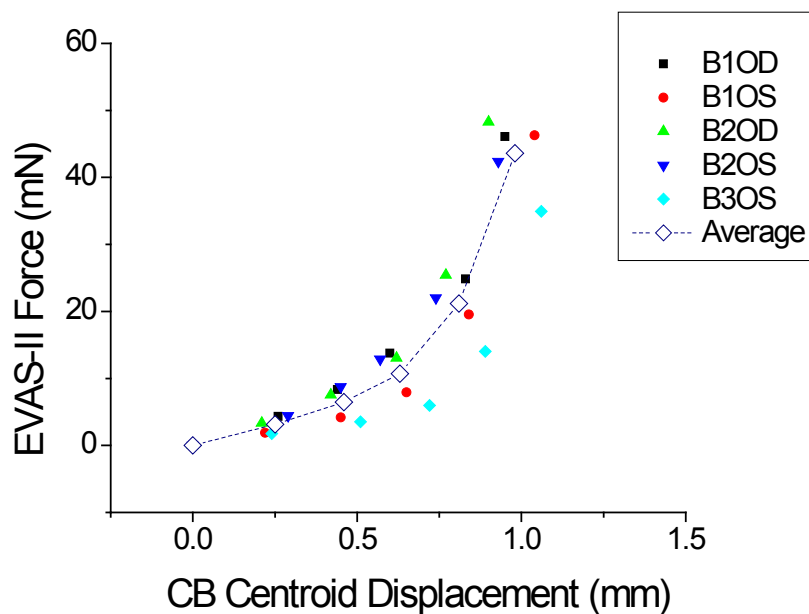
Figure 6.11: Graph shows force applied by EVAS-II to stretch tissue as a function of CB centroid displacement.

6.6.4 Lens Thickness Versus CB Centroid Displacement

Change in lens thickness was plotted as a function of change in CB centroid displacement. Average lens thickness remained relatively unchanged during the first two steps of stretching (1mm of stretch) and then decreased linearly at a rate of -0.63±0.07 (p=0.01) for the next 1.5mm of stretch.
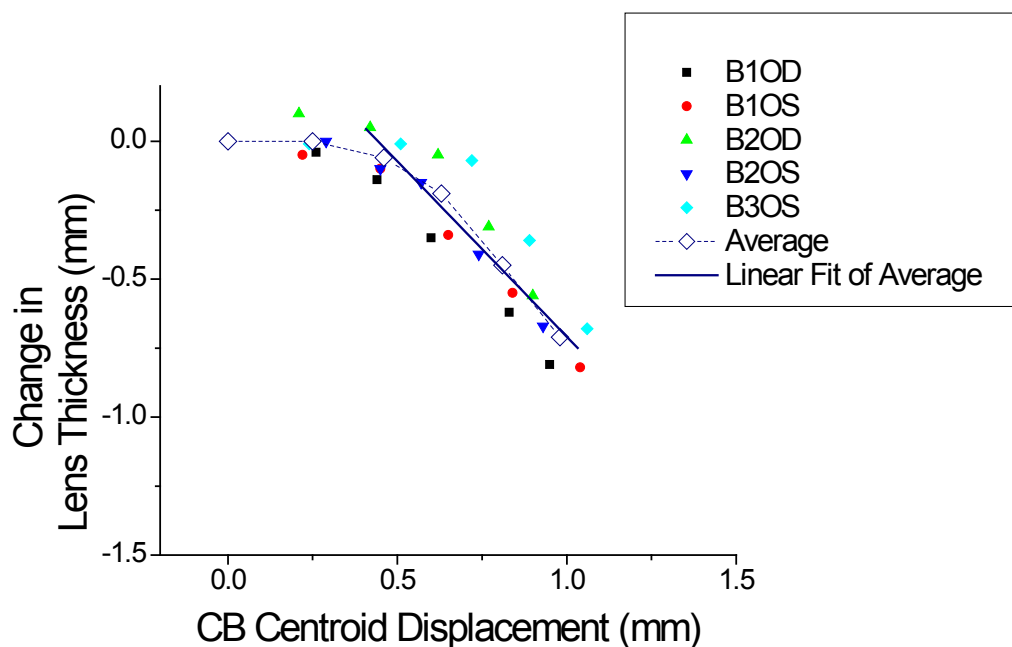
Figure 6.12: Change in lens thickness as a function of change in displacement of the CB centroid. Data shows that during the first mm of stretch the lens thickness remains relatively constant. Linear fit of average values (◊), excluding the first 2 stretch states, yields a slope of -0.63±0.07 (p=0.01) for the final 1.5mm stretch.

6.6.5 Lens Diameter Versus CB Centroid Displacement

Change in lens diameter was analyzed as a function of change in CB centroid displacement. Lens diameter could not always be measured at the zero stretch state because the ciliary body occluded the equator. Therefore, diameter at 0.5 mm of stretch was considered as the reference diameter. Lens diameter changed only after 1 mm of stretch. Linear fit of average lens diameter over the final 1.5mm of stretch yielded a slope of 1.1 ± 0.12 (p=0.01).
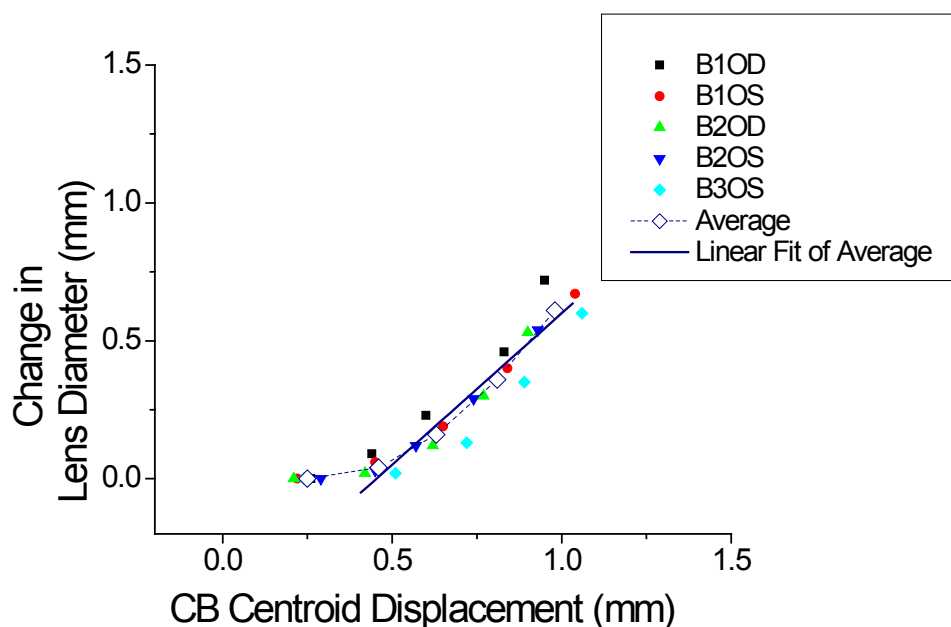
Figure 6.13: Change in lens diameter as a function of change in displacement of the CB centroid. Diameter at zero stretch could not always be measured and was therefore not included for data analysis. Linear fit of average values (◊), excluding the first 2 stretch states, yields a slope of 1.1 ± 0.12 (p=0.01) for the final 1.5mm stretch.

6.6.6 Accommodation Versus CB Centroid Displacement

Accommodative amplitude was plotted versus CB centroid displacement. The amount of accommodation per mm of CB centroid displacement was 36.8±2.5 D/mm (p=0.005) during the last 1.5mm of stretch
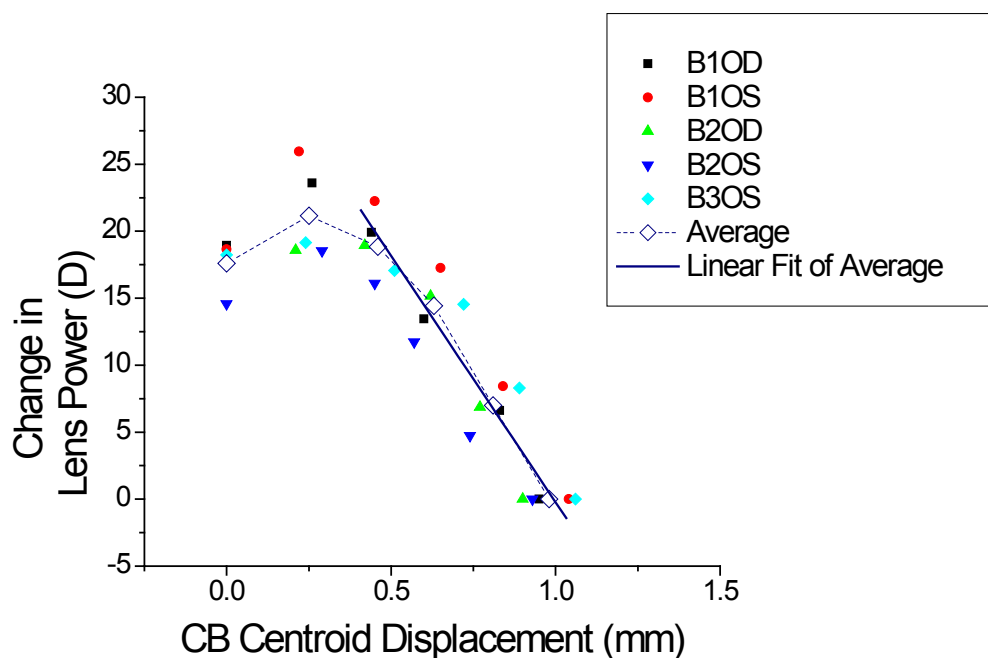
Figure 6.14: Change in lens power as a function of change in displacement of the CB centroid. Linear fit of average values (◊), excluding the first 2 stretch states, yields a slope of -36.8±2.5D/mm (p=0.005) for the final 1.5mm stretch.

6.7 Discussion and Conclusion

A three dimensional ultrasound imaging system was developed to obtain images of tissue in EVAS-II. Sequential images of the entire accommodative apparatus were recorded during several stretched steps and data obtained was used to reconstruct images in eight equally spaced hemi-meridional planes. The reconstructed images were processed to obtain information about ciliary body displacement during stretching of the tissue in EVAS-II.

Local CB centroid was displaced outward and anterior during stretching as the shoes were radially stretched. This would correspond to inward and posterior movement during accommodation. CB centroid was displaced consistently (0.93 to 1.09 mm) in the same direction (between 16 and 32°) for the total 2.5 mm of stretch. Absolute distances between CB centroid positions varied linearly as a function of stretch distances.

In EVAS-II, forward or anterior motion of CB centroid during stretching (dis-accommodation) refers to movement towards anterior chamber of the eye. In literature the CB is described as moving inward and forward during accommodation (Rohen, 1979; Croft, et al., 2006, 2009). However, a point of reference is not provided for the movement. A schematic from Rohen (1979) shows the eye oriented such that the posterior zonular fibers (PPZ) are horizontal (Figure 6.15). UBM images used by Croft, et al., (2006, 2009) were presented with the same orientation. In EVAS-II ocular tissue is oriented such that the lens equator is horizontal. The posterior zonular fibers (PPZ) are not visible in UBM images in EVAS-II and therefore, the same reference geometry could not be used for comparison.
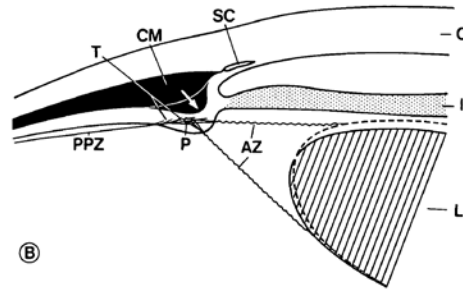
Figure 6.15: Schematic of the accommodating eye from Rohen (1979). The posterior zonules fibres (PPZ) are horizontal. In EVAS-II the lens equator is horizontal.

Forward movement has only been quantified by Croft, et al., (2006, 2009). They described forward movement as a decrease in angle between the anterior aspect of the CB and the inner aspect of the cornea (Figure 6.16 (a)). The inner aspect of the cornea is not always available in EVAS-II, but similar measurements can be made in a few images. Figure 6.16 (b) shows that the angle increased after stretching, similar to Croft et al.,'s (2006, 2009) in vivo observations, demonstrating 'forward' movement of the CB during simulated accommodation in EVAS-II.

Although ciliary body in EVAS-II moves outward and posterior during accommodation, it should be noted that these measurements were made when the shoes in EVAS-II were mounted upside down, with the anterior surface of the lens facing down. This orientation of the shoes, enabled imaging of the entire ring of ciliary muscle. If the shoes are mounted in the original orientation, with the anterior surface of the lens facing upwards, and forces are applied in the same direction, the movement would be outward and anterior during accommodation, which would be similar to the in vivo behavior. These results have to be verified either by recording images of this orientation in cross-sections between the shoes or by imaging the ciliary body from below.
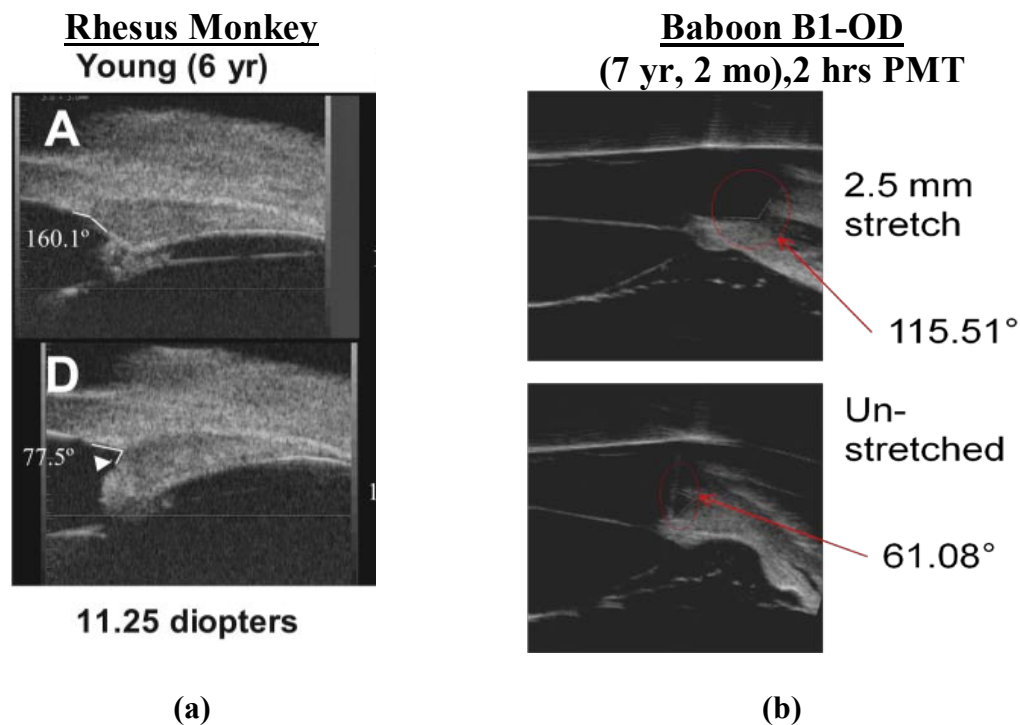
Figure 6.16: (a) UBM images of temporal quadrants in the rhesus monkey eye (Croft, et al., 2006). The anterior aspect of the CB moves past the sclera spur and the angle between the inner aspect of the cornea and the anterior aspect of the CB decreases during accommodation. (b) UBM images of Baboon tissue in EVAS-II, showing similar movement.

Lens thickness was relatively unchanged during the first two stretching intervals, indicating an anatomical difference between the accommodative structures in the maximally accommodated in vivo eye and tissue in EVAS-II. Examination of UBM, OCT and coronal digital images of tissue in EVAS-II at Step 0 showed ciliary body partially covering the lens equator. This condition is most likely caused due to slack in the ciliary body in post mortem lenses. This issue can be resolved by a 'pre-stretch' of the tissue until the CB is no longer occluding the lens equator. For data analysis in this project the first two stretch states were not included. Lens thickness decreased linearly with CB centroid displacement during the final 1.5mm stretch.

Lens diameter increased linearly with CB centroid displacement at the rate of 1.1 (ratio of change in lens diameter and change in CB centroid displacement). Croft, et al (2009) measured lens equator and ciliary process (CP) distances to a fixed landmark placed at the corneoscleral limbus in live rhesus monkeys, using goniovideography (Figure 6.17). They reported a slightly lower value of 0.86 for the relationship between lens movement and CP movement for the young lens (6-10 years).

Accommodation in EVAS-II in the young baboon lens was 36.8 D/mm of CB centroid movement. Croft, et al., (2006) reported a value of 0.015 mm/D for nasal muscle and 0.011 mm/D for the temporal muscle of the live rhesus monkey in the age range of (5.8-26 years). The inverse of the EVAS-II slope yields 0.027 mm/D, indicating that in the young baboon eye in EVAS-II CB has to move twice the distance in the live rhesus monkey eye, to produce the same amount of accommodation. The difference could mainly be due to the process of accommodation. In vivo, the process involves muscle contraction and relaxation, whereas in EVAS-II it is produced by passive stretch of the muscle. The difference could also be in part due to the use of goniovideographic images to obtain ciliary process displacement distances (Figure 6.17). Goniovideographic images are en-face images and do not provide depth information and therefore only allow measurement of centripetal movement only. UBM images allow quantification of centripetal and anterior movement, accounting for larger displacement rate for accommodation in EVAS-II. Also, Croft, et al., (2006) included a large age range of rhesus monkeys (5.8 – 26 years) whereas for this study only young lenses were available (6 – 8 years). Differences in nasal and temporal muscle movement were not considered in this study as CB centroid displacement distances were averaged over 8 hemi-meridional

planes. The difference could also be species related. Taking into account these differences in measurement techniques, the EVAS-II findings are in relative good agreement with in vivo measurements.
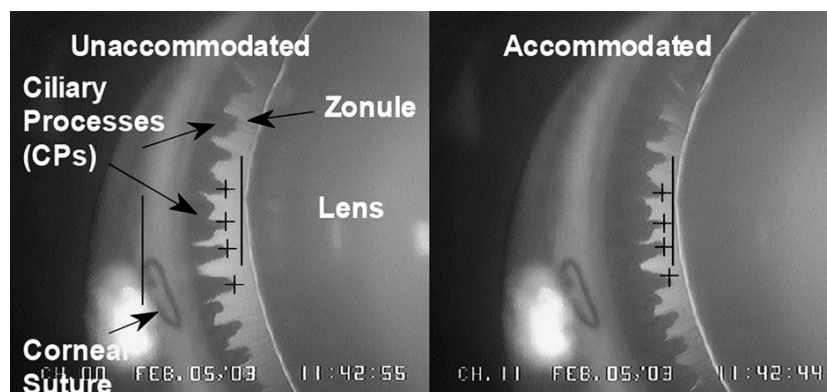
Figure 6.17: Goniovideography images of normal lens and ciliary process (CP) configuration in the accommodated and unaccommodated states (Croft et al., 2006). A 9-0 nylon suture placed at the corneoscleral limbus served as a reference point (left solid vertical line) from which to measure distances to the lens equator (right solid vertical line) and the CPs (cross-hairs). Only centripetal movement can be measured from these images. UBM images allow measurement of centripetal and anterior movement.
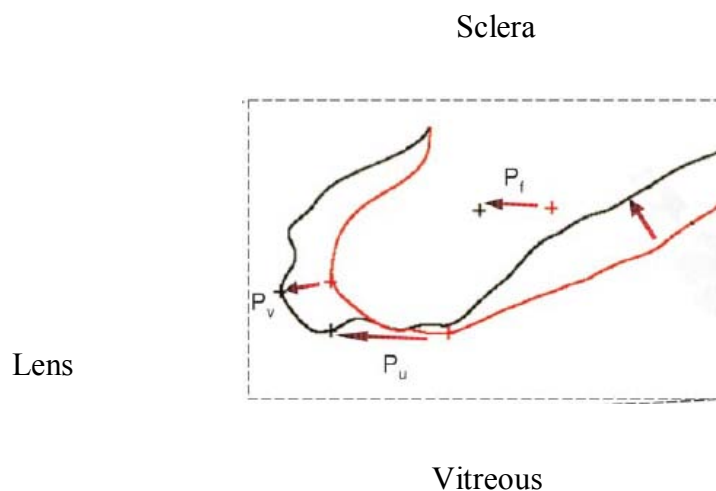
Figure 6.18: Quantification of the contour changes of the ciliary muscle during accommodation in the human eye (Stachs et al., 2002). The outer contours in accommodation (black) and dis-accommodation (red) are shown, as is the shift of defined characteristic contour points (center of gravity Pf, anterior contour point Pv and lower contour point Pu).

Ciliary muscle center of gravity displacement in the young human eye was measured by Stachs, et al., in 2002 (Figure 6.18). They reported a value of 0.17 mm of movement for accommodation in a 34 year old human. The displacement value is about 5 times lower than measured values of local CB centroid displacement in EVAS-II for the young baboon eye. However, when the first 2 steps of stretching, where there is no change in lens thickness, diameter and power, are not considered, the local CB centroid displacement reduces to 0.52 mm which is 3 times the reported value in the young human eye. The difference in displacement values could be species related. They could also be because Stachs, et al., (2002) measured center of gravity of the whole muscle, whereas in this study local CB centroid displacement was measured. For the same human eye, other landmarks on the ciliary body (Figure 6.18) such as the anterior contour point (Pv) and the lower contour point (Pu) moved 0.36 and 0.56 mm respectively. Similar landmarks could not be identified in images from EVAS-II, most likely due to tissue preparation.

In summary data presented here shows that the UBM provides informative data about the ciliary body to validate EVAS-II. However, results cannot be compared directly with published in vivo data. A methodology has to be developed to make similar measurement in vivo for comparison with EVAS-II. Also, similar analysis has to be performed in older baboon eyes to assess age related configurational changes of the ciliary body in response to stretching forces in EVAS-II. Similar experiments should be performed on human eyes to determine interspecies variations.

In conclusion ciliary body in EVAS-II moves outward and posterior during accommodation. Local ciliary body centroid displacement values in the young baboon eye are comparable to in vivo displacement values in the rhesus monkey. The work

described in this chapter demonstrates that UBM can provide useful data to quantify ciliary body changes. More data, both in vivo and in EVAS-II is required to validate age dependent changes.

CHAPTER 7. **SUMMARY AND CONCLUSIONS**

The goal of this project is to obtain quantitative images of the lens and the ciliary body to validate EVAS-II. To accomplish this goal it was necessary to develop methods, instrumentation and image processing techniques to acquire 3D images in EVAS-II, using UBM, and to apply these techniques to non-human primate eyes.

Knowledge of the shape of the lens and the position and orientation of the ciliary muscle during accommodation is important to better understand accommodation and presbyopia and to develop new treatments for presbyopia. Previous measurements of lens shape in EVAS-II were made with optical imaging techniques. The position and orientation of the ciliary muscle were not recorded in EVAS-II because the ciliary muscle cannot be imaged using optical imaging techniques. Therefore, the UBM was chosen to image both the lens and the ciliary muscle in the stretcher. The UBM is fast and enables acquisition of multiple images for 3-D reconstruction in a short period of time.

The speed of sound in the lens was first measured, to obtain accurate biometric information about the lens. The average speed measured by the 35 and 50 MHz transducers at the center of the un-stretched lens was 1685 m/s and 1687 m/s respectively for lenses that were not swollen. These values are 45-47 m/s (<3%) larger than reported values. These higher values could be due to better hydration control of the lens by using DMEM as immersion medium and not water or saline solution which swells tissue and changes the lens shape. Speed of sound measured across the equatorial profile showed variations similar to refractive index gradients obtained from MRI measurements. The

younger lens showed greater variation of speed of sound across the equatorial profile than the older lenses. As both speed of sound and refractive index are dependent on protein concentration, the speed measurements validate MRI measurements of the refractive index. Results from speed measurements are consistent with lens compaction and with the formation of a protein nuclear plateau.

To validate the lens shape obtained from UBM images, a shadow-photogrammetric system was developed to record un-distorted lens shape. A mathematical model using cosine functions was developed to describe and quantify the shape of the whole lens. Thickness, diameter, cross-sectional area, surface area and volume were measured using the cosine lens model. Conic function fits were used to measure the central curvatures of the anterior and posterior surfaces of the lens. Comparison of data from UBM and shadow-photogrammetric images indicate that UBM images of the lens can be used to obtain reliable measurements of thickness, diameter, CSA, surface area and volume of the lens. However, they cannot be used to measure radius of curvature. The poor correlation of the curvature data is be due to the low resolution and poor contrast of UBM images and adherent vitreous on the posterior surface of the lens which cause error in lens contour detection. The gradient speed of sound in the lens also contributes to error in curvature measurement especially for the young lenses. The UBM is a reliable tool to measure whole lens dimensions, but it cannot be used to measure radii of curvature.

A three dimensional ultrasound imaging system was developed to obtain images of tissue in EVAS-II. Sequential images of the entire accommodative apparatus were recorded during several stretched steps and data obtained was used to reconstruct images

in eight equally spaced hemi-meridional planes. The reconstructed images were processed to obtain information about ciliary body displacement during stretching of the tissue in EVAS-II. Accommodation in EVAS-II is comparable to the in vivo process.

The main findings and contributions of this project are:

- The speed of sound exhibits a gradient profile across the equator similar to the refractive index gradient obtained from MRI measurements. This profile is consistent with lens compaction and with the formation of a protein nuclear plateau. These first measurements of the speed of sound profile on intact lenses, opens new avenues of research in determining the relationship between mechanical and optical properties of the crystalline lens.

- Cosine functions can be used to describe and quantify the whole lens shape. This mathematical model was used to develop an age dependent lens shape model (Urs et al., submitted to Vision Research, VR-09-429, acknowledged on 11/10/2009) that can be used in studies employing numerical modeling of accommodation.

- UBM can be used to image and quantify the lens and the ciliary body in EVAS-II. These UBM images provide valuable information about the geometry of the lens in relationship with the geometry, orientation and position of the ciliary body at different stretched states. This information can be used in computational studies of accommodation and presbyopia.

- Accommodation process in the non-human primate lens in EVAS-II is comparable to the in vivo mechanism.

Additional experiments can be designed to assess age dependence of speed of sound gradient in the lens. Speed of sound can also be measured in lens protein solutions to determine the accurate constant value for the lens in Goss et al.,'s (1980) general empirical model to build a new model to predict speed of sound in the crystalline lens. Additional experiments can also be performed in EVAS-II to evaluate ciliary body movement in older lenses to assess age related changes in EVAS-II. Instrumentation and experimental protocols have to be developed to make similar measurements in vivo.

In conclusion UBM can be used to obtain reliable quantitative information about the lens and the ciliary body. 3-D UBM enables monitoring of ciliary body motion of the entire accommodative apparatus.

REFERENCES

Abramoff, M. D., Magelhaes, P. J., & Ram, S. J. (2004). Image processing with ImageJ. *Biophotonics International*, *11*, pp. 26-42.

Atchison, D. A. (1995). Accommodation and presbyopia. *Ophthalmic and Physiological Optics* , *15*, 255-272.

Augusteyn, R. C., Rosen, A. M., Borja, D., Ziebarth, N. M., & Parel, J.-M. (2006). Biometry of primate lenses during immersion in preservation media. *Molecular Vision* , *12*, 740-747.

Augusteyn, R. C. (2008). Growth of the lens: in vitro observations. *Clinical and Experimental Optometry* , *91*, 226-239.

Barer, K., & Joseph, S. (1954). Refractometry of living cells. *Quarterly Journal Microscopy in Science* , *95*, 399-423.

Beers, A. P., & van der Heijde, G. L. (1994). Presbyopia and velocity of sound in the lens. *Optometry and Vision Science* , *71*, 250-253.

Begui, Z. E. (1954). Acoustic properties of the refractive media of the eye. *The Journal of the Acoustical Society of America* , *26*, 365-368.

Bernal, A., Parel, J.-M., & Manns, F. (2006). Evidence for posterior zonular fiber attachment on the anterior hyaloid membrane. *Investigative Ophthalmology and Visual Science* , *47*, 4708-4713.

Borja, D., Manns, F., Ho, A., Ziebarth, N. M., Rosen, A. M., Jain, R., et al. (2008). Optical power of the isolated human crystalline lens. *Investigative Ophthalmology & Visual Science* , *49*, 2541-2548.

Borja, D., Uhlhorn, S. R., Ziebarth, N. M., Nankivil, D., Arrieta-Quintero, E., Ehrmann, K., et al. (2009a). Scheimpflug camera system for cross-sectional imaging of the ex vivo crystalline lens during simulated accommodation. *SPIE, Poster # 7163-65*.

Borja, D., Manns, F., Uhlhorn, S., Ho, A., & Parel, J.-M. (2009b). Age-dependent optical model of the isolated human crystalline lens. *Investigative Ophthalmology and Visual Science* , *50*, ARVO E-Abstract 6125.

Burd, H. J., Judge, S. J., & Cross, J. A. (2002). Numerical modelling of the accommodating lens. *Vision Research* , *42*, 2235-2251.

Bushberg, J. T., Seibert, J. A., Leidholdt Jr., E. M., & Boone, J. M. (2001). *The Essential Physics of Medical Imaging* (2nd Edition ed.). Lippincott Williams & Wilkins.

Byrne, S. F., & Green, R. L. (2002). *Ultrasound of the Eye and Orbit* (2nd Edition ed.). St. Louis, Missouri: Mosby Inc.

Carstensen, E. L., Li, K., & Schwan, H. P. (1953). Determination of the acoustic properties of blood and its components. *The Journal of Acoustical Society of America , 25*, 286-89.

Carstensen, E. L., & Schwan, H. P. (1959). Acoustic properties of hemoglobin solutions. *Journal of the Acoustical Society of America , 31*, 305-311.

Chivers, R. C., Round, W. H., & Zieniuk, J. K. (1984). Investigation of ultrasound axially traversing the human eye. *Ultrasound in Medicine and Biology , 10*, 173-188.

Cobbold, R. (2007). *Foundations of Biomedical Ultrasound.* New York: Oxford University Press, Inc.

Coleman, D. J. (1970). Unified model for accommodative mechanism. *American Journal of Ophthalmology , 69*, 1063-1079.

Coleman, D. J., Lizzi, F. L., Franzen, L. A., & Abramson, D. H. (1975). A determination of the velocity of ultrasound in cataractous lenses. In *Ultrasonography in Ophthalmology* (pp. 246-251). Basel: Karger.

Coleman, D. J. (1986). On the hydraulic suspension theory of accommodation. *Transactions of the American Ophthalmological Society , 84*, 846-848.

Coleman, D. J., Silverman, R. H., Rondeau, M. J., & Lizzi, F. L. (1992). New perspectives: 3-D volume rendering of ocular tumors. *Acta Ophthalmologica Supplement , 204*, 22.

Coleman, D. J., & Fish, S. K. (2001). Presbyopia, accommodation, and the mature catenary. *Ophthalmology , 108*, 1544-1551.

Coleman, D. J., Reinstein, D. Z., Silverman, R. H., & Lizzi, F. L. (2005). Ultrasound maps the eye. Looking inside the eye with corneal maps and 3-D data. *RT-Image , 18*, 3.

Coleman, D. J., Silverman, R. H., Lizzi, F. L., & Rondeau, M. J. (2006). *Ultrasonography of the Eye and Orbit* (2nd Edition ed.). Lippincott Williams & Wilkins.

Croft, M. A., Glasser, A., Heatley, G., McDonald, J., Ebbert, T., Dhal, D. B., et al. (2006). Accommodative ciliary body and lens function in rhesus monkeys, I: Normal lens, zonule and ciliary process configuration in the iridectomized eye. *Investigative Ophthalmology & Visual Science , 47*, 1076-1086.

Croft, M. A., McDonald, J. P., Nadkarni, N. V., Lin, T. L., & Kaufman, P. L. (2009). Age-related changes in centripetal ciliary body movement relative to centripetal lens movement in monkeys. *Experimental Eye Research , 89*, 824-832.

De Korte, C. L., van der Steen, A. F., & Thijssen, J. M. (1994a). Acoustic velocity and attenuation of eye tissues at 20 MHz. *Ultrasound in medicine & biology , 20*, 471-480.

De Korte, C. L., Van Der Steen, A. F., Thijssen, J. M., Duindam, J. J., Otto, C., & Puppels, G. J. (1994b). Relation between local acoustic parameters and protein distribution in human and porcine eye lenses. *Experimental Eye Research , 59*, 617-627.

Delides, C. G., & King, T. A. (1979). High frequency ultrasonic studies of poly (dimethylsiloxane) networks. *Journal of the Chemical Society, Faraday Transactions 2: Molecular and Chemical Physics , 75*, 359 - 368.

Dendy, P. P., & Heaton, B. (1999). *Physics for Diagnostic Radiology.* Taylor & Francis.

Denham, D. B., Holland, S., Mandelbaum, S., Pflugfelder, S. C., & Parel, J. M. (1989). Shadow photogrammetric apparatus for the quantitative evaluation of corneal buttons. *Ophthalmic Surgery , 20*, 794-9.

Dubbelman, M., & Van der Heijde, G. L. (2001). The shape of the aging human lens: Curvature, equivalent refractive index and the lens paradox. *Vision Research , 41*, 1867-1877.

Dussik, K. T. (1942). Über die Möglichkeit, hochfrequente mechanische Schwingungen als diagnostisches Hilfsmittel zu verwerten. *Zeitschrift für die gesamte Neurologie und Psychiatrie , 174*, 153-168.

Dussik, K. T. (1952). Weitere Ergebnisse der Ultraschalluntersuchung bei Gehirnerkrankungen. *Acta Neurochirurgica , 2*, 379-401.

Ehrmann, K., Ho, A., & Parel, J.-M. (2008). Biomechanical analysis of the accommodative apparatus in primates. *Clinical and Experimental Optometry , 91*, 302-312.

Fisher, R. F. (1971). The elastic constants of the human lens. *The Journal of Physiology , 212*, 147-180.

Fisher, R. F. (1977). The force of contraction of the human ciliary muscle during accommodation. *The Journal of Physiology , 270*, 51-74.

Foster, F. S., Pavlin, C. J., Harasiewicz, K. A., Christopher, D. A., & Turnbull, D. H. (2000). Advances in ultrasound biomicroscopy. *Ultrasound in Medicine & Biology , 26*, 1-27.

Fukasaku, H., & Marron, J. A. (2001). Anterior ciliary sclerotomy with silicone expansion plug implantation: Effect on presbyopia and intraocular pressure. *International Ophthalmology Clinics , 41*, 133-141.

Galton, F. (1883). *Inquiries into Human Faculty and its Development.* Macmillan.

Gavish, B., Gratton, E., & Hardy, C. J. (1983). Adiabatic compressibility of globular proteins. *Proceedings of the National Academy of Sciences , 80*, 750-754.

Glasser, A., & Campbell, M. C. (1998). Presbyopia and the optical changes in the human crystalline lens with age. *Vision Research , 38*, 209-229.

Glasser, A., & Kaufman, P. L. (1999). The mechanism of accommodation in primates. *Ophthalmology(Rochester, MN) , 106*, 863-872.

Glasser, A., & Kaufman, P. L. (2003). Accommodation and presbyopia. In P. L. Kaufman, & A. Alm, *Adler's Physiology of the Eye: Clinical Application* (2nd Edition ed., pp. 197-233). St Louis, MO: Mosby.

Goss, S. A., Johnston, R. L., & Dunn, F. (1978). Comprehensive compilation of empirical ultrasonic properties of mammalian tissues. *The Journal of the Acoustical Society of America , 64*, 423-457.

Goss, S. A., Frizzell, L. A., & Dunn, F. (1980). Dependence of the ultrasonic properties of biological tissue on constituent proteins. *Journal of the Acoustical Society of America , 67*, 1041-1044.

Griffin, D. R. (1958). *Listening in the Dark.* Yale University Press New Haven.

Haefliger, E., & Parel, J. M. (1994). Accommodation of an endocapsular silicone lens (Phaco-Ersatz) in the aging rhesus monkey. *Journal of Refractive and Corneal Surgery , 10*, 550-555.

Helmholtz, H. (1855). *Ueber die Accommodation des Auges.* Archiv fur Ophthalmolgie.

Hill, C. R., Bamber, J. C., & Ter Haar, G. R. (2002). *Physical Principles of Medical Ultrasoincs.* Wiley.

Howcroft, M. J., & Parker, J. A. (1977). Aspheric curvatures for the human lens. *Vision Research , 17*, 1217-1223.

Huang, C. C., Ameri, H., DeBoer, C., Rowley, A. P., Xu, X., Sun, L., et al. (2007). Evaluation of lens hardness in cataract surgery using high-frequency ultrasonic parameters in vitro. *Ultrasound in Medicine & Biology , 33*, 1609-1616.

Ishikawa, T. (1962). Fine structure of the human ciliary muscle. *Investigative Ophthalmology , 1*, 587-608.

Jansson, F., & Sundmark, E. (1961). Determination of the velocity of ultrasound in ocular tissues at different temperatures. *Acta Ophthalmol (Copenh) , 39*, 899-910.

Jansson, F., & Kock, E. (1962). Determination of the velocity of ultrasound in the human lens and vitreous. *Acta Ophthalmologica , 40*, 420-433.

Jones, C. E., Atchison, D. A., Meder, R., & Pope, J. M. (2005). Refractive index distribution and optical properties of the isolated human lens measured using magnetic resonance imaging (MRI). *Vision Research , 45*, 2352-2366.

Kasprzak, H. T. (2000). New approximation for the whole profile of the human crystalline lens. *Ophthalmic and Physiological Optics , 20*, 31-43.

Katzir, S. (2003). The discovery of the piezoelectric effect. *Archive for History of Exact Sciences , 57*, 61-91.

Koopmans, S. A., Terwee, T., Glasser, A., Wendt, M., Vilipuru, A. S., van Kooten, T. G., et al. (2006). Accommodative lens refilling in rhesus monkeys. *Investigative Ophthalmology & Visual Science , 47*, 2976-2984.

Koretz, J. F., Handelman, G. H., & Brown, N. P. (1984). Analysis of human crystalline lens curvature as a function of accommodative state and age. *Vision Research , 24*, 1141-1151.

Krag, S., Andreassen, T. T., & Olsen, T. (1996). Elastic properties of the lens capsule in relation to accommodation and presbyopia. *Investigative Ophthalmmology and Visual Science , 37*, Abstract no. 774.

Lafon, C., Khokhlova, V. A., Kaczkowski, P. J., Bailey, M. R., Sapozhnikov, O. A., & Crum, L. A. (2006). Use of a bovine eye lens for observation of HIFU-induced lesions in real-time. *Ultrasound in medicine & biology , 32*, 1731-1741.

Lippmann, G. (1881). Principe de la conservation de l'électricité. *Annales de chimie et de physique , 24*, 145-178.

Lodish, H., Berk, A., Kaiser, C. A., Krieger, M., Scott, M. P., Bretscher, A., et al. (2007). *Molecular Cell Biology* (6th Edition ed.). New York: W. H. Freeman.

Manns, F., Ho, A., & Kruger, R. R. (2004a). Customized visual correction of presbyopia. In *Wavefront Customized Visual Corrections: the Quest for Super Vision II* (2nd Edition ed., pp. 353–360). Thorofare NJ: Slack Inc.

Manns, F., Fernandez, V., Zipper, S., Sandadi, S., Hamaoui, M., Ho, A., et al. (2004b). Radius of curvature and asphericity of the anterior and posterior surface of human cadaver crystalline lenses. *Experimental Eye Research , 78*, 39-51.

Manns, F., Parel, J.-M., Denham, D., Billotte, C., Ziebarth, N. M., Borja, D., et al. (2007). Optomechanical response of human and monkey lenses in a lens stretcher. *Investigative Ophthalmology & Visual Science , 48*, 3260-3268.

Marmer, R. H. (2001). The surgical reversal of presbyopia: A new procedure to restore accommodation. *International Ophthalmology Clinics , 41*, 123-132.

Mastropasqua, L., Toto, L., Nubile, M., Falconio, G., & Ballone, E. (2003). Clinical study of the 1CU accommodating intraocular lens. *Journal of Cataract & Refractive Surgery , 29*, 1307-1312.

Myers, R. I., & Krueger, R. R. (1998). Novel approaches to correction of presbyopia with laser modification of the crystalline lens. *Journal of refractive surgery , 14*, 136-139.

Neuweiler, G. (2000). *The Biology of Bats.* Oxford University Press, USA.

Nishi, O., & Nishi, K. (1998). Accommodation amplitude after lens refilling with injectable silicone by sealing the capsule with a plug in primates. *Archives of Ophthalmology , 116*, 1358-1361.

Oksala, A., & Lentinen, A. (1958). Measurement of the velocity of sound in some parts of the eye. *Acta Ophthalmologica , 36*, 633-639.

Parel, J.-M., Gelender, H., Trefers, W. F., & Norton, E. W. (1986). Phaco-Ersatz: Cataract surgery designed to preserve accommodation. *Graefe's Archive for Clinical and Experimental Ophthalmology , 224*, 165-173.

Parel, J.-M., Fernandez, V., Billotte, C., Denham, D. B., Lamar, P. D., Rosen, A., et al. (2002). Accommodation stress-strain relation in human and non-human primate eyes ex-vivo. *Investigative Ophthalmology and Visual Science , 43*, E-Abstract 406.

Parel, J.-M., Lee, W., Lamar, P., Acosta, A. C., Abri, A., Nose, I., et al. (2004). Manual Lens Stretching Apparatus (MLSA) for rapid analysis of the optical properties of the natrual lens, accommodating IOL and refilled lens capsule (Phaco-Ersatz). *Investigative Ophthalmology and Visual Science , 45*, ARVO E-Abstract 1724.

Pau, H. (1951). Dependence of the shape of the lens on physical factors. *Ophthalmologica , 122*, 308-314.

Pauly, H., & Schwan, H. P. (1971). Mechanism of absorption of ultrasound in liver tissue. *The Journal of the Acoustical Society of America , 50*, 692-699.

Pavlin, C. J., & Foster, F. S. (1995). *Ultrasound Biomicroscopy of the Eye.* New York, Berlin, Heidelberg: Springer.

Pfeiffer, H., Heremans, K., & Wevers, M. (2008). The influence of correlated protein-water volume fluctuations on the apparent compressibility of proteins determined by ultrasonic velocimetry. *Biochimica et Biophysica Acta , 1784*, 1546-1551.

Pflugfelder, S. C., Roussel, T. J., Denham, D. B., Feuer, W., Mandelbaum, S., & Parel, J. M. (1992). Photogrammetric analysis of corneal trephination. *Archives of Ophthalmology , 110*, 1160-1166.

Pierscionek, B., Smith, G., & Augusteyn, R. C. (1987). The refractive increments of alpha, beta and gamma crystallins. *Vision Research , 27*, 1539-1541.

Pierscionek, B. K. (1995). Age-related response of human lenses to stretching forces. *Experimental Eye Research , 60*, 325-332.

Poyer, J. F., Kaufman, P. L., & Flugel, C. (1993). Age does not affect contractile responses of the isolated rhesus monkey ciliary muscle to muscarinic agonists. *Current eye research , 12*, 413-422.

Poynting, J. H., & Thomson, J. J. (1920). *A Textbook of Physics: Sound* (7th Edition ed.). London: C. Griffin.

Rasband, W. S. (1997-2008). *ImageJ*. (U. S. National Institutes of Health, Bethesda, Maryland, USA.) Retrieved from http://rsb.info.nih.gov/ij/

Ripken, T., Oberheide, U., Fromm, M., Schumacher, S., Gerten, G., & Lubatschowski, H. (2008). fs-Laser induced elasticity changes to improve presbyopic lens accommodation. *Graefe's archive for clinical and experimental ophthalmology , 246*, 897-906.

Rivara, A., & Sanna, G. (1962). Determinazione della velocità degli ultrasoni nei tessuti oculari di uomo e di maiale. *Ann. Ottal , 88*, 675-682.

Rohen, J. W. (1979). Scanning electron microscopic studies of the zonular apparatus in human and monkey eyes. *Invest Ophthalmol Vis Sci , 18*, 133-144.

Rosen, A. M., Denham, D. B., Fernandez, V., Borja, D., Ho, A., Manns, F., et al. (2006). In vitro dimensions and curvatures of human lenses. *Vision Research , 46*, 1002-1009.

Schachar, R. A., Huang, T., & Huang, X. (1993a). Mathematical proof of Schachar's model of accommodation. *Annals of Ophthalmology , 25*, 5-9.

Schachar, R. A., Cudmore, D. P., & Black, T. D. (1993b). Experimental support for Schachar's Hypothesis on accommodation. *Annals of Ophthalmology , 25*, 404-409.

Schachar, R. A., & Bax, A. J. (2001a). Mechanism of human accommodation as analyzed by nonlinear finite element analysis. *Comprehensive Therapy , 27*, 122-132.

Schachar, R. A., & Bax, A. J. (2001b). Mechanism of accommodation. *International Ophthalmology Clinics , 41*, 17-32.

Schachar, R. A. (2002). Presbyopic surgery. *International Ophthalmology Clinics , 42*, 107-118.

Siebinga, I., Vrensen, G. F., De Mul, F. M., & Greve, J. (1991). Age-related changes in local water and protein content of human eye lenses measured by Raman microspectroscopy. *Experimental Eye Research , 53*, 233-239.

Silverman, R. H., Lizzi, F. L., Ursea, B., Rondeau, M. J., Eldeen, N. B., Kaliscz, A., et al. (2001). High-resolution ultrasonic imaging and characterization of the ciliary body. *Investigative Ophthalmology & Visual Science , 42*, 885-894.

Stachs, O., Martin, H., Kirchhoff, A., Stave, J., Terwee, T., & Guthoff, R. (2002). Monitoring accommodative ciliary muscle function using three-dimensional ultrasound. *Graefe's Archive for Clinical and Experimental Ophthalmology , 204*, 906-912.

Stachs, O., Schneider, H., Stave, J., & Guthoff, R. (2005). Potentially accommodating intraocular lenses--an in vitro and in vivo study using three-dimensional high-frequency ultrasound. *ournal of Refractive Surgery , 21*, 37-45.

Stachs, O., Martin, H., Behrend, D., Schmitz, K. P., & Guthoff, R. (2006). Three-dimensional ultrasound biomicroscopy, environmental and conventional scanning electron microscopy investigations of the human zonula ciliaris for numerical modelling of accommodation. *Graefe's Archive Clinical and Experimental Ophthalmology , 244*, 836-844.

Stephens, R. (1972). Piezoelecticity and the growth of ultrasonics. *Journal de Physique , 33*, C64-C69.

Strenk, S. A., Strenk, L. M., Semmlow, J. L., & DeMarco, J. K. (2004). Magnetic resonance imaging study of the effects of age and accommodation on the human lens cross-sectional area. *Investigative Ophthalmology & Visual Science , 45*, 539-545.

Strenk, S. A., Strenk, L. M., & Koretz, J. F. (2005). The mechanism of presbyopia. *Progress in Retinal and Eye Research , 24*, 379-393.

Strenk, S. A., Strenk, L. M., & Guo, S. (2006). Magnetic resonance imaging of aging, accommodating, phakic, and pseudophakic ciliary muscle diameters. *Journal of Cataract & Refractive Surgery , 32*, 1792-1798.

Subbaram, M. V., Gump, J. C., Bullimore, M. A., & Sooryakumar, R. (2002). The elasticity of the human lens. *Investigative Ophthalmology and Visual Science , 43*, E-Abstract 468.

Suetens, P. (2002). *Fundamentals of Medical Imaging.* Cambridge University Press.

Sunderland, H. R., & O'Neill, W. D. (1976). Functional dependence of optical parameters on circumferential forces in the cat lens. *Vision Research , 16*, 1151-1158.

Tabandeh, H., Wilkins, M., Thompson, G., Nassiri, D., & Karim, A. (2000). Hardness and ultrasonic characteristics of the human crystalline lens. *Journal of Cataract & Refractive Surgery , 26*, 838-841.

Tahi, H., Fantes, F., Hamaoui, M., & Parel, J. M. (1999). Small peripheral anterior continuous curvilinear capsulohexis. *Journal of Cataract & Refractive Surgery , 25*, 744-747.

Thijssen, J. M., Mol, M. J., & Timer, M. R. (1985). Acoustic parameters of ocular tissues. *Ultrasound in Medicine and Biology , 11*, 157-161.

Uhlhorn, S. R., Borja, D., Manns, F., & Parel, J.-M. (2008). Refractive index measurement of the isolated crystalline lens using optical coherence tomography. *Vision Research , 48*, 2732-2738.

Urs, R., Manns, F., Ho, A., Borja, D., Amelinckx, A., Smith, J., et al. (2009). Shape of the isolated ex-vivo human crystalline lens. *Vision Research , 49*, 74-83.

Urs, R., Ho, A., Manns, F., Parel, J.-M. (2009). Age-dependent Fourier model of the shape of isolated ex vivo human crystalline lens. (Submitted to *Vision Research, VR-09-429* acknowledged on 11/10/2009).

van Alphen, G. W., & Graebel, W. P. (1991). Elasticity of tissues involved in accommodation. *Vision Research , 31*, 1417-1438.

Willard, G. W. (1947). Temperature coefficient of ultrasonic velocity in solutions. *The Journal of the Acoustical Society of America , 19*, 235-241.